

# COUPLED WAVE PROPAGATION IN A ROD WITH A DYNAMIC ABSORBER LAYER

by

Jiulong Meng

BSEE, University of Science and Technology of China, 1988

SUBMITTED TO THE DEPARTMENT OF OCEAN  
ENGINEERING IN PARTIAL FULFILLMENT OF THE  
REQUIREMENTS FOR THE DEGREE OF

MASTER OF SCIENCE

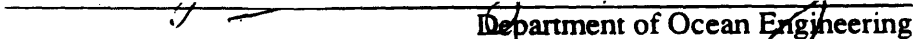
at the

MASSACHUSETTS INSTITUTE OF TECHNOLOGY

February 1991

Copyright © Massachusetts Institute of Technology, 1991. All rights reserved.

Signature of Author

  
Department of Ocean Engineering  
February, 1991

Certified by

  
Professor Ira Dyer  
Thesis Supervisor

Accepted by

  
Professor A. Douglas Carmichael  
Chairman, Department Committee

# **COUPLED WAVE PROPAGATION IN A ROD WITH A DYNAMIC ABSORBER LAYER**

by

Jiulong Meng

Submitted to the Department of Ocean Engineering on February , 1991 in partial fulfillment of the requirements for the degree of Master of Science.

## **Abstract**

This thesis experimentally tests the effect of a continuous longitudinal dynamic absorber layer on longitudinal wave propagation in a circular rod. Wavenumber-frequency solutions are derived analytically. The associated attenuation and phase velocity results are presented to show how their behavior depends on the loading treatment. Experimental results for the phase velocity are compared to a model developed by Dr. Dyer and Olivieri. A relaxation mechanism is developed to fully model the viscoelastic material. It is also shown that the interaction between longitudinal/flexural waves may lead to significant rates of transformation of the compressional wave energy into bending.

Thesis Supervisor:  
Title:

Professor Ira Dyer  
Weber-Shaughness Professor of Ocean Engineering, MIT

## Dedication

I would like to express my gratitude to many people whose invaluable contribution made this thesis possible.

Dr. Ira Dyer, for his wealth of insight, guidance and support for this work.

Dr. Richard Lyon and Dr. John Lienhard for their meaningful discussion and advice.

Ms. Marilyn Staruch and Mary Toscano.

My colleagues at MIT: Joe Bondaryk, Djamil Boulahbal, John Briggs, Chifang Chen, Matthew Conti, Chick Corrado Jr, Joe Deck, Kay Herbert, Tarun Kapoor, Kelvin LePage, Lan Liu, Charles Oppenheimer, Dave Ricks, Ken Rolt, Hee Chun Song, Da Jun Tang; and Alan, Brain, Larry of EECS.

A final note of thanks must go to my family. From them I derived the strength, determination and confidence to make it through and to continue moving forward.

I dedicate this thesis to the memory of Dad, Guozhong Meng and Hao Tang.

## Table of Contents

<b>Abstract</b>	<b>2</b>
<b>Dedication</b>	<b>3</b>
<b>Table of Contents</b>	<b>4</b>
<b>List of Figures</b>	<b>5</b>
<b>List of Tables</b>	<b>6</b>
<b>1. Introduction</b>	<b>7</b>
<b>2. Analytical Model</b>	<b>10</b>
2.1 Coupled Wave Equations	10
2.2 Resonance Characteristic and Relaxation Mechanism	14
2.3 Wavenumber Analysis	16
<b>3. The Experiment</b>	<b>28</b>
3.1 Experiment Design	28
3.2 Signal Conditioning	30
3.3 Data Acquisition and Spectrum Analysis	42
<b>4. Results</b>	<b>48</b>
4.1 Resonance Frequency and Loss Factor	48
4.2 Phase Speed From Cross Spectrum Function	49
4.3 Flexural-Longitudinal Wave Energy Ratio	51
<b>5. Conclusions</b>	<b>54</b>
<b>References</b>	<b>56</b>
<b>Appendix A: Computer Program for Wavenumber Analysis</b>	<b>60</b>
<b>Appendix B: Drive Point Impedance Diagram</b>	<b>62</b>
<b>Appendix C: Cross Spectrum Data</b>	<b>69</b>
<b>Appendix D: Longitudinal-Flexural Coupling Data(Symmetric Loading)</b>	<b>89</b>
<b>Appendix E: Longitudinal-Flexural Coupling Data(Asymmetric Loading)</b>	<b>108</b>

## List of Figures

Figure 1-1: Elements of a vibratory system	7
Figure 1-2: Schematic diagrams of dynamic equivalent vibratory systems, Ref[3]	8
Figure 1-3: Mass-spring-damper model of the dynamic absorber	9
Figure 2-1: Semi-infinite rod with dynamic absorber	10
Figure 2-2: Three-element spring and dashpot combination	15
Figure 2-3: Attenuation vs. normalized frequency ratio for $\beta=3, \eta=0.1,0.3,1.0$	18
Figure 2-4: Attenuation vs. normalized frequency ratio for $\eta=0.2, \beta=1,2,3$	19
Figure 2-5: Phase Speed vs. normalized frequency ratio for $\beta=3, \eta=0.1,0.3,1.0$	20
Figure 2-6: Phase Speed vs. normalized frequency ratio for $\eta=0.2, \beta=1,2,3$	21
Figure 2-7: Attenuation vs. $\omega_n$ for $\beta=3, N=1, \eta=0.1,0.34,1.0$	22
Figure 2-8: Attenuation vs. $\omega_n$ for $\eta=0.2, N=1, \beta=1,2,3$	23
Figure 2-9: Attenuation vs. $\omega_n$ for $\eta=0.2, \beta=3$ , changing N factor	24
Figure 2-10: Phase speed vs. $\omega_n$ for $\beta=3, N=1, \eta=0.1,0.34,1.0$	25
Figure 2-11: Phase speed vs. $\omega_n$ for $\eta=0.2, N=1, \beta=1,2,3$	26
Figure 2-12: Phase speed vs. $\omega_n$ for $\beta=3, \eta=0.2$ , changing N factor	27
Figure 3-1: Experiment apparatus	29
Figure 3-2: Resistance bridge with cancellation of flexural vibrations	30
Figure 3-3: Resistance bridge with cancellation of longitudinal vibrations	32
Figure 3-4: Decide the range of $R_t$ under the most unfavorable combinations of resistors	33
Figure 3-5: Six-channel circuit lay-out	34
Figure 3-6: AD624 functional block diagram	36
Figure 3-7: AD624 pin configuration	36
Figure 3-8: Noise interference problem, initial testing of the conditioning circuit	37
Figure 3-9: 60 Hz and its harmonic interfering noises, conditioning circuit with proper balance and ground	38
Figure 3-10: Response of pure tone excitation with battery supplied bridge circuits	39
Figure 3-11: Response of pure tone excitation with SNR larger than 30 dB	40
Figure 3-12: Noise interference problem in data aquisition using the Concurrent Computer	41
Figure 3-13: Data aquisition diagram	42
Figure 3-14: Clock connections on the CK10 and SH16FA modules	43
Figure 3-15: Sampling of a periodic timing signal	44
Figure 3-16: LWB modules in the data flow diagram	45
Figure 3-17: Synchronization virtual instrument	46
Figure 4-1: Phase speed vs. normalized frequency, $\omega_o = 2\pi f_o = 2\pi * 134.75$	50
Figure 4-2: Longitudinal to flexural coupling wave energy ratio	53
Figure 5-1: With wave propagation in the dynamic absorber layer	55

## List of Tables

<b>Table 3-I: AD624A specifications (@ <math>V_s = \pm 15\text{v}</math>, Gain = 100, <math>R_f = 2\text{k}\Omega</math> and <math>T_A = 25^\circ\text{C}</math></b>	<b>35</b>
<b>Table 4-I: Resonance frequency and loss factor</b>	<b>49</b>
<b>Table 4-II: Flexural/Longitudinal coupling wave energy ratio</b>	<b>52</b>

## Chapter 1

### Introduction

This study investigates the effect of a continuous longitudinal dynamic absorber layer on longitudinal wave propagation in a circular rod. Previous studies [21,22,36,42] relating vibration control to a continuous dynamic absorber layer focused on the attenuation of flexural or longitudinal wave propagation. In this study, an apparatus for measuring phase velocity and flexural/longitudinal wave coupling energy ratio is designed. In addition, a relaxation mechanism is employed to simulate the behavior of the isolator/dynamic absorber.

One of the basic principles in engineering is to start analysis with simple cases. For that reason, modeling of the dynamic absorber in several simple combinations of vibratory elements is studied here.

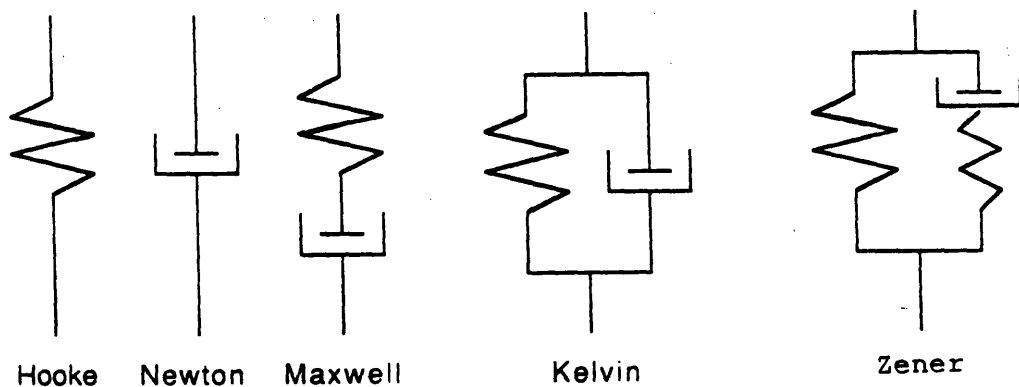


Figure 1-1: Elements of a vibratory system

The mechanical response of viscoelastic bodies are poorly represented by either a spring or a dashpot, which obey Hooke's law and Newton's law, respectively. J.C. Maxwell suggested a series combination of the spring and dashpot elements, which is merely a linear combination of perfectly elastic behavior and perfectly viscous behavior. Another simple element which has been used frequently in connection with viscoelastic behavior is the so-called Kelvin or Voigt model, with a spring and a dashpot in parallel. Creep and stress relaxation studies[2,3,13,14,33,38,39,40,43] reveal that the response of either Maxwell model or Kelvin model to several kinds of deformation does not fully represent some real damping systems. Different combinations of vibratory elements continue to appear in their applications, as cited by S.H.Crandall in the foreword of [33]: vibration theory was essentially complete - except for a realistic treatment of damping.

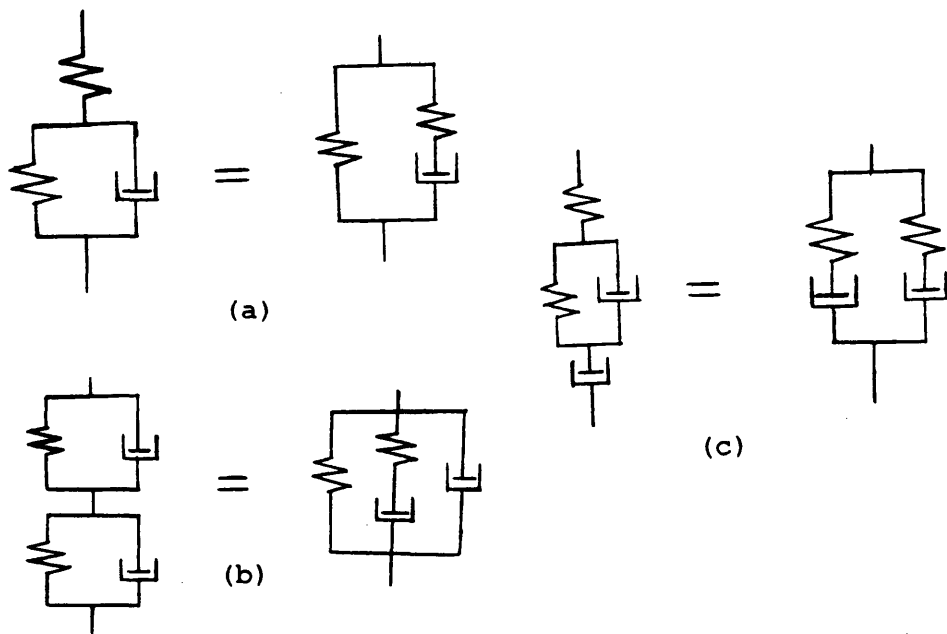


Figure 1-2: Schematic diagrams of dynamic equivalent vibratory systems, Ref[3]



When a spring is used as a vibration isolator and damped with a dashpot in parallel (right, the Kelvin or Voigt model) the conventional analysis accurately predicts force transmitted, deflection and damping loss. But when the elastic element is adhesive vinyl foam tape (also known as weatherstrip) with internal damping the conventional analysis may be in substantial error. For such a visco-elastic material, representation with a relaxation spring added in series with the dashpot (left, known as Zener model) more precisely simulates the behavior of the isolator. It is also regarded as possessing "one and one-half" degrees of freedom[23].

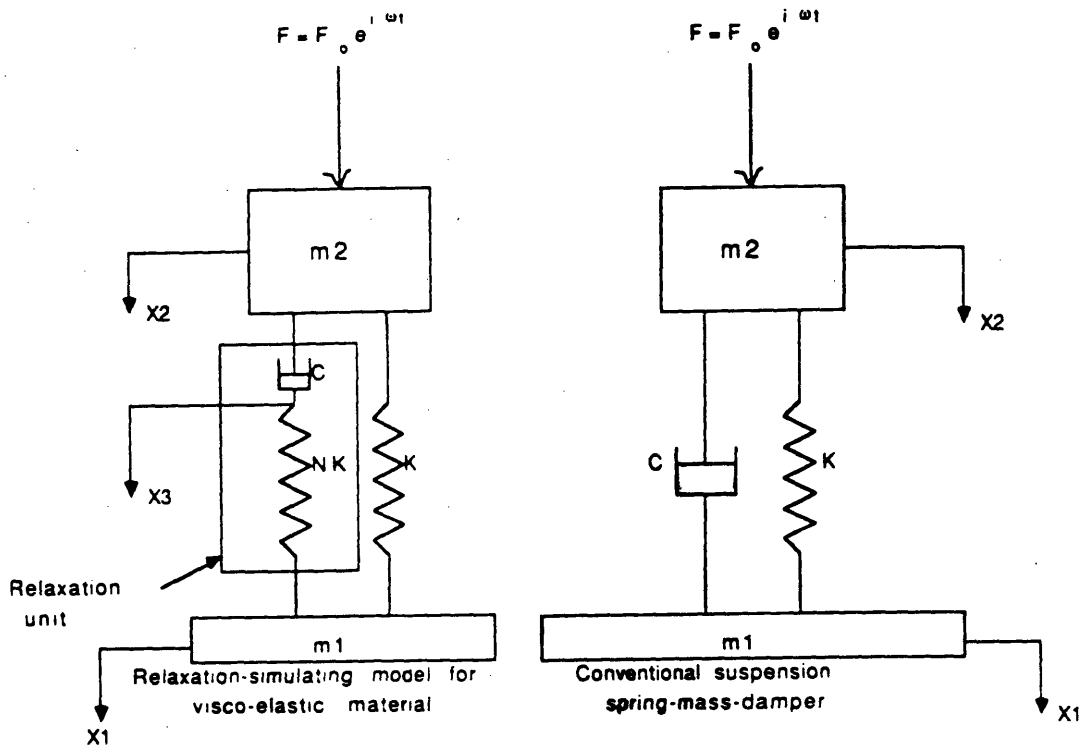


Figure 1-3: Mass-spring-damper model of the dynamic absorber

## Chapter 2

### Analytical Model

#### 2.1 Coupled Wave Equations

We first consider a infinite slender elastic rod with a continuously distributed layer of similar masses, springs and dashpots, transporting longitudinal waves (see Figure 2-1).

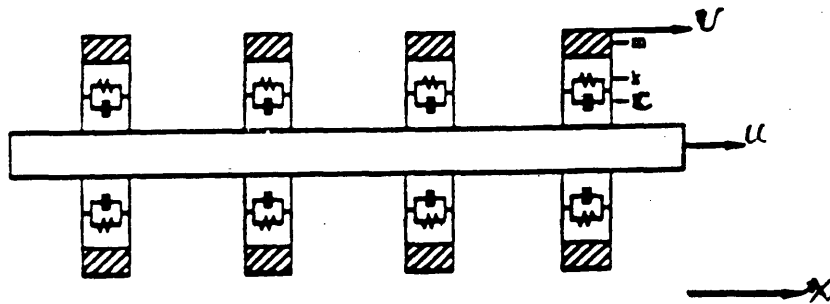


Figure 2-1: Semi-infinite rod with dynamic absorber

The equations of motion of this freely suspended rod with Kelvin coupling between  $u(x,t)$  and  $v(x,t)$  are:

$$m_2 \frac{\partial^2 u}{\partial t^2} + K(u-v) + C \frac{\partial}{\partial t}(u-v) = 0$$

$$m_1 \frac{\partial^2 v}{\partial t^2} + K_l(v-u) + C \frac{\partial}{\partial t}(v-u) = E_1 s_1 \frac{\partial^2 v}{\partial x^2}$$

where  $E_1$ ,  $m_1$ ,  $\rho_1$ ,  $s_1$  are modulus of elasticity, unit length mass, density and cross sectional area, of the rod,  $m_2$ ,  $C$ ,  $\rho_2$ ,  $K_l$  are the unit length mass, resistance, density and stiffness, of the dynamic absorber layer. Finally,  $u$  and  $v$  are longitudinal displacements of the rod and absorber, and  $\omega_0$  which follows is the natural resonance frequency of the absorber:

$$\omega_0^2 = \frac{K_l}{m_2}$$

The damped resonance frequency is usually approximated as  $\omega_d$ [7,43]:

$$\omega_d^2 = \omega_0^2(1-\zeta^2) \approx \omega_0^2$$

with the viscoelastic damping factor typically small, where

$$\zeta^2 = \frac{C^2}{4Kl m_1}$$

Since  $u$  and  $v$  are both space and time dependent, we assume the solution is harmonic and substitute  $-i\omega$  for the time derivatives

$$v = V \cdot e^{i(k \cdot x - \omega \cdot t)}$$

$$u = U \cdot e^{i(k \cdot x - \omega \cdot t)}$$

in the equation:

$$\frac{E_1}{\rho_1} \frac{\partial^2 v}{\partial t^2} - \frac{\partial^2 v}{\partial t^2} - \frac{K_l}{m_1}(v-u) - \frac{C}{m_1} \frac{\partial}{\partial t}(v-u) = 0$$

which corresponds to,

$$K^2V - K_1^2V + \frac{K_1\rho_1}{m_1E_1}(V-U) - i\frac{C\omega\rho_1}{m_1E_1}(V-U)=0$$

where

$$K_1^2 = \frac{\omega^2}{\frac{E_1}{\rho_1}}$$

We can normalize the above equation, with the following non-dimensional parameters:

$$\gamma = \frac{K}{K_1} \quad \text{ratio of wavenumber}$$

$$\beta = \frac{m_2}{m_1} \quad \text{mass ratio}$$

$$K_1 = \omega_0^2 m_2 \quad \text{stiffness}$$

$$\eta = \frac{C}{\omega_0 m_2} \quad \text{loss factor}$$

$$\omega_n = \frac{\omega}{\omega_0} \quad \text{normalized frequency}$$

Therefore the normalization yields the following equation:

$$\gamma^2V - V + \frac{\beta}{\omega_n^2}(V-U) - i\frac{\beta\eta}{\omega_n}(V-U)=0$$

The coupled equations can now be rewritten as:

$$\gamma^2V - V + \frac{\beta}{\omega_n^2}(V-U) - i\frac{\beta\eta}{\omega_n}(V-U)=0$$

$$-U + \frac{1}{\omega_n^2}(U-V) - i\frac{\eta}{\omega_n}(U-V)=0$$

This is a set of two coupled homogeneous linear equations in U and V. For a nontrivial solution to exist, the determinant of the coefficients must vanish. This leads to the dispersion relation:

$$\begin{vmatrix} \gamma^2 - 1 + \beta Y & -\beta Y \\ -Y & -1 + Y \end{vmatrix} = 0$$

with  $Y = \frac{1}{\omega_n^2} - \frac{i\eta}{\omega_n}$

$$(\gamma^2 - 1 + \beta Y)(-1 + Y) - \beta Y^2 = 0$$

$$\gamma^2(-1 + Y) + 1 - Y - \beta Y = 0$$

$$\gamma^2 = 1 + \frac{\beta}{1 - \frac{1}{Y}}$$

$$\gamma^2 = 1 + \frac{\beta}{\frac{\omega_n^2}{1 - i\eta\omega_n}}$$

The roots of this equation in the wavenumber  $\gamma$  represent a right going wave and a left going wave. Therefore, there are two different natural modes that can propagate in this semi-infinite rod with an absorber layer. Each mode, of course, can be left going and right going.

## 2.2 Resonance Characteristic and Relaxation Mechanism

For realistic treatment of damping influence in the vibration isolation, when we look at the indirectly coupled viscous damping Zener model[35], the complex ratio of stress or strain or, equally, the complex stiffness  $K^c$  of the three-element mounting may be written as

$$K^c = K + \frac{1}{(1/NK) + (1/i\eta\omega)}$$

It is readily shown that the stiffness approximately equals  $K$  at low frequency,  $K + i\eta\omega$  near resonance, and  $K + NK$  at high frequency. Therefore this is consistent with the concept of the mass-control, damping-control and stiffness-control regions of a dynamic absorber[24].

$$\begin{aligned}\omega_0^2 &= \frac{K^c}{m} \approx \frac{K + i\omega_0 C}{m} = \frac{K}{m} \left(1 + \frac{i\omega_0 C}{K}\right) \\ &\approx \frac{K}{m} \left(1 + \frac{i\omega_0 C}{2K}\right)^2\end{aligned}$$

In our light damping situation,

$$\frac{\omega C}{K}$$

is small near the resonance frequency. We shall therefore be able to approximate

$$\omega_0^2 \approx \frac{K}{m}$$

Following the analysis in the previous section, we can easily write down the wave equation for the three-element combination with Zener coupling as:

$$m_1 \ddot{x}_1 + K(x_1 - x_2) + NK(x_1 - x_3) = E_1 s_1 \frac{\partial^2 x_1}{\partial x^2}$$

$$m_2 \ddot{x}_2 + K(x_2 - x_1) + C(\dot{x}_2 - \dot{x}_3) = 0$$

$$NK(x_1 - x_3) + C(\dot{x}_2 - \dot{x}_3) = 0$$

where  $x_1, x_2, x_3$  are the displacements at points shown in Figure 2-2,  $N$  is the stiffness ratio of the relaxation spring over the main spring.

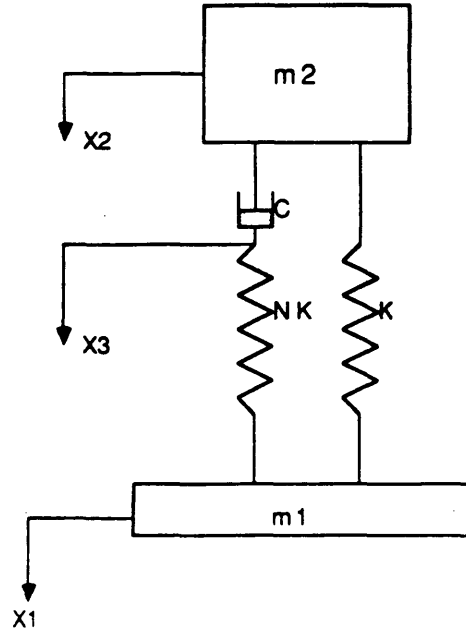


Figure 2-2: Three-element spring and dashpot combination

Again we assume a harmonic solution, substitute  $-i\omega$  for the time derivatives, and normalize with the same non-dimensional parameters.

$$x_1 = X_1 \cdot e^{i(k \cdot x - \omega \cdot t)}$$

$$x_2 = X_2 \cdot e^{i(k \cdot x - \omega \cdot t)}$$

$$x_3 = X_3 \cdot e^{i(k \cdot x - \omega \cdot t)}$$

$$(\gamma^2 - 1)X_1 + \beta(X_1 - X_2)/\omega_n^2 + N\beta(X_1 - X_3)/\omega_n^2 = 0$$

$$-X_2 + (X_2 - X_1)/\omega_n^2 - i\eta(X_2 - X_3)/\omega_n = 0$$

$$N(X_1 - X_3)/\omega_n^2 - i\eta(X_2 - X_3)/\omega_n = 0$$

The wavenumber-normalized frequency solution is thus obtained:





and

$$c_g = \frac{d\omega}{dK}$$

respectively.

The velocities  $c$  and  $c_g$  can be determined from the dispersion relation. To avoid some complex algebraic manipulation, we write a computer program (enclosed in Appendix A) solving for both the imaginary component and the real component of the wavenumber from the above dispersion relation, for both the relaxation (Zener) and non-relaxation (Kelvin) cases.

The following figures, which depict a lightly damped system with different mass ratios, show that both the peak and bandwidth of attenuation increase dramatically with increasing  $\beta$ , for both relaxation and non-relaxation models. These figures also reveal that with increasing loss factor, the attenuation and the phase speed peak drops considerably, for the non-relaxation model, but the attenuation bandwidth widens.

Furthermore, by increasing loss factor, the relaxation model predicts the attenuation and phase speed drop in the low damping region, increase in the high damping region, and possesses a transition frequency, which is referred to as optimum (attenuation is a maximum at the optimum damping point).

Analytical results are also obtained when holding mass ratio and loss factor unchanged, increasing the stiffness ratio  $N$  factor, which causes the attenuation and phase speed to drop.

The analytical model is therefore consistent with the concept of a dynamic absorber.

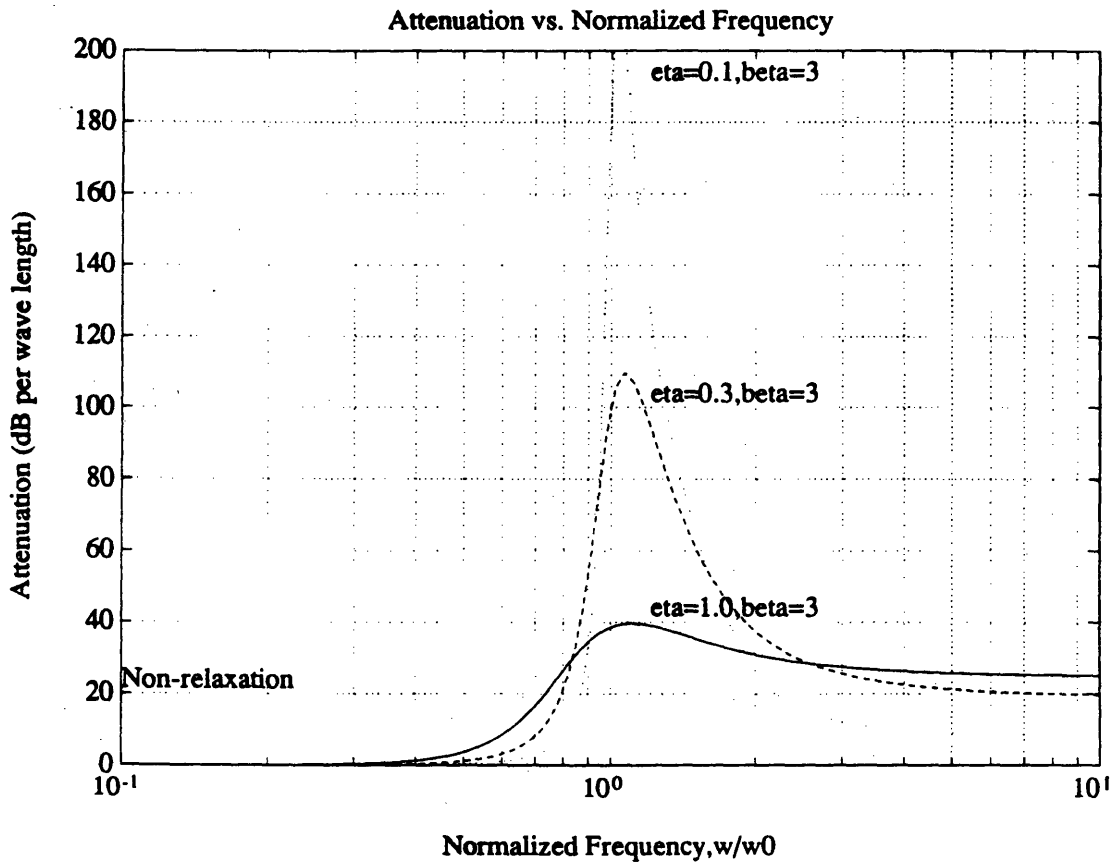


**Figure 2-3: Attenuation vs. normalized frequency ratio for  $\beta=3$ ,  $\eta=0.1, 0.3, 1.0$**

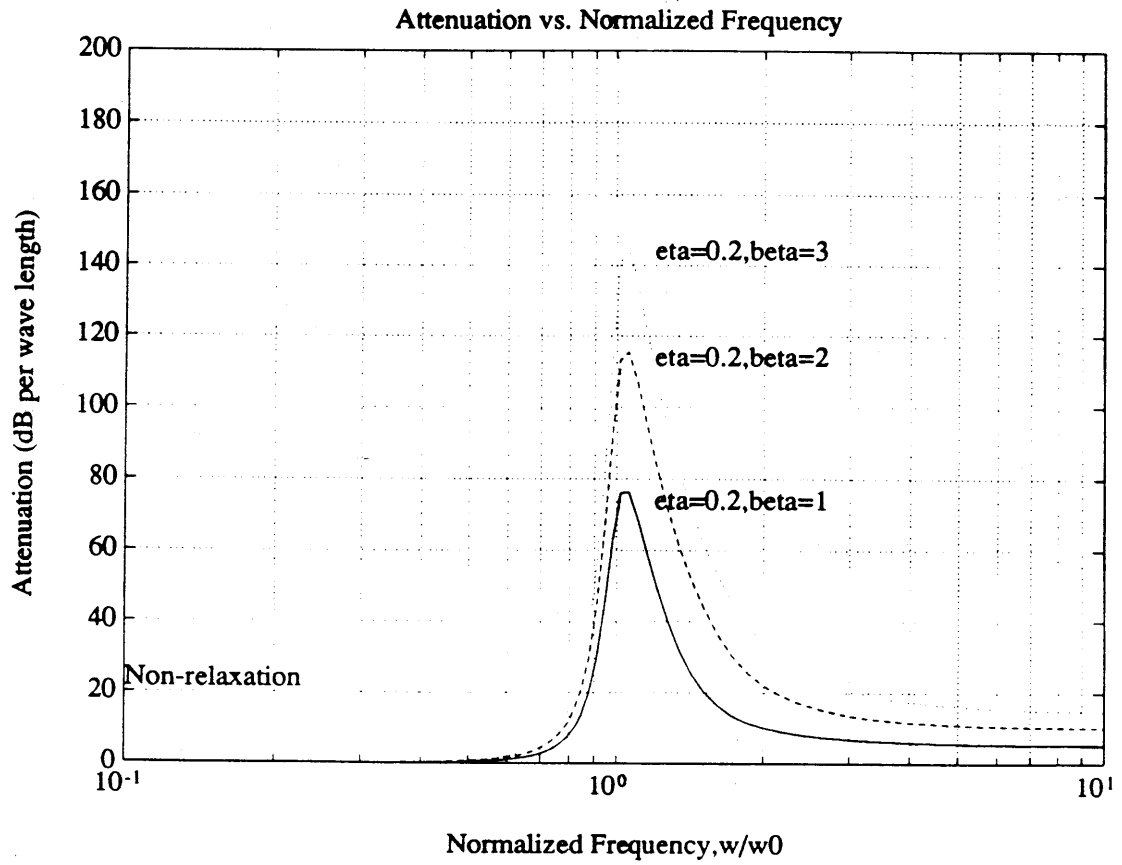


Figure 2-4: Attenuation vs. normalized frequency ratio for  $\eta=0.2$ ,  $\beta=1,2,3$

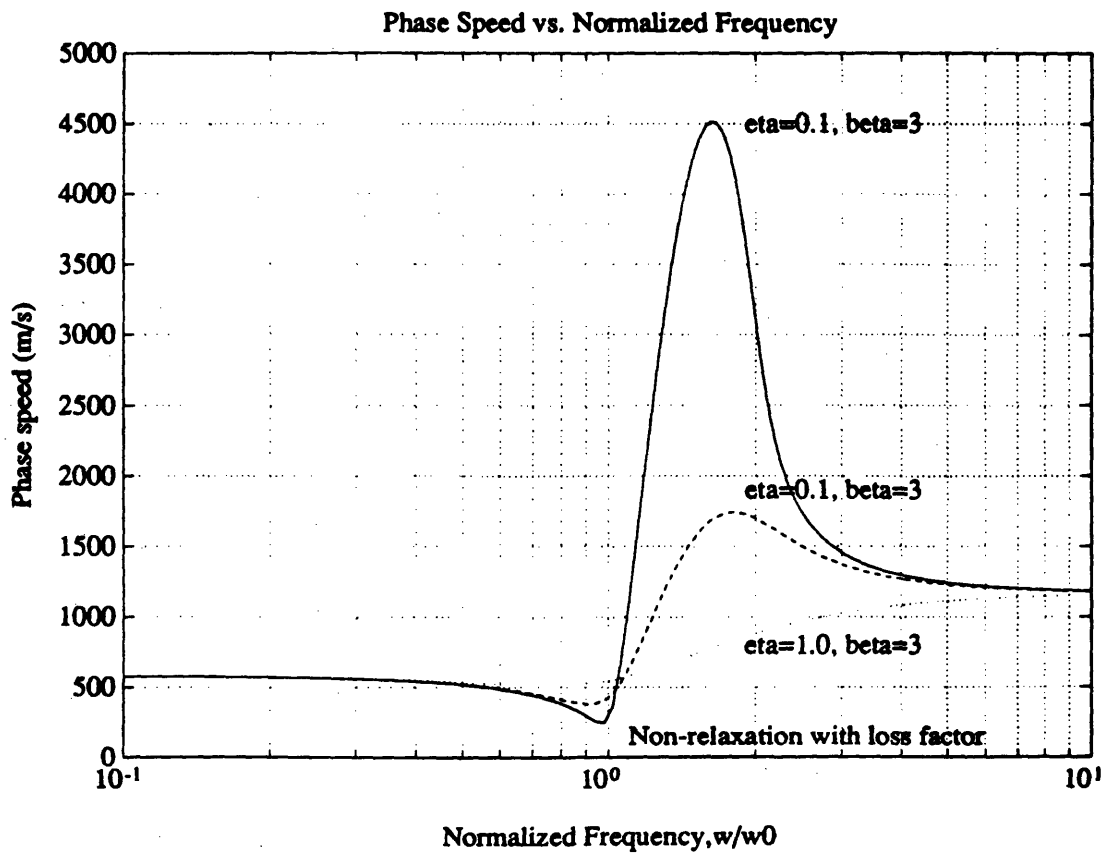


Figure 2-5: Phase Speed vs. normalized frequency ratio for  $\beta=3$ ,  $\eta=0.1, 0.3, 1.0$

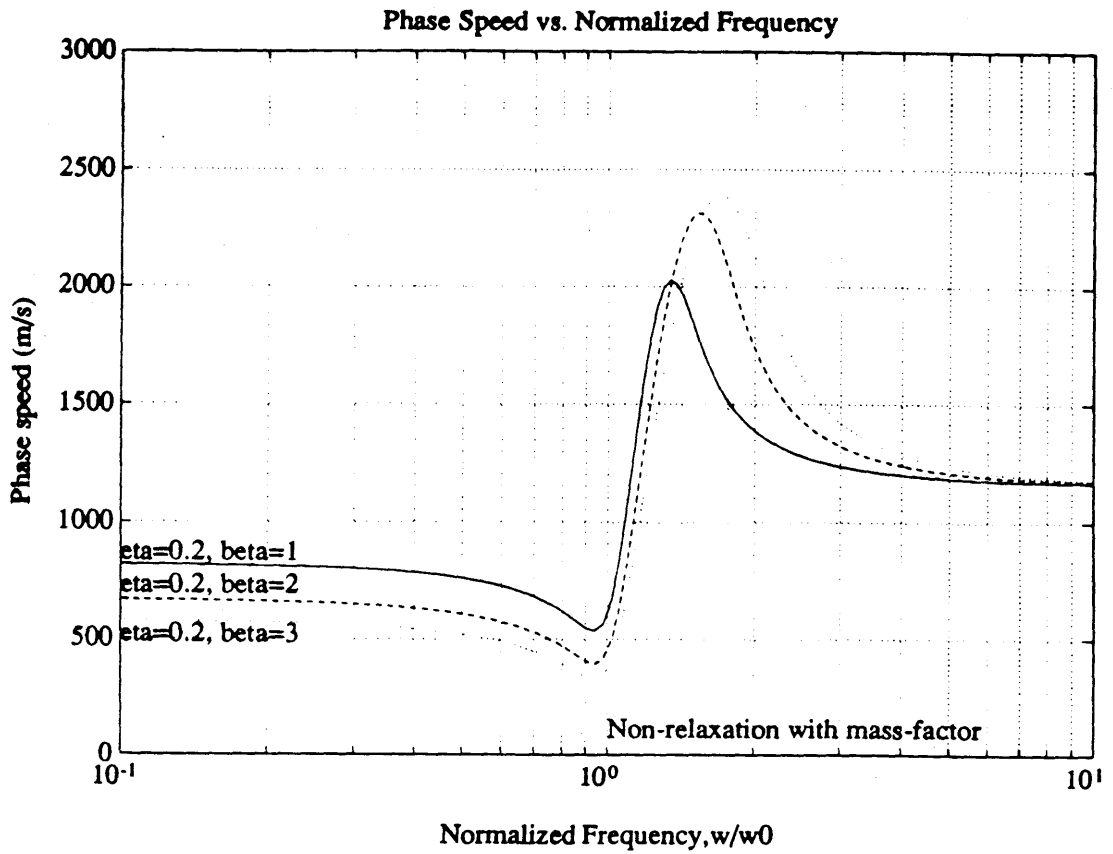


Figure 2-6: Phase Speed vs. normalized frequency ratio for  $\eta=0.2$ ,  $\beta=1,2,3$

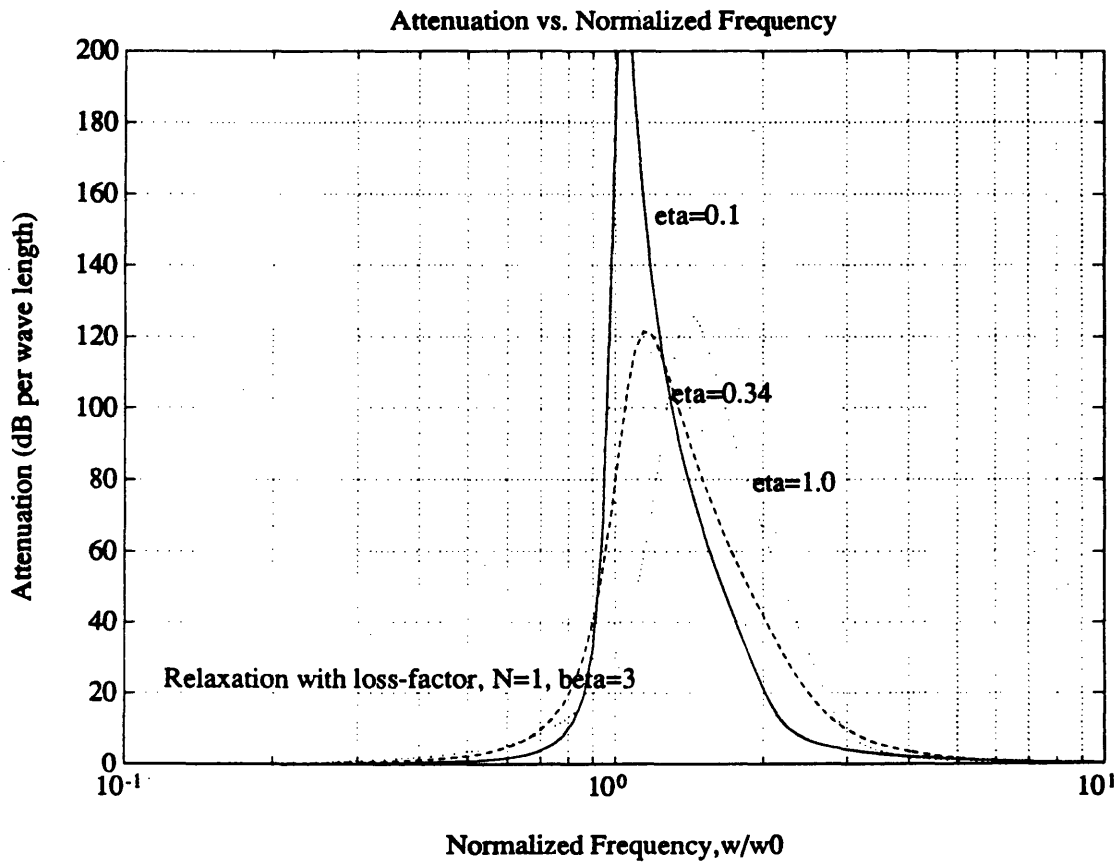


Figure 2-7: Attenuation vs.  $\omega_n$  for  $\beta=3$ ,  $N=1$ ,  
 $\eta=0.1, 0.34, 1.0$

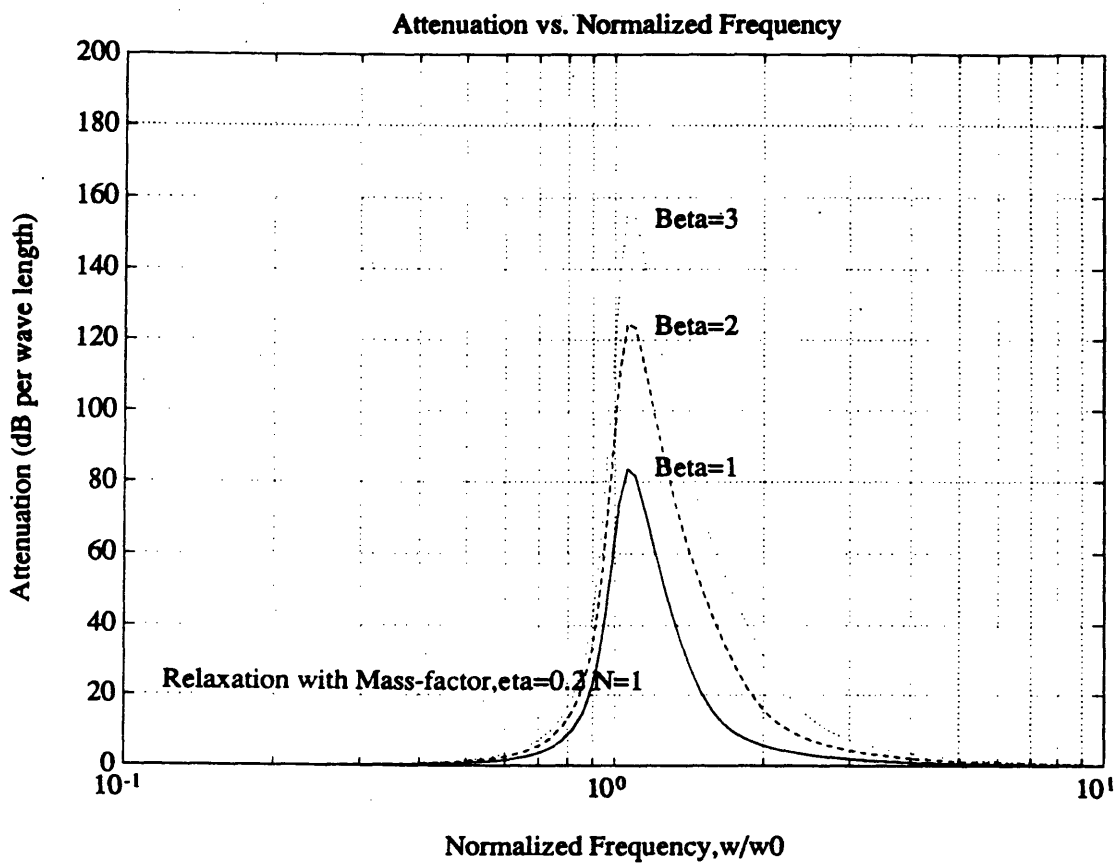
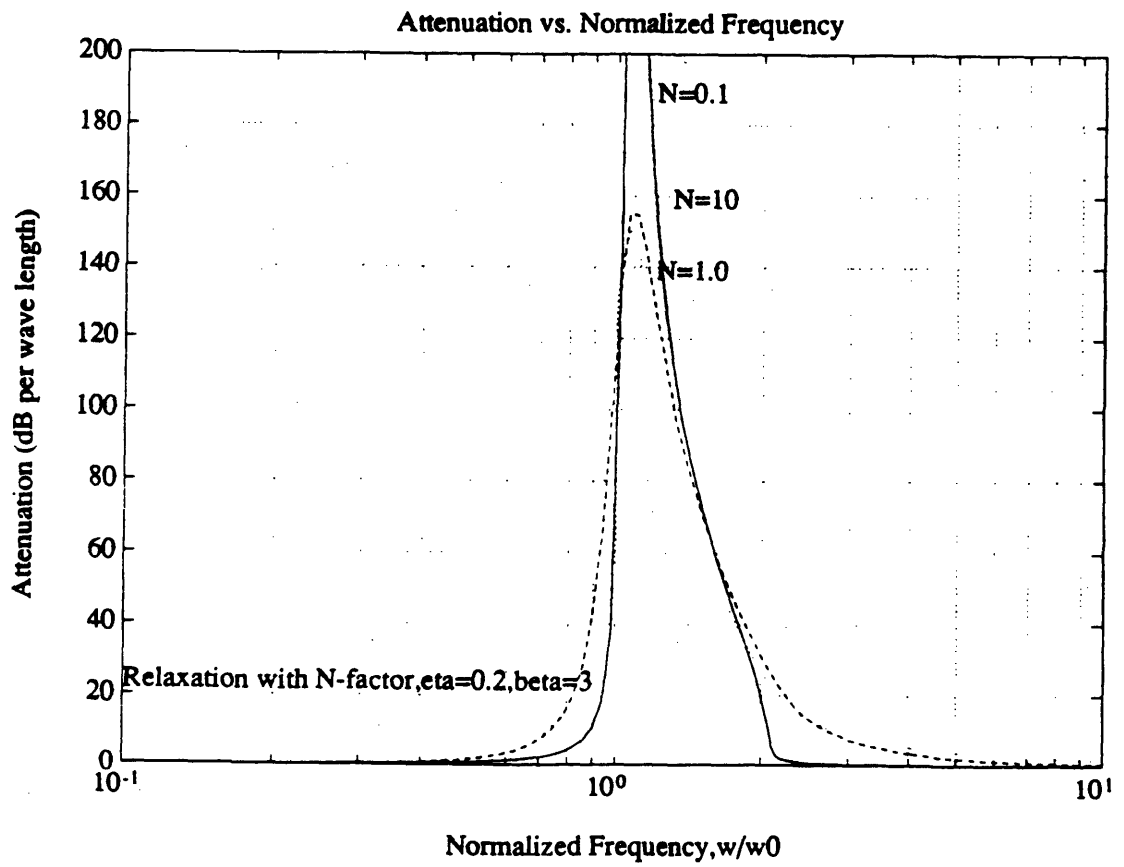
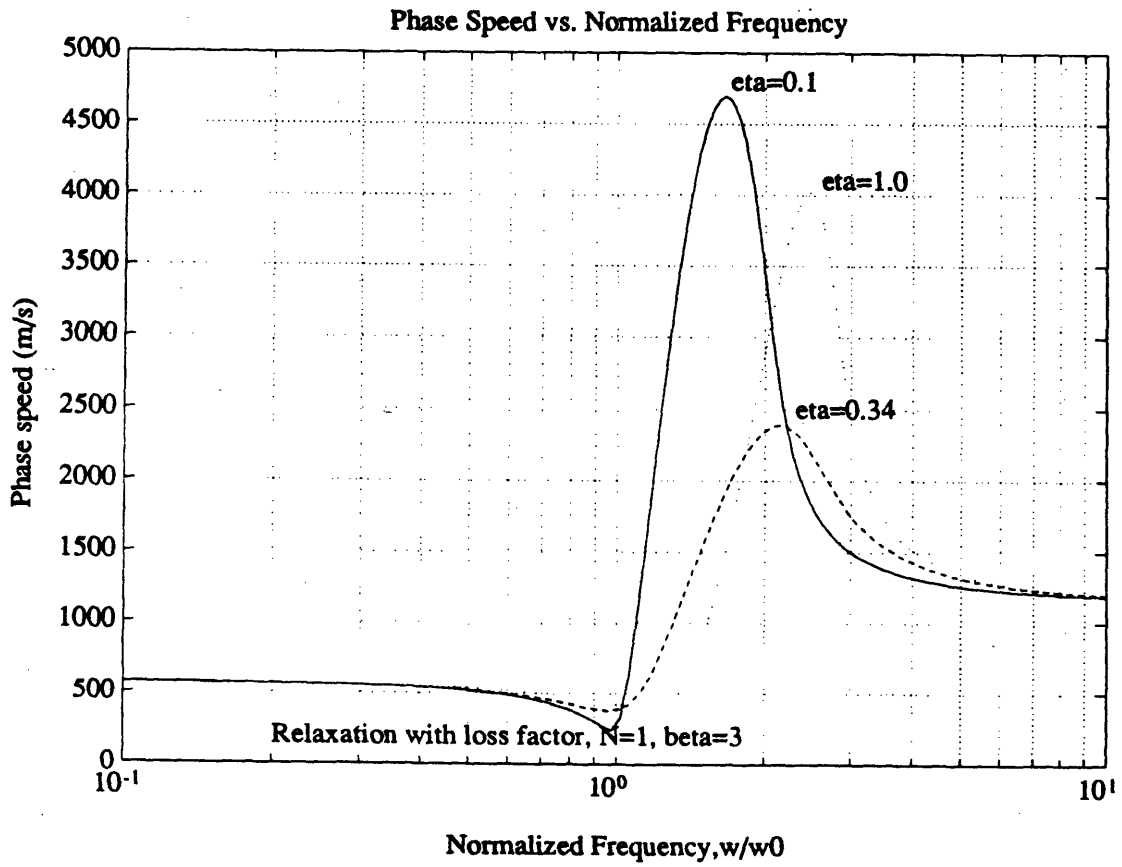


Figure 2-8: Attenuation vs.  $\omega_n$  for  $\eta=0.2$ ,  $N=1$ ,  
 $\beta=1,2,3$



**Figure 2-9: Attenuation vs.  $\omega_n$  for  $\eta=0.2, \beta=3$ , changing N factor**





**Figure 2-10: Phase speed vs.  $\omega_n$  for  $\beta=3$ ,  $N=1$ ,  $\eta=0.1, 0.34, 1.0$**

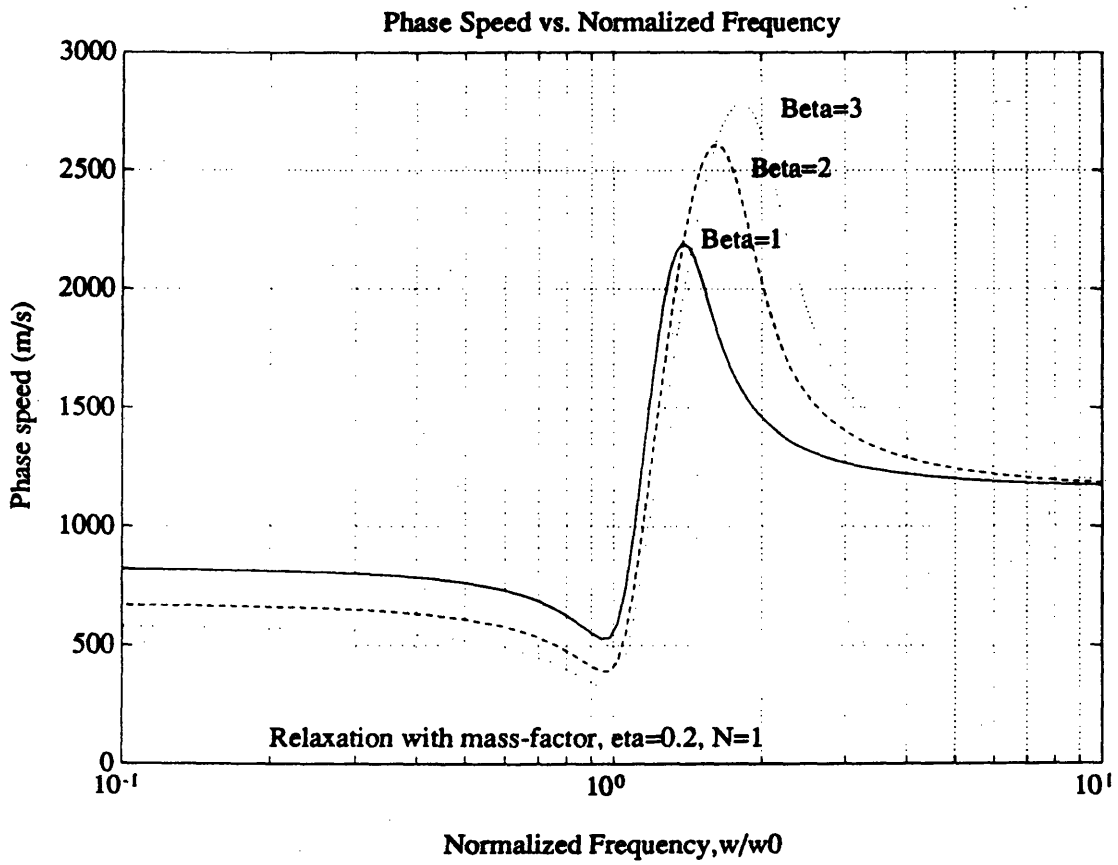


Figure 2-11: Phase speed vs.  $\omega_n$  for  $\eta=0.2$ ,  $N=1$ ,  
 $\beta=1,2,3$

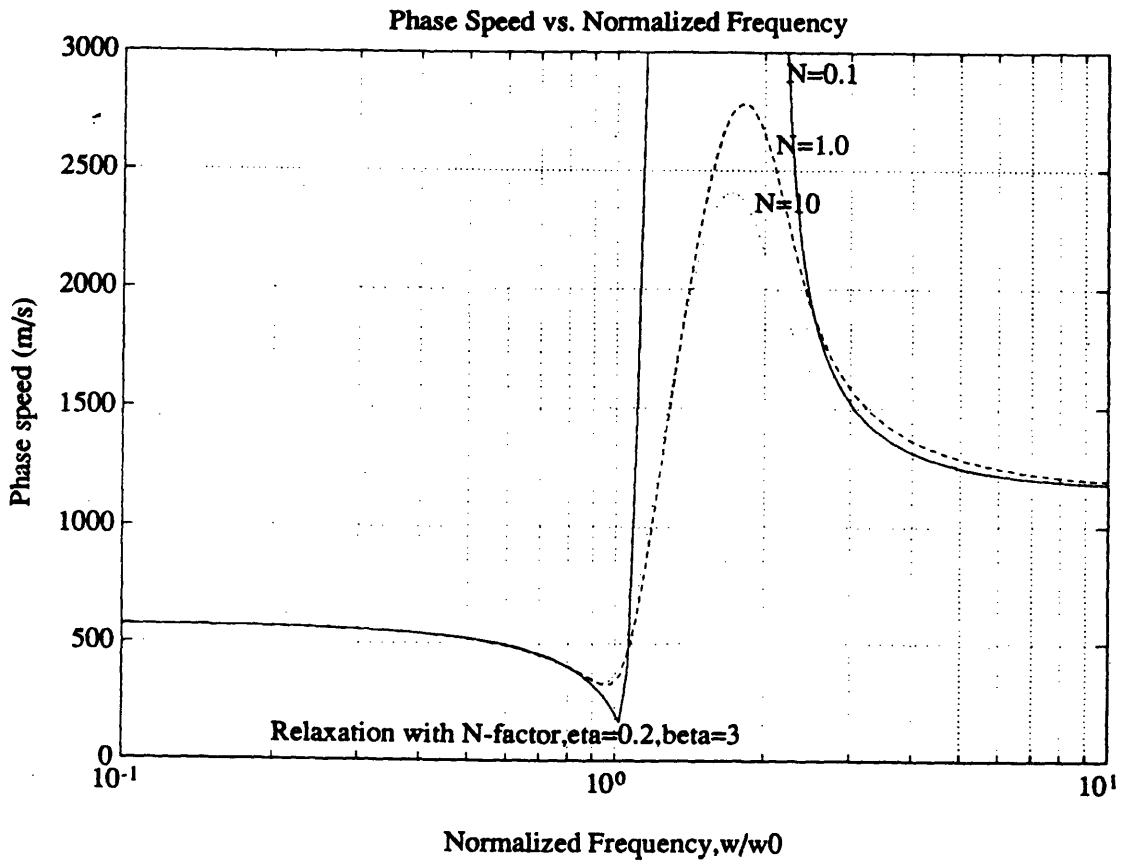


Figure 2-12: Phase speed vs.  $\omega_n$  for  $\beta=3, \eta=0.2$ , changing N factor

## Chapter 3

### The Experiment

#### 3.1 Experiment Design

An experiment should be planned to bring into prominence those factors to be studied and to enable their effects to be assessed in relation to the unavoidable errors of experimentation.

The first object to undertake an experimental investigation of wave propagation is to build an apparatus that closely resembles the analytical model: a thin elastic rod with a continuously distributed layer of masses, springs and dashpots, transporting longitudinal waves. A Delrin rod is a solid material used in Olivieri's experiment, which has a very low modulus of elasticity, an average density for a crystalline plastic and one-third of the compressional wave speed that is in steel or aluminum. The use of the Delrin rods was considered fixed, due to the desirability shown in Olivieri's experiment.

To simulate one dimensional propagation of longitudinal waves in an infinite medium, we dampen the propagating waves at the end of the test rod with sand. Enough sand is placed around the end of the rod to reduce wave reflection.

The other end of the rod (not immersed in sand) is drilled and fitted with a bolt, then connected tightly perpendicular to a Wilcoxon Research F1 shaker with a matching Z-602 impedance head.

Input to the shaker was provided by a signal generator with gain provided by a McIntosh power amplifier. The frequency range of the signals, limited by the linearity of the shaker, power amplifier and signal generator, is considered to be low-bounded by 40 Hz.

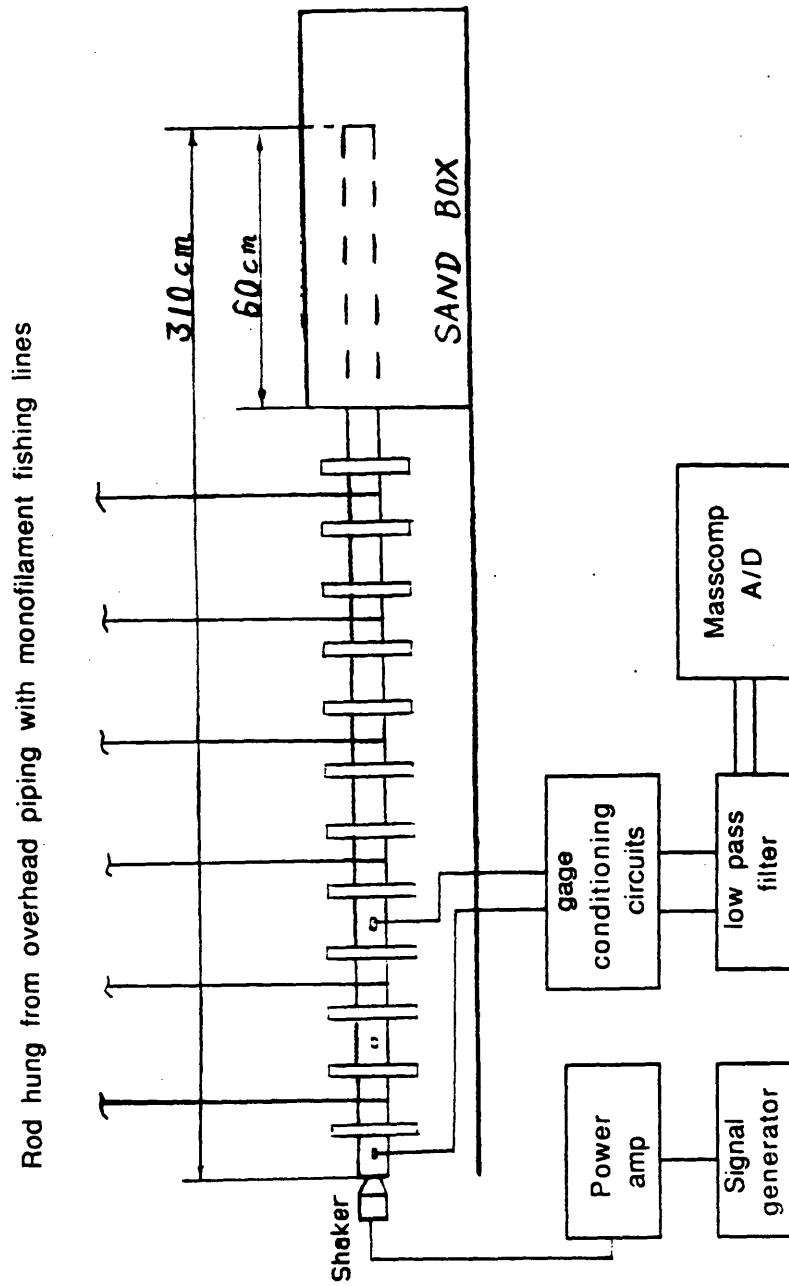


Figure 3-1: Experiment apparatus

Accelerometers, which were implemented in previous experiments[21,22,36,42] to measure attenuation spectra, are considered poor choices in measuring phase velocity and

wave coupling energy ratios, because of their phase lag and sensitivity axis difference, and high mass. Instead, strain gauges are used.

### 3.2 Signal Conditioning

In order to measure longitudinal and flexural waves separately, we need to investigate the strain gage balancing and amplifying circuits.

All commercial strain indicators employ some form of the following Wheatstone bridge circuit to detect the change of resistance in the gage with strain.

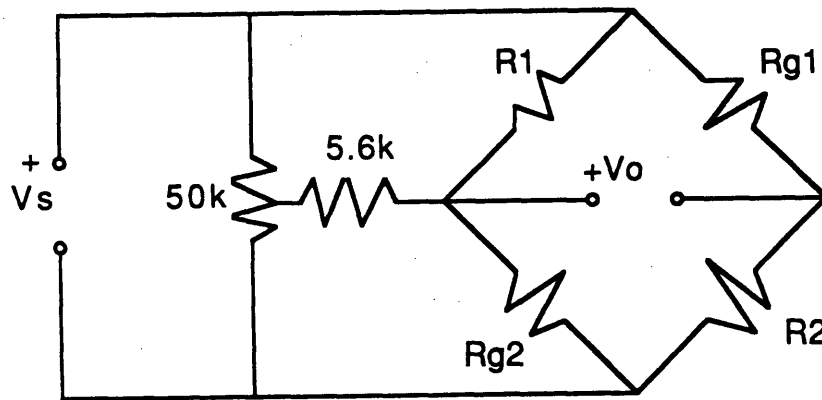


Figure 3-2: Resistance bridge with cancellation of flexural vibrations

In the above well-known Wheatstone circuit,  $v_s$  and  $v_o$  are the source and output voltage of the balancing circuit, respectively;  $R_{g1}$  and  $R_{g2}$  are two matched gages connected as nonadjacent arms of the bridge circuit (with the same length leadwires, they maintained identical temperature-compensation); and  $R_1$ ,  $R_2$  are reference resistors on the two other arms. We find:

$$\frac{v_o}{v_s} = \frac{R_{g2}}{R_1 + R_{g2}} - \frac{R_2}{R_{g1} + R_2}$$

where

$$R_{g2} = R_o + \Delta R_l - \Delta R_f$$

$$R_{g1} = R_o + \Delta R_l + \Delta R_f$$

$$R_1 = R_2 = R_o$$

where  $\Delta R_l$  and  $\Delta R_f$  donate to the resistance changes in the two strain gages mounted on the opposite side of the rod at the same distance from the drive point, which reflects the changes in resistance according to the longitudinal and flexural wave propagation. Then:

$$\begin{aligned} \frac{v_o}{v_s} &= \frac{\Delta R_l - \Delta R_f + R_o}{2R_o + \Delta R_l - \Delta R_f} - \frac{R_o}{2R_o + \Delta R_l + \Delta R_f} \\ &= \frac{1}{2} \left[ \frac{1 + \frac{(\Delta R_l - \Delta R_f)}{R_o}}{1 + \frac{(\Delta R_l - \Delta R_f)}{2R_o}} - \frac{1}{1 + \frac{(\Delta R_l + \Delta R_f)}{2R_o}} \right] \\ &\approx \frac{1}{2} \left[ \left(1 + \frac{\Delta R_l - \Delta R_f}{R_o}\right) \cdot \left(1 - \frac{\Delta R_l - \Delta R_f}{2R_o}\right) - \left(1 - \frac{\Delta R_l + \Delta R_f}{2R_o}\right) \right] \\ &= \frac{1}{2} \left[ \frac{\Delta R_l - \Delta R_f}{R_o} - \frac{\Delta R_l - \Delta R_f}{2R_o} - \frac{\Delta R_l + \Delta R_f}{R_o} + \frac{\Delta R_l + \Delta R_f}{2R_o} \right] \end{aligned}$$

With the obvious assumption  $\frac{\Delta R}{R_o} \ll 1$ , we obtain

$$\frac{v_o}{v_s} = \frac{\Delta R_l}{2R_o}$$

The change of resistance in the strain gage due to longitudinal strain is proportional to the gage factor  $F_g$  and actual strain  $\epsilon$  as  $\Delta R_l = F_g \cdot R_o \cdot \epsilon$  so the bridge circuit output voltage is  $v_o = v_s \cdot \frac{F_g \epsilon}{2}$ .

Recall in this case that the measurement cancels out the flexural modes and only contains the longitudinal modes.

In order to investigate the amount of flexural wave energy coupled from longitudinal excitation, the following circuit configuration is used:

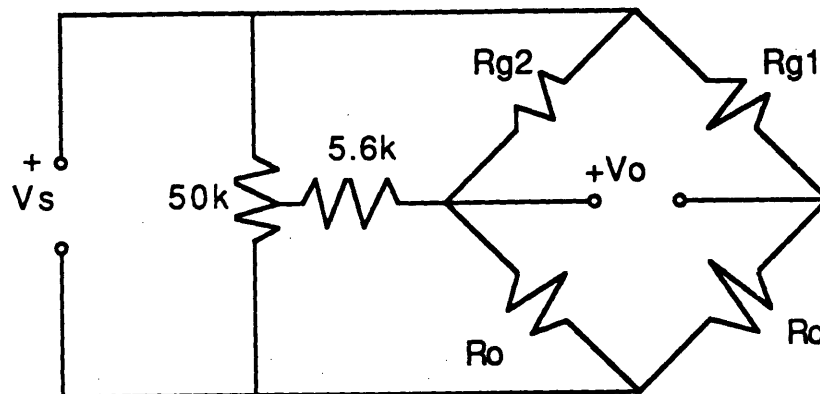


Figure 3-3: Resistance bridge with cancellation of longitudinal vibrations

where  $\frac{v_o}{v_s} = \frac{\Delta R_f}{2R_o}$  with the  $\frac{\Delta R}{R_o} \ll 1$  assumption.

In practice, a Wheatstone bridge is never precisely balanced as a result of the finite tolerances of the bridge resistors. Consequently, some method must be introduced to slightly change the resistance ratios of one side of the bridge. Thus, the pot and trim resistors are introduced as shown:



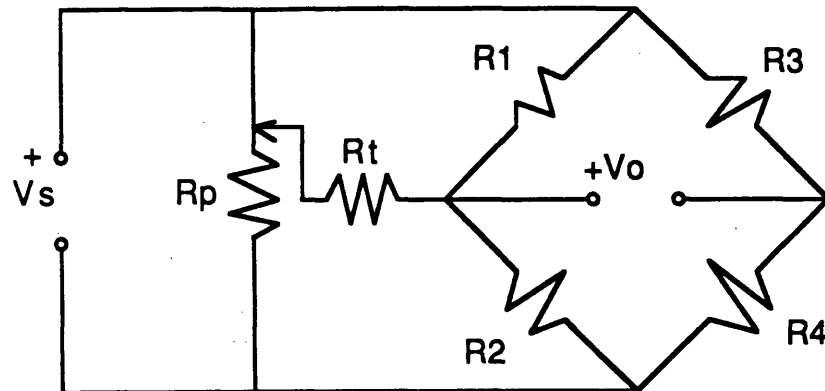


Figure 3-4: Decide the range of  $R_t$  under the most unfavorable combinations of resistors

Given that the resistors  $R_1, R_2, R_3, R_4$  are  $350.0\Omega \pm 0.3\%$  (for Micro-Measurement CEA series gages and carefully chosen reference resistors), the maximum value of  $R_t$ , for which the bridge can be balanced under the most unfavorable combination of resistors, is decided to be  $8.7\text{ k}\Omega$ . The  $50\text{ k}\Omega$   $R_p$  resistor draws little current and acts simply to control the voltage on one side of  $R_t$ .

We now construct this bridge circuit on a proto-board. With a Tektronix oscilloscope and a regulated power supply, we are able to balance the bridge to  $v_o$  less than or equal to  $25\text{ }\mu\text{v}$ .

Considering that the contact resistance at mechanical connections within the bridge circuit can lead to errors in the measurement of strain, a "wiggle" test is made on wires leading to the mechanical connections. The actual change in balance does occur, so we decided to wire-wrap and solder the bridge circuit on a Vector-board to insure that good connections have been made.

The following circuit layout diagram shows six channel balancing bridge circuits and their differential amplifiers:

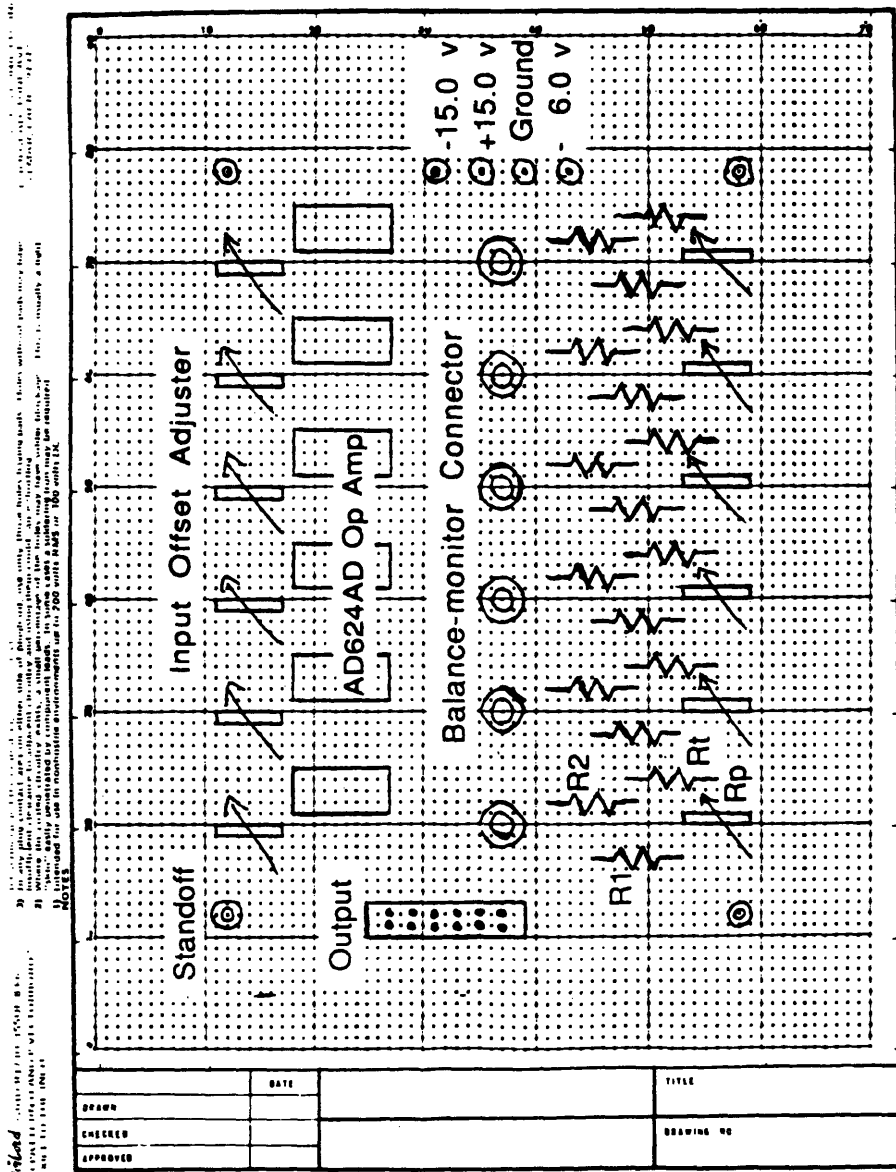


Figure 3-5: Six-channel circuit lay-out

**Table 3-I: AD624A specifications (@  $V_s = \pm 15\text{v}$ , Gain = 100,  $R_f = 2\text{k}\Omega$  and  $T_A = 25\text{ }^\circ\text{C}$ )**

Specification	Value	Unit
Gain Max Error	$\pm 1.0$	%
Gain Nonlinearity	$\pm 0.005$	%
Input voltage range (Max Differ. Input Linear)	$\pm 10$	v
Output rating	$\pm 10$	v
Dynamic response (small signal -3dB)	25	KHz
Slew Rate	75	$\mu\text{s}$
Power supply range	Min $\pm 5$ Max $\pm 18$ Typ $\pm 15$	v

The operational amplifier we chose is a AD624 precision instrumentation amplifier. The AD624 amplifier is designed primarily for use with low level transducers (including strain gages), with low noise, high gain accuracy, and low temperature coefficient. For the adjustable pretrimmed gain of 1000, the linearity range of the dynamic response is DC to 25 KHz. The  $5\text{V}/\mu\text{s}$  slew rate and  $15\text{ }\mu\text{s}$  settling time permit the use in our multiple channel, high sampling rate data acquisition applications.

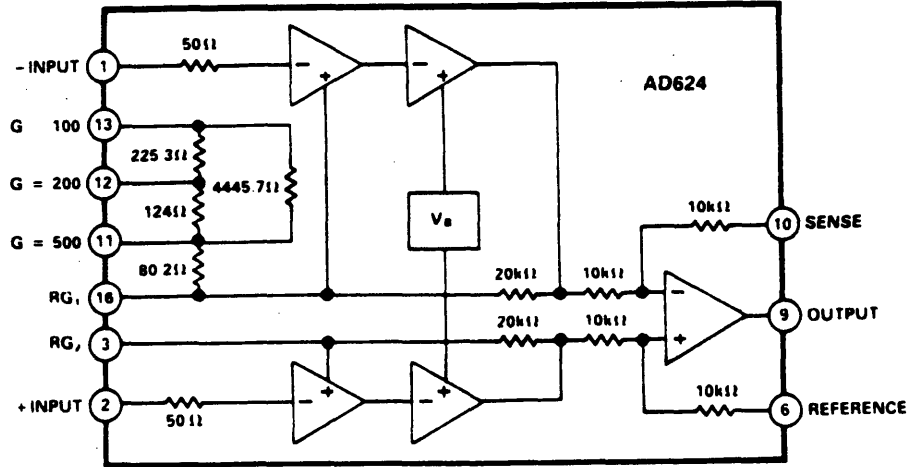


Figure 3-6: AD624 functional block diagram

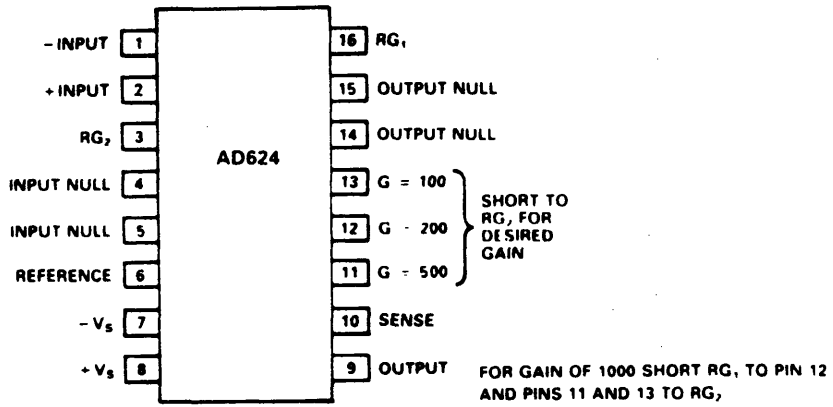


Figure 3-7: AD624 pin configuration

Too often in experiment designs, noise is considered to be one step down from the weather: hardly anyone even talks about it. Yet it is the noise level in a measurement circuit that ultimately limits the ability of that circuit to transmit faithfully the information carried by the signals being processed. To avoid a "noise-limited" statement that would likely appear in the "conclusion and discussion" chapter, we shall now incorporate into discussion the possible noise sources and their effects.

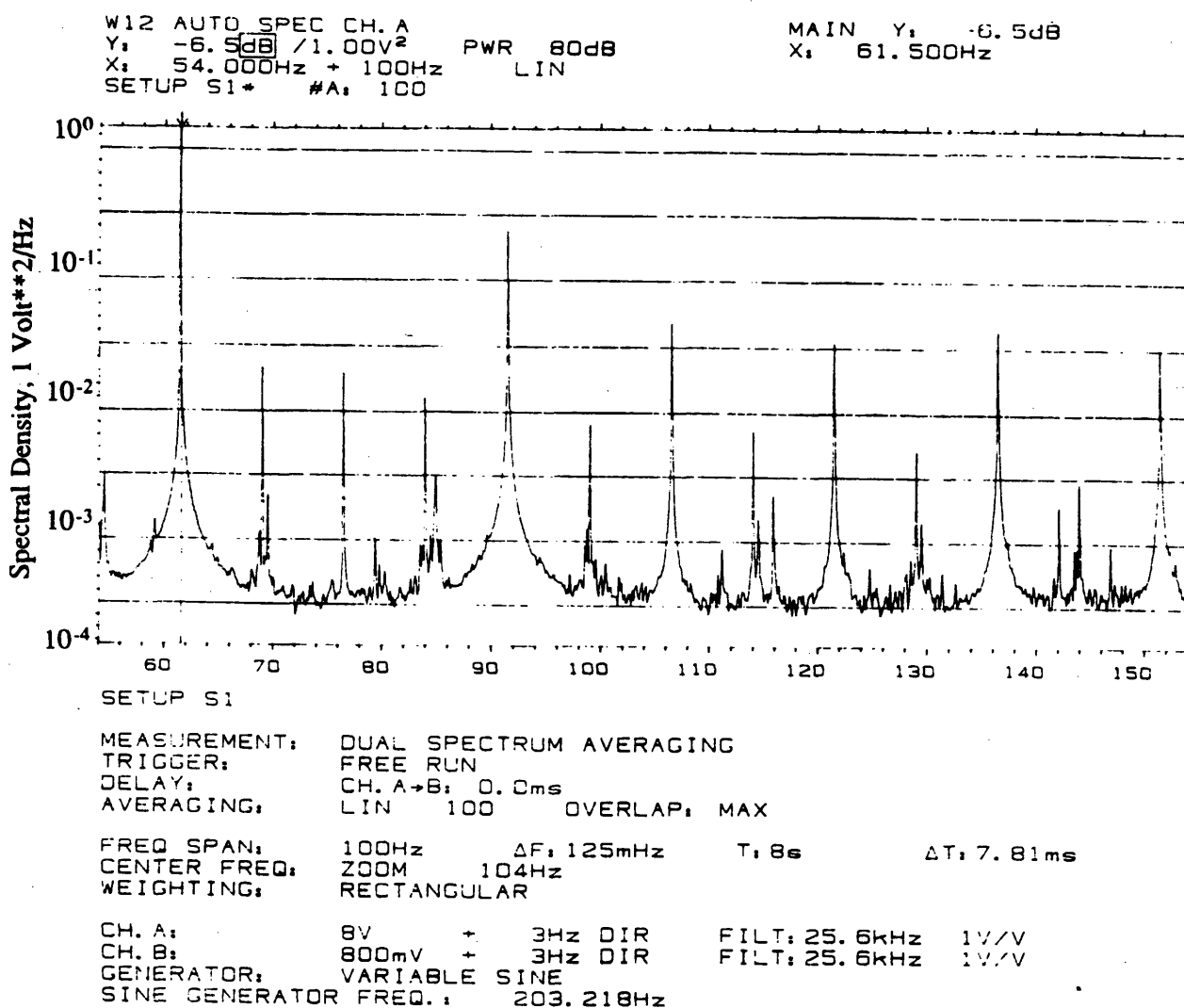


Figure 3-8: Noise interference problem, initial testing of the conditioning circuit

The interfering signals initially were dominated by the interference at 60 Hz and harmonics of 60 Hz, introduced at the Wheatstone bridge circuit. A test signal of a pure tone sine wave at 203 Hz is buried under the 60 Hz, and its harmonics (see Figure 3-9):

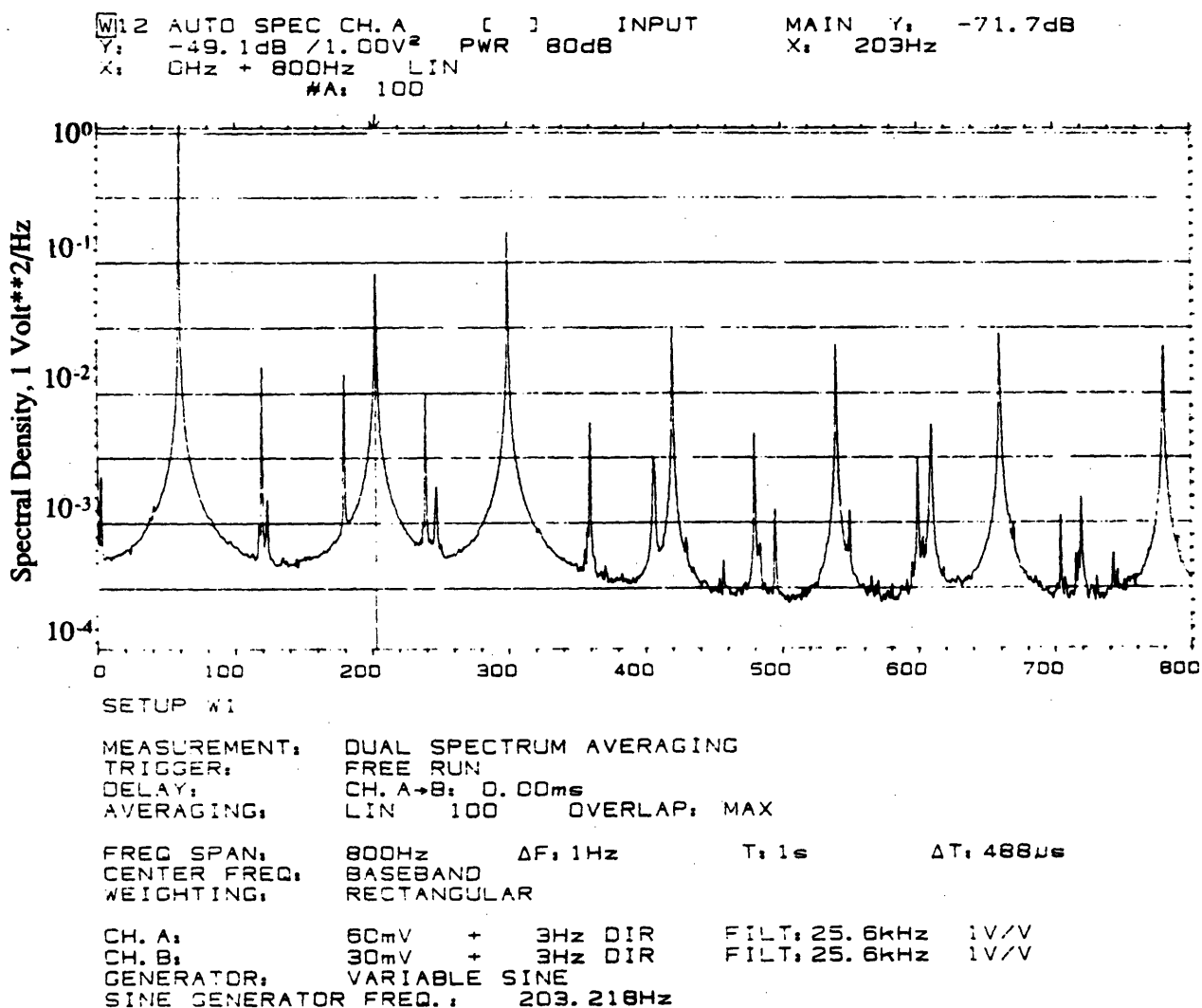


Figure 3-9: 60 Hz and its harmonic interfering noises, conditioning circuit with proper bala

By carefully studying the coupling between the power lines and the experiment apparatus, along with the use of power transformers and a regulated DC power supply, the interference is reduced by about 10 dB from Fig3-9 (as shown in Figure 3-9, Figure 3-10). With the battery supplied bridge circuits and DC transformer supplied operational amplifier, the signal to noise ratio is satisfactorily increased to larger than 30 dB.

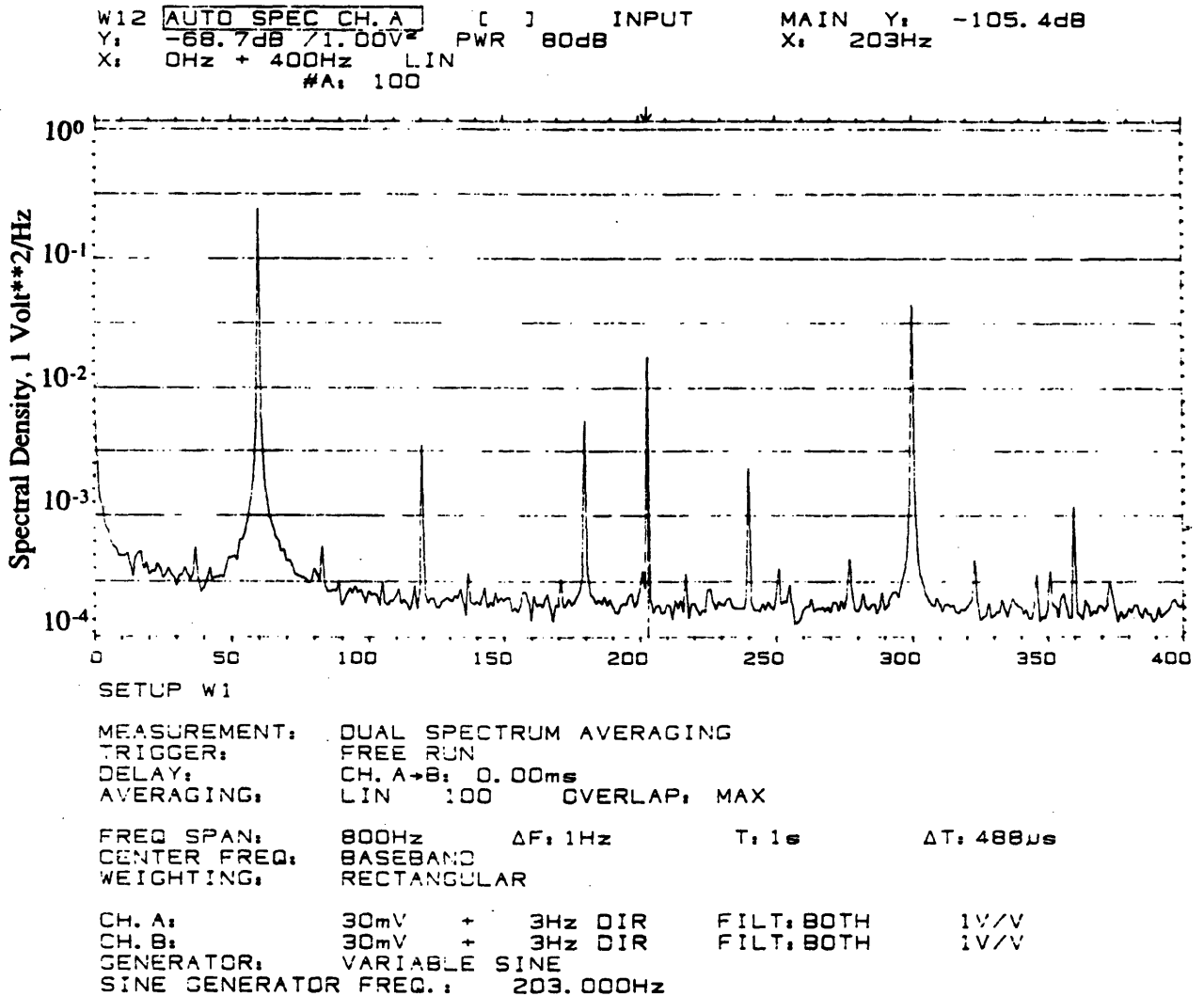


Figure 3-10: Response of pure tone excitation with battery supplied bridge circuits

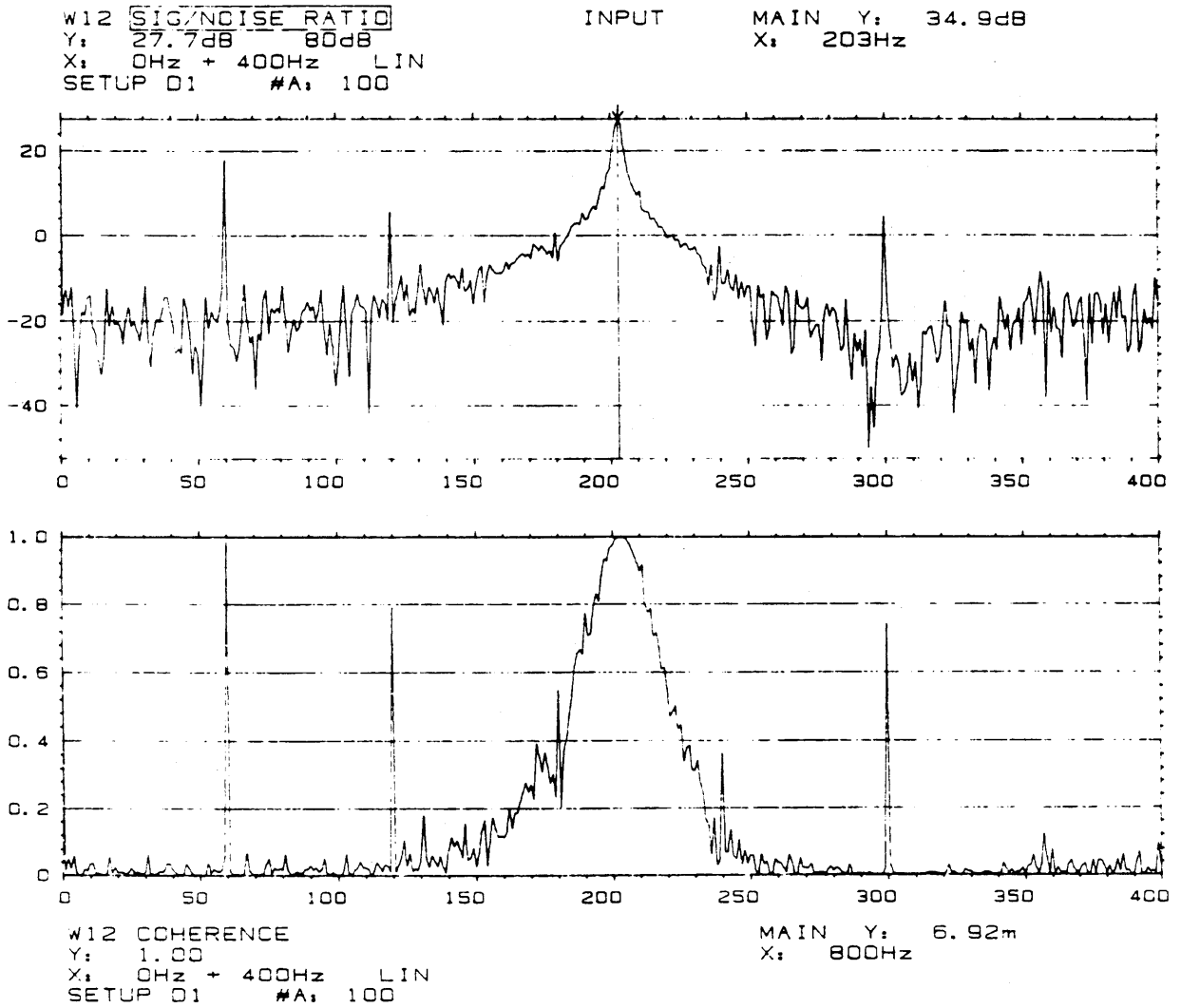
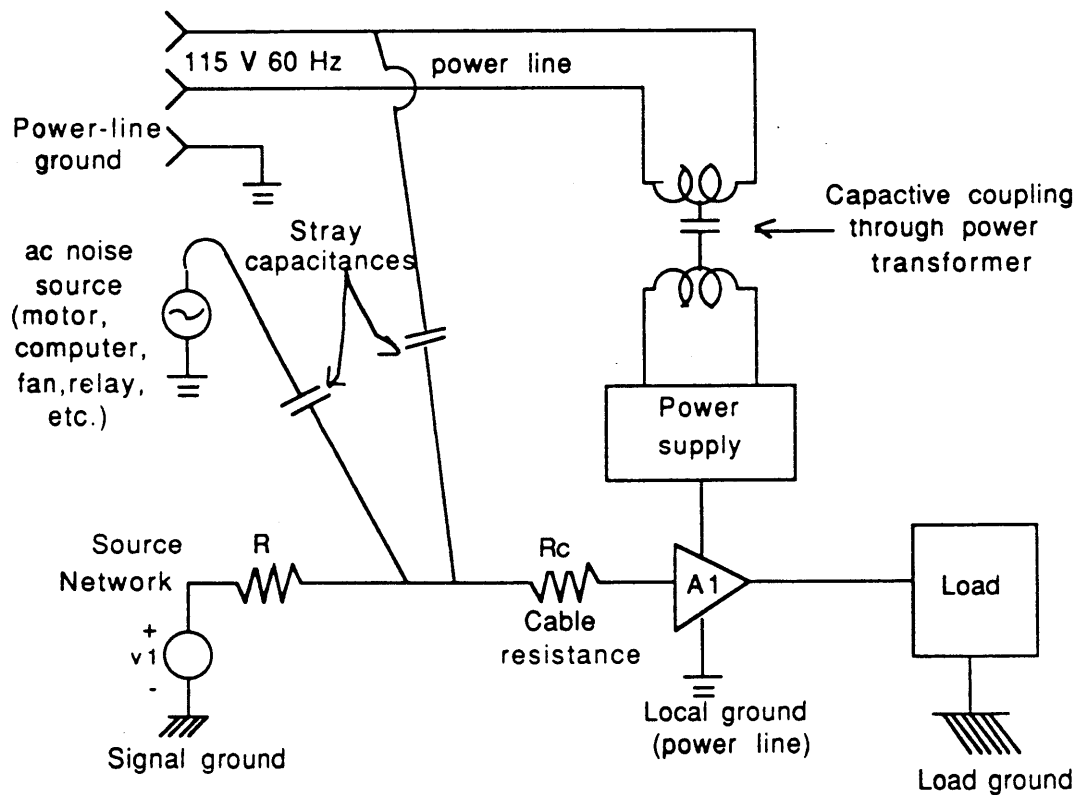


Figure 3-11: Response of pure tone excitation with SNR larger than 30 dB



The drifts in power supplies and amplifier offsets are controlled by the balancing adjustment in the circuit. The stray capacity fluctuations and electronic device noises are problems in data acquisition with the Concurrent Computer, as shown in Figure 3-12. With careful shielding, chase and signal grounding, wax-sealing the trimpot, and using the band-pass and low-pass filters, we finally achieve an excellent degree of noise isolation in the measurement apparatus.



### 3.3 Data Acquisition and Spectrum Analysis

The strain gage output is collected and digitized at the Acoustics and Vibration Lab using the Concurrent Computer.

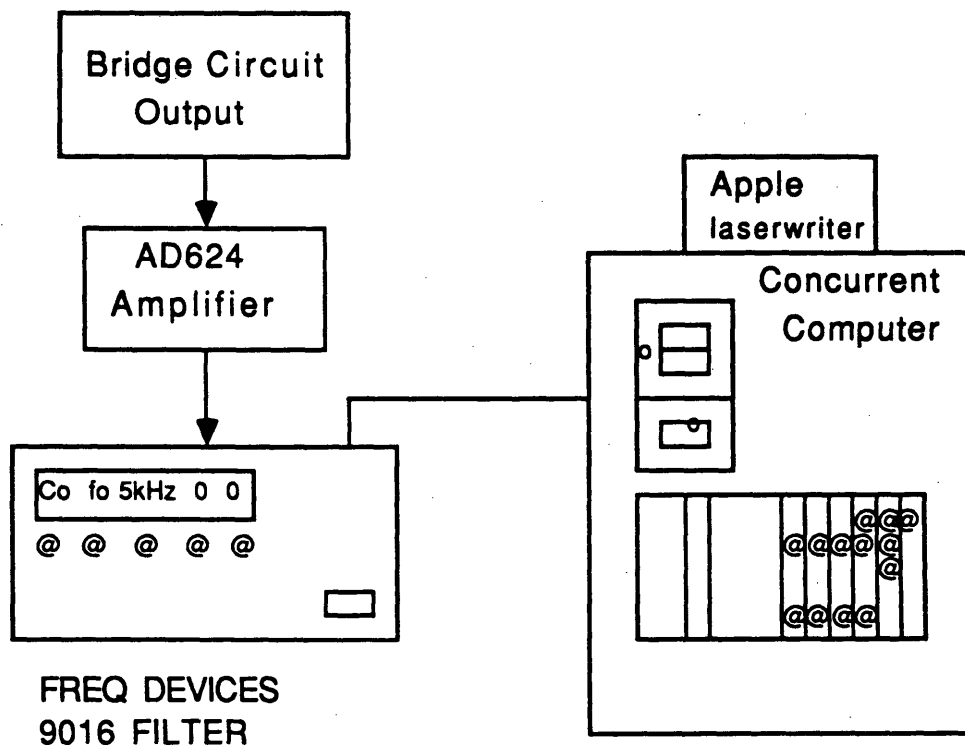


Figure 3-13: Data acquisition diagram

The analog input from the resistance bridge is amplified by the AD624 operational amplifier. After passing through the Frequency Devices 9016 programmable low pass filter, it is sampled, digitized and displayed with proper triggering, anti-aliasing, synchronizing and clipping.

The AD12FA analog/digital converter, along with a SH16FA sample and hold module, are used to digitize the data. Two analog/digital channels (Channel 0 and Channel 5) contain amplified signals for flexural and longitudinal waves, respectively.

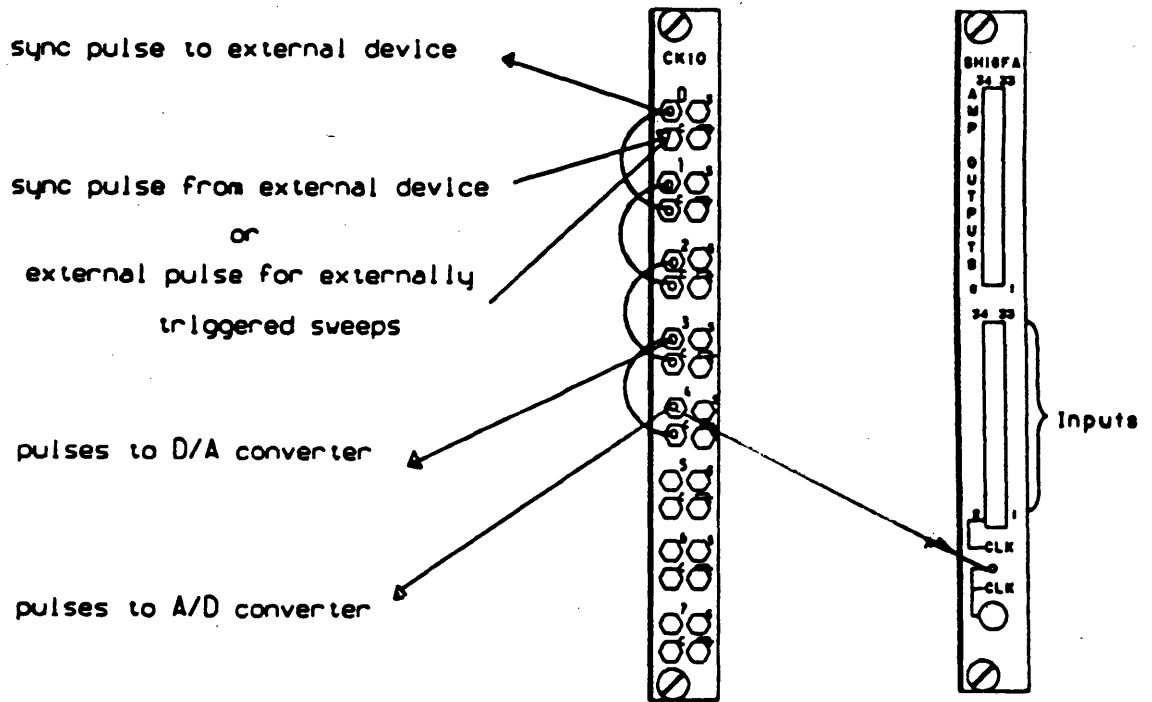


Figure 3-14: Clock connections on the CK10 and SH16FA modules

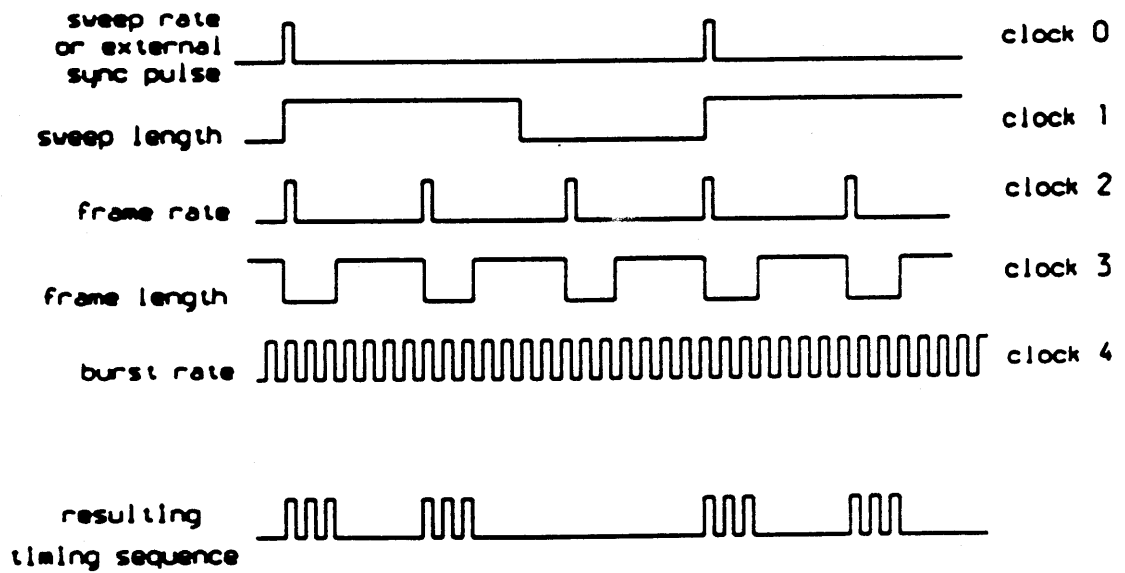


Figure 3-15: Sampling of a periodic timing signal

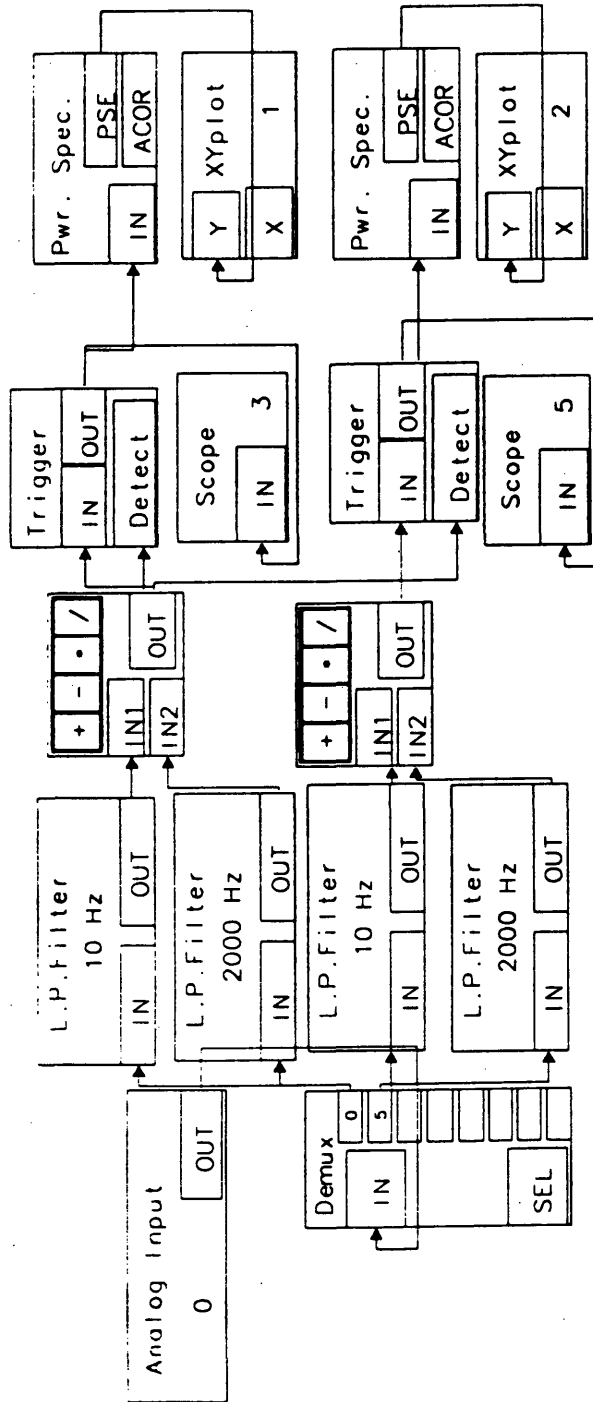


Figure 3-16: LWB modules in the data flow diagram

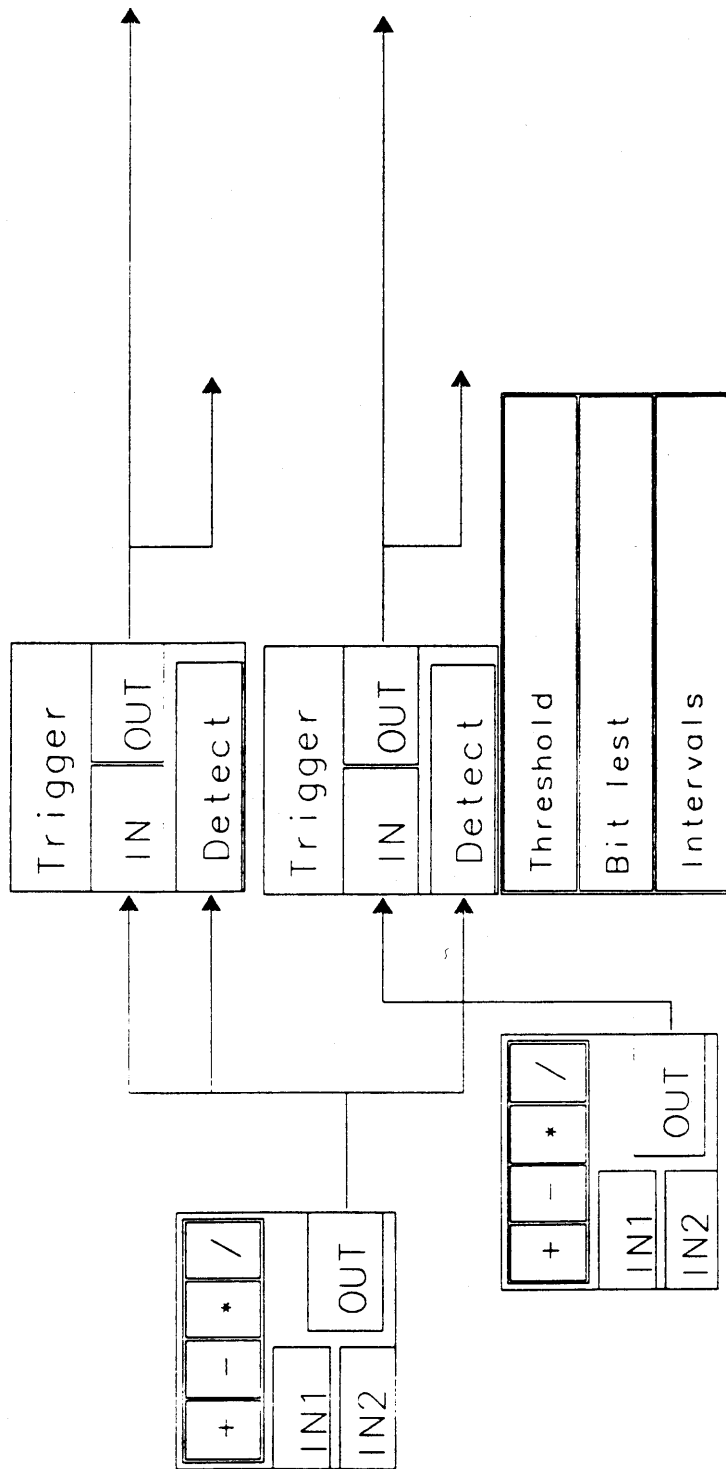


Figure 3-17: Synchronization virtual instrument

The data acquisition on the Concurrent Computer takes place inside the Lab Workbench (LWB) environment. The analog signal is demodulated using a demultiplexer module to separate channel 0 from channel 5 ( and multi-channel demodulating, when applicable).

The channel 0 signal provides the input for a trigger module that controls the data flow in both channels. The synchronization enables us to measure phase speed in the time domain. The trigger threshold and intervals are adjustable. This is of importance for future experimental investigations of multi-mode wave propagation problems.

The power spectra, defined as the Fourier transform of the input time series, are calculated and displayed with time series for both channels. We can now measure the ratio of energy transformation as a result of flexural wave coupling with longitudinal excitation.

## Chapter 4

### Results

#### 4.1 Resonance Frequency and Loss Factor

The quarter wavelength resonance frequency for a free rod of 3.10 m length, with a longitudinal nondispersive wave speed of 1161 m/s, is determined to be 93 Hz. Three tests are conducted to decide the resonance frequency for the Delrin rod with the attached dynamic absorber layer.

An impedance head is installed between the shaker and the contacting surface of the rod. The acceleration and force gage output from the impedance head are taken to the B & K spectrum analyzer.

The drive-point impedance (defined as force over velocity, which comes from integration of the acceleration) is obtained to decide the actual resonance frequency and loss factor.

The first actual resonance peak occurs at a much lower frequency than predicted and is considered to be caused by the resonance frequency of the shaker and sand termination problem, as addressed in Larry Olivieri's report[21].

In order to experimentally decide the loss factor, we conduct a test of the resonance frequency  $f_o$  and the half power bandwidth (-3dB down from both sides of  $f_o$ ). The loss factor  $\eta$  is defined as

$$\eta = \frac{\Delta f_{3dB}}{f_o}$$

for a system consisting of a short rod with a single isolator located very closely to the drive point(mass ratio is 3.2).



Three measurements are conducted and reveal the following results (Plots are enclosed in Appendix B):

Measurement freq. span	$f_o$ (Hz)	$f_{3dB\ low}$ (Hz)	$f_{3dB\ high}$ (Hz)	$\eta$
800	135	111	157	.341
400	134.5	109.5	156.5	.349
200	134.75	107.75	155.25	.353
Hz	$\bar{f}_o = 134.75$		$\bar{\eta} = .348$	

Table 4-I: Resonance frequency and loss factor

#### 4.2 Phase Speed From Cross Spectrum Function

The Fourier transform of the cross-correlation function, which is the expected value of the product of two time series, is defined as the cross-spectral density function (Cross Spectrum).

$$R_{xy}(\tau) = E [ y(t) x(t+\tau) ]$$

$$S_{xy}(f) = \int_{-\infty}^{\infty} R_{xy}(\tau) \cdot e^{-i2\pi f\tau} d\tau$$

The phase speed of the wave propagation can be determined from the frequency and the phase lag, through phase function  $\theta_{xy}(f)$  of the cross spectrum

$$\hat{S}_{xy}(f) = |\hat{S}_{xy}(f)| e^{-i\theta_{xy}(f)}$$

Using the B&K 2032 dual channel signal analyzer to measure the frequency response

of a series of pure tone longitudinal excitations to the rod, the phase speed is obtained and compared to the analytical prediction, where the crosses represent the experimental value.

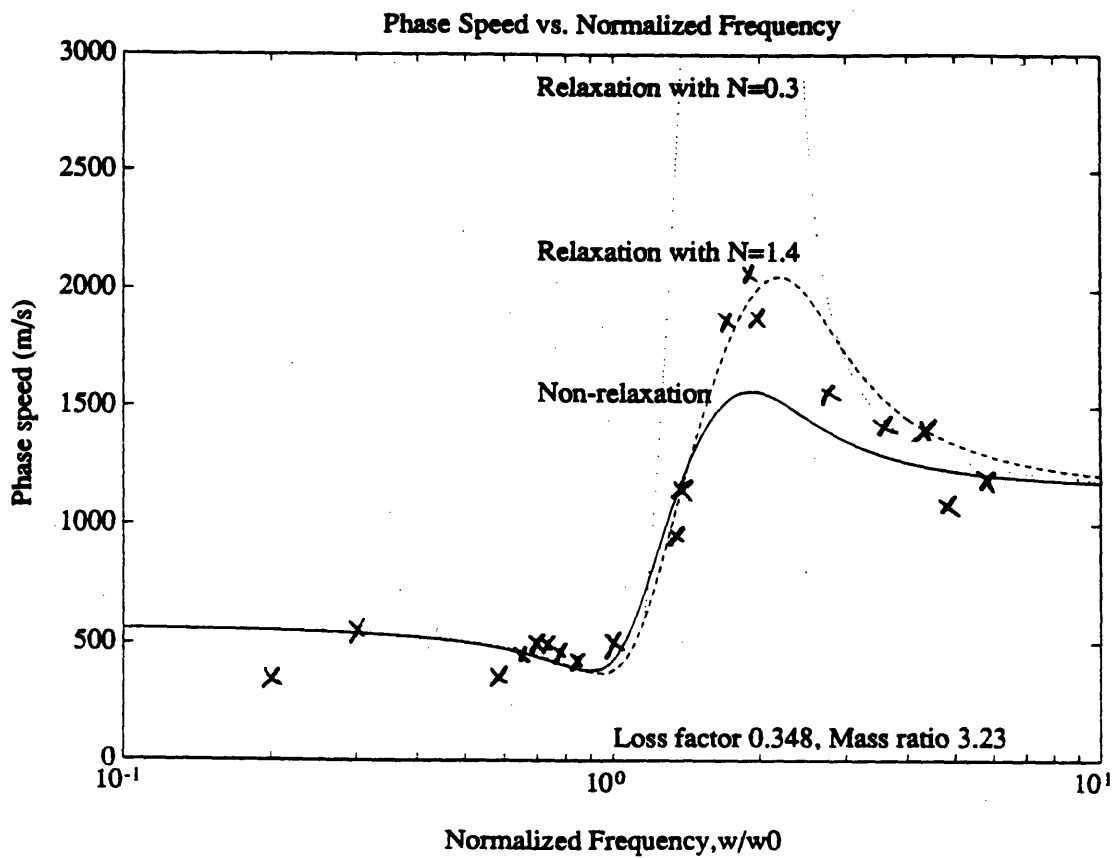


Figure 4-1: Phase speed vs. normalized frequency,  $\omega_0 = 2\pi f_0 = 2\pi * 134.75$

The experimental phase speed is dispersive, with shape as predicted, provided that  $N = 1.4$ . The good agreement in shape confirms the analytical model used and also that the attached mass system acts as a continuous longitudinal dynamic absorber. Although an independent measurement of  $N$  was not carried out, the Zener model seems to be a significant improvement over the Kelvin model.

### 4.3 Flexural-Longitudinal Wave Energy Ratio

Power densities referring to longitudinal and flexural wave energy are obtained from the output of two independent sets of strain gages, measuring simultaneously at the same distance away from the drive point. The ratio is presented in dB vs. normalized frequency, and the results reveal that the coupling from longitudinal excitation to a bending wave is much stronger at low frequency than at high frequency.

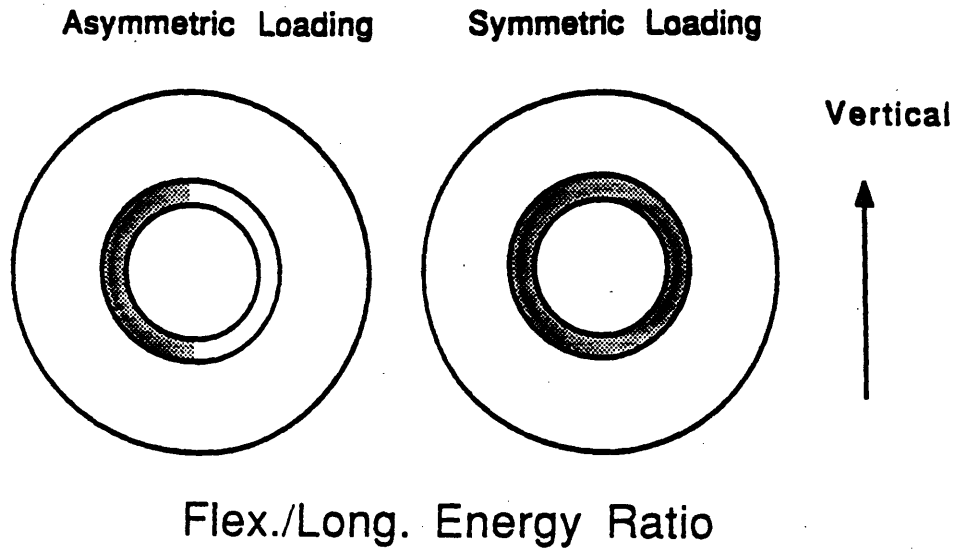
The estimated spectrum is calculated by Fourier transforming the auto-correlation function of the time series from a sample function, in conjunction with a "window" which is a weighting function applied to data to reduce the spectral leakage associated with the finite observation intervals.

By applying a Hamming window, the power spectra we calculated achieves -30dB down sidelobe level and good frequency resolution of .01 Hz, as shown in Appendix D and Appendix E.

In the symmetric loading case, the flexural wave is considered to be induced by the slight misalignment at the drive point, supporting fishing line, sand termination, and any other imperfections for longitudinal wave propagation.

The experiment results show that the longitudinal to flexural wave coupling is induced significantly by the asymmetric (disc mass adding through half circle weatherstrip to the rod) loading of the resiliently mounted masses. It is also shown in Figure 4-2 that both power spectra decrease linearly in logarithmic frequency scale.

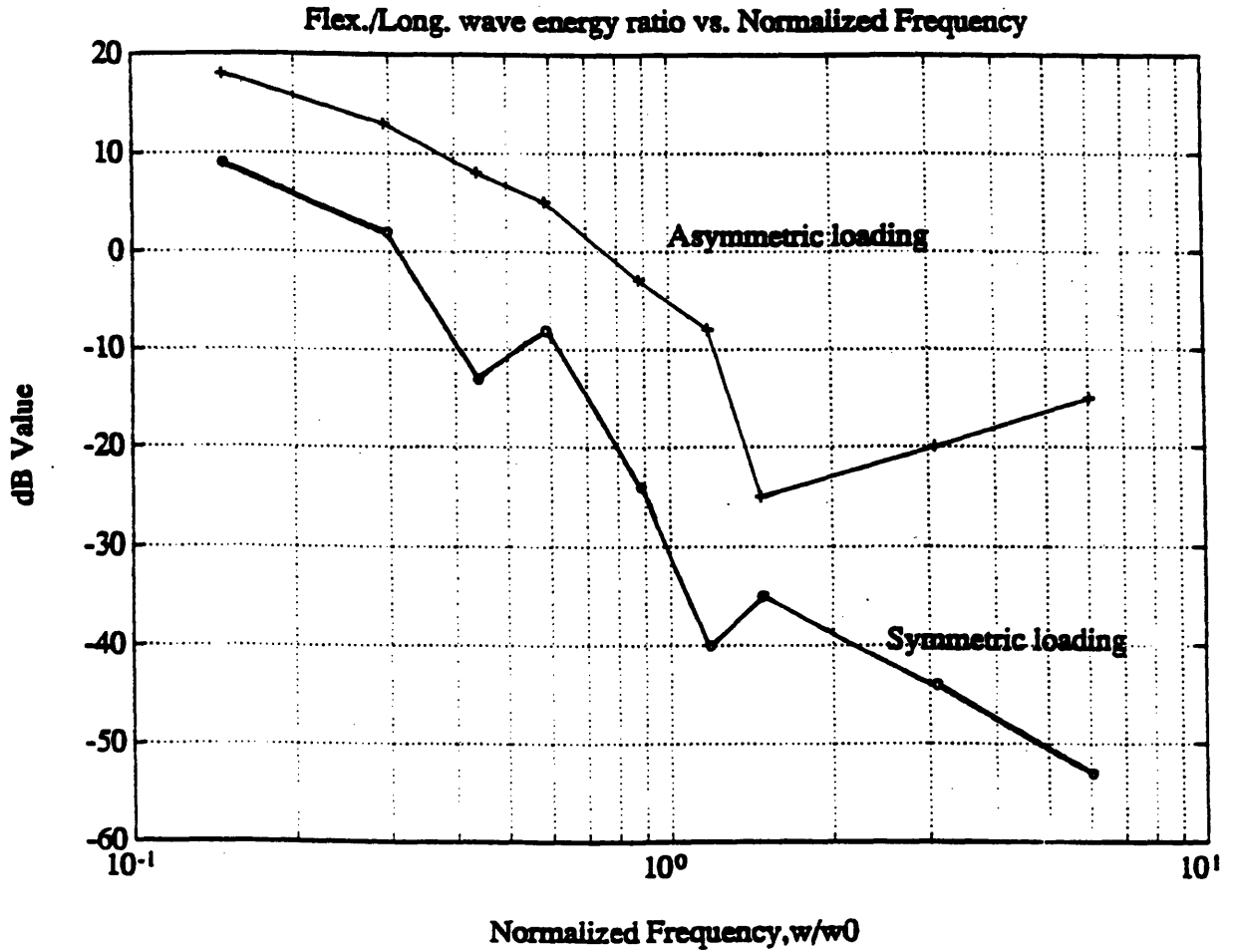
Above resonance frequency, the flexural wave diminishes(-30dB per decade)in the symmetric loading case, while the longitudinal to flexural wave coupling grows (20dB per decade) throughout the investigated frequency span for the asymmetric loading case.



Flex./Long. Energy Ratio

frequency (Hz)	Symmetric loading (dB)	Asymmetric loading (dB)
19.531	9	18
39.063	2	13
58.594	-13	8
78.125	-8	5
117.19	-24	-3
156.25	-40	-8
195.31	-35	-25
410.16	-44	-20
800.78	-53	-15

Table 4-II: Flexural/Longitudinal coupling wave energy ratio



Power spectrum measurements for a series of pure tone longitudinal excitations to the Delrin rod with a dynamic absorber layer attached, where the crosses represent asymmetric loading and circles for symmetric.

Figure 4-2: Longitudinal to flexural coupling wave energy ratio

## Chapter 5

### Conclusions

For zero damping, a stop band exists for the range  $1 < \omega/\omega_0 < (1 + \beta)^{1/2}$ , in which the wavenumber  $\gamma$  is pure imaginary. Realistic treatment of damping is applied and the effects of damping parameters to the longitudinal wave propagation through the dispersion relation is verified from the experiment. The results confirm the analytical model used and that the attached mass system acts as a dynamic absorber.

The three-element combination (Zener model) does stiffen by a small amount as the frequency increases and, by association, is said to possess a transition frequency. This model gives better prediction than the Kelvin model when the loss factor is not too small ( $\eta > 0.2$  in our case).

It is also shown that the interaction between longitudinal and flexural waves may lead to significant rates of transformation of the compressional wave energy into bending, as the coupling is much stronger in the asymmetric loading case than symmetric.

Future work may be suggested to have a continuous isolation layer, with consideration of wave propagation in the isolator layer. Also an investigation of multi-mode wave propagation within one layer would appear worthwhile.

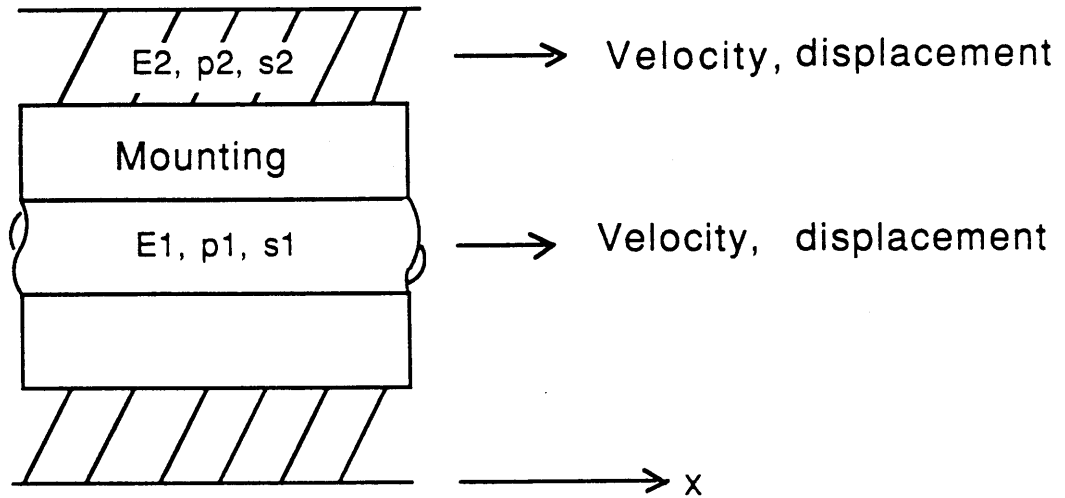


Figure 5-1: With wave propagation in the dynamic absorber layer

In complex structure testing, e.g. fluid loaded cylindrical shell, use of rubber as a mounting material is generally expected. For this, it is important to fully model the viscoelastic behaviour. Experimental investigation of the stiffness ratio N-factor may thus be important.

## References

- [1] Abdulhadi, M.I.  
*Stiffness and Damping Coefficients of Rubber.*  
Ingenieur-Archiv, 55, pp 421-427, 1985.
- [2] Aklonis, J. J. and Macknight, W. J.  
*Introduction to Polymer Viscoelasticity.*  
John Wiley & Sons, New York, 1983.
- [3] Alfrey, T. and Doty P.  
*The Methods of Specifying the Properties of Viscoelastic Materials.*  
*J. Applied Physics*, 16(11):700-713 , , 1945.
- [4] Allen, P. W., Lindley, P. B. and Payne, A. R.  
*Use of Rubber in Engineering.*  
*Maclaren and Sons LTD, London , , 1967.*
- [5] Baer, E.  
*Engineering Design for Plastics.*  
Reinhold Publishing Corp., New York, 1964.
- [6] Bendat, J. S. and Piersol, A. G.  
*Engineering Application of Correlation and Spectra Analysis.*  
Wiley, New York, 1980.
- [7] Bendat, J. S. and Piersol, A. G.  
*Random Data: Analysis & Measurement Procedures.*  
John Wiley & Sons, New York, 1986.
- [8] Brown, R. P.  
*Physical Testing of Rubbers.*  
*Applied Science Publishers LTD, London , , 1979.*
- [9] Cremer, L., Heckl, M. and Ungar, E. E.  
*Structure Borne Sound.*  
Springer-Verlag, New York, New York, 1988.
- [10] Feinberg, M.  
*Vibration-Isolation Systems.*  
*Mach. des.* 37(18):142-149, 1965.
- [11] Freakley, P. K. and Payne, A. R.  
*Theory and Practice of Engineering with Rubber.*  
Applied Science Publishers LTD, London, 1978.
- [12] Fung, Y.C.  
*Foundation of Solid Mechanics.*  
Prentice-Hall, Englewood Cliffs, N.J., 1965.



- [13] Gent, A. N. and Rusch, K. C.  
Viscoelastic Behavior of Open-Cell Forms.  
*Polymer Conf. Series, Wayne State Univ. , May, 1966.*
- [14] Gurnee, E. F.  
Dynamics of Viscoelastic Behavior.  
*Polymer Conf. Series, Wayne State Univ. , May, 1966.*
- [15] Harris, Fredric.  
On the use of Windows for Harmonic Analysis with the discrete Fourier Transform.  
*Proc. IEEE, V. 66, No. 1 , , 1978.*
- [16] Hopkins, I. L.  
Resonance as Observed by Fitzgerald in Relation to characteristics of the Specimen-  
Aparatus System.  
*Polymer Conf. Series, Wayne State Univ. , May, 1966.*
- [17] Junger, M.C. and Feit, D.  
*Sound, Structures and Their Interactions.*  
The MIT Press, Cambridge, MA, 1986.
- [18] Kaul, R.K. and McCoy, J.J.  
*Propagation of Axisymmetric Waves in a Circular Semi-infinite Elastic Rod.*  
JASA, 36, pp.653-660, 1964.
- [19] Kerwin, E. M. Jr. and Ungar E. E.  
*Discussion of paper entitled 'Damping Structural Resonances Using Viscoelastic  
Shear-Damping Mechanisms' by J. E. Ruzicka.*  
Trans. ASME, J. Eng. Ind. 83(4):424, 1961.
- [20] Klyukin, I. I.  
*Influence of the Elastic Dissipation Parameters, Load characteristics, and Degree  
of Lateral Constraint of Vibration-Isolation Elements on Their Damping  
Properties.*  
Soviet Physics Acoustics, 28(1):46-49, 1982.
- [21] Olivieri, L.A.  
The Effect of Dynamic Absorbers on Longitudinal Wave Propagation in A Circular  
Rod.  
*S.M. Thesis, M.I.T. , September, 1989.*
- [22] LePage, K.D.  
The Attenuation of Flexural Waves in Asymmetrically Masses Loaded Beams.  
*S.M. Thesis, M.I.T. , September, 1986.*
- [23] Levitan, E. S.  
*Forced Oscillation of a Spring-Mass System having Combined Coulomb and  
Viscous Damping.*  
JASA, 32(10):1265, 1960.

- [24] Lyon, R. H.  
*Machinery Noise and Diagnostics.*  
Butterworths, Stoneham, MA, 1987.
- [25] McNiven, H.D.  
*Extensional Waves in a Semi-infinite Elastic Rod.*  
JASA, 33, pp.23-27, 1961.
- [26] Meirovitch, L.  
*Elements of Vibration Analysis.*  
McGraw-Hill, Inc., 1975.
- [27] Morse, P.M. and Ingard, K.U.  
*Theoretical Acoustics.*  
Princeton University Press, Princeton, 1986.
- [28] Nishinari, K.  
*Longitudinal Vibration of High-Elastic Gels as a Method for Determining  
Viscoelastic Constants.*  
Jap. J. A. Phy. 15(7):1263-1270, 1976.
- [29] Nolle, A. W.  
*Methods for Measuring Dynamic Mechanical Properties of Rubber-Like Materials.*  
J. App. Physics, 19(8):753-774, 1948.
- [30] Plunkett, R.  
*Mechanical Impedance Methods.*  
The American Society of Mechanical Engineers, 1958.
- [31] Ruzicka, J. E.  
*Forced Vibration in Systems with Elastically Supported Dampers.*  
*S.M. Thesis, M.I.T. , June, 1957.*
- [32] Ruzicka, J. E.  
*Resonance characteristics of Unidirectional Viscous and Coulomb-Damped  
Vibration Isolation Systems.*  
*Trans. ASME, J. Eng. Ind. 89(4):729-740 , , 1967.*
- [33] Ruzicka, J. E.  
*Influence of Damping in Vibration Isolation.*  
*Technical Information Division, Naval Research Lab, Washington, D.C. , , 1971.*
- [34] Senturia, S.D. and Wedlock, B.D.  
*Electronic circuits and Applications.*  
John Wiley & Sons, .
- [35] Seybert, A. F.  
*Estimation of Damping from Response Spectra.*  
J. Sound Vib. 75(2):199-206, 1981.
- [36] Smith, Timothy, L.  
*The Attenuation of Flexural Waves in Mass Loaded Beams.*  
*S.M. Thesis, M.I.T. , May, 1985.*

- [37] Snowdon, J. C.  
*Vibration Isolation: Use and Characterization.*  
Rubber Chem., 53(5):1041-1087, 1980.
- [38] Snowdown, J. C.  
*Vibration and Shock in Damped Mechanical Systems.*  
John Wiley & Sons, Inc., 1968.
- [39] Soroka, W. W.  
Vibration Isolators.  
*Prod. Eng.* 141-145 , July, 1957.
- [40] Sperry, W. C.  
*Rheological-Model Concept.*  
JASA, 36(2):376-385, 1964.
- [41] Steven, Kay and Stanley, Marple.  
Spectrum Analysis - A Modern Perspective.  
*Proc. IEEE*, V.69, No. 11 , , 1981.
- [42] Taylor, P.D:  
Wave Propagation in a Beam Having Double Resonant Loading.  
*S.M. Thesis, M.I.T.* , August, 1987.
- [43] Tse, F. S., Morse, I. E., and Hinkle, R. T.  
*Mechanical Vibrations : Theory and Applications.*  
Allyn and Bacon, Boston, 1978.
- [44] Tse, F. S. and Morse, I. E.  
*Measurement and Instrumentation in Engineering.*  
Marcek Dekker, New York, 1989.
- [45] Ungar, E. E. and Kerwin, E. M. Jr.  
*Loss Factors of Viscoelastic Systems in Terms of Energy Concepts.*  
JASA, 34(7):954, 1962.
- [46] Welch, P. D.  
The Use of FFT for the Estimation of Power Spectra.  
*IEEE Trans.Audio & Electroacoust*, V.AU-15, No.2 , June, 1967.
- [47] William, H. Press, etc.  
*Numerical Recipes. & Example Book (Fortran).*  
Cambridge Univ. Press, 1989.

## Appendix A: Computer Program for Wavenumber Analysis

```
for k=1:250;
t1(k)=(2*k+1)/50.0;
r1(k,1)=1+beta/(1-(t1(k)*t1(k))/(1+i*ata*t1(k)*N/(i*ata*t1(k)-N)));
r(k,1)=sqrt(r1(k,1));
att(k,1)=54.6*imag(r(k,1));
c(k,1)=1161/(real(r(k,1)));
end;

for k=1:250;
t1(k)=(2*k+1)/50.0;
r1(k,2)=1+beta/(1-(t1(k)*t1(k))/(1+i*ata*t1(k)*N/(i*ata*t1(k)-N)));
r(k,2)=sqrt(r1(k,2));
att(k,2)=54.6*imag(r(k,2));
c(k,2)=1161/(real(r(k,2)));
end;

for k=1:250;
t1(k)=(2*k+1)/50.0;
r1(k,3)=1+beta/(1-(t1(k)*t1(k))/(1+i*ata*t1(k)*N/(i*ata*t1(k)-N)));
r(k,3)=sqrt(r1(k,3));
att(k,3)=54.6*imag(r(k,3));
c(k,3)=1161/(real(r(k,3)));
end;
text(2.2,2900,'N=0.1,eta=0.204,beta=3.23')
>> axis([-1,1,0,3000])
>> semilogx(t1,c)
>> grid
>> axis([-1,1,2,4])
>> loglog(o,c)
>> title('Phase Speed vs. Normalized Frequency')
>> xlabel('Normalized Frequency,w/w0')
text(2,1500,'Non-relaxation')
>> text(2.2,2500,'Relaxation')

>> ylabel('Phase speed (m/s)')
text(1,40,'eta=0.204, beta=3.23')
text(.3,0,'K1=.6 K2,eta=0.204,beta=3.23')
text(2.2,2900,'N=0.1')
text(.2,50,'Relaxation with N-factor,eta=0.204,beta=3.23')
>> print('oe -h')
text(.7,1800,'Non-relaxation')
text(.3,2500,'Relaxation with N=1')
text(1,40,'Loss factor 0.284, Mass ratio 3.23')
text(.7,2800,'Relaxation with N=.3')
text(.7,2200,'Relaxation with N=1.5')

semilogx(t1,c)
semilogx(t1,att)
axis([-1,1,2,4])
axis([-1,1,0,3000])
axis([-1,1,0,200])
```

```
text(.12,20, 'Relaxation with N-factor,eta=0.2 N=1')
>> clg
>> semilogx(t1,att)
>> title('Attenuation vs. Normalized Frequency')
>> xlabel('Normalized Frequency,w/w0')
>> ylabel('Attenuation (dB per wave length)')
>> text(.12,20, 'Relaxation with Mass-factor,eta=0.2 N=1')
>> text(1.2,150,'Beta=3')

>> title('Attenuation vs. Normalized Frequency')
>> xlabel('Normalized Frequency,w/w0')
>> ylabel('Attenuation (dB per wave length)')
>> grid
>> text(1.2,190,'eta=0.1,beta=3')
>> text(1.2,100,'eta=0.3,beta=3')
>> text(1.2,40,'eta=1.0,beta=3')
>> text(.1,20,'Non-relaxation')

>> axis([-1,1,0,200])
axis([-1,1,0,3000])

for k=1:250;
t1(k)=(2*k+1)/50.0;
r1(k,1)=1+beta/(1-t1(k)*t1(k)/(1-i*ata*t1(k)));
r(k,1)=sqrt(r1(k,1));
c(k,1)=1161/(real(r(k,1)));
att(k,1)=54.6*imag(r(k,1));
end;

for k=1:250;
t1(k)=(2*k+1)/50.0;
r1(k,2)=1+beta/(1-t1(k)*t1(k)/(1-i*ata*t1(k)));
r(k,2)=sqrt(r1(k,2));
c(k,2)=1161/(real(r(k,2)));
att(k,2)=54.6*imag(r(k,2));
end;

for k=1:250;
t1(k)=(2*k+1)/50.0;
r1(k,3)=1+beta/(1-t1(k)*t1(k)/(1-i*ata*t1(k)));
r(k,3)=sqrt(r1(k,3));
c(k,3)=1161/(real(r(k,3)));
att(k,3)=54.6*imag(r(k,3));
end;
```

### Appendix B: Drive Point Impedance Diagram

Measurement freq. span	$f_o$ (Hz)	$f_{3dB\ low}$ (Hz)	$f_{3dB\ high}$ (Hz)	$\eta$
800	135	111	157	.341
400	134.5	109.5	156.5	.349
200	134.75	107.75	155.25	.353
Hz	$\bar{f}_o = 134.75$		$\bar{\eta} = .348$	



Brüel & Kjær

Type 2032

Page No.  
43

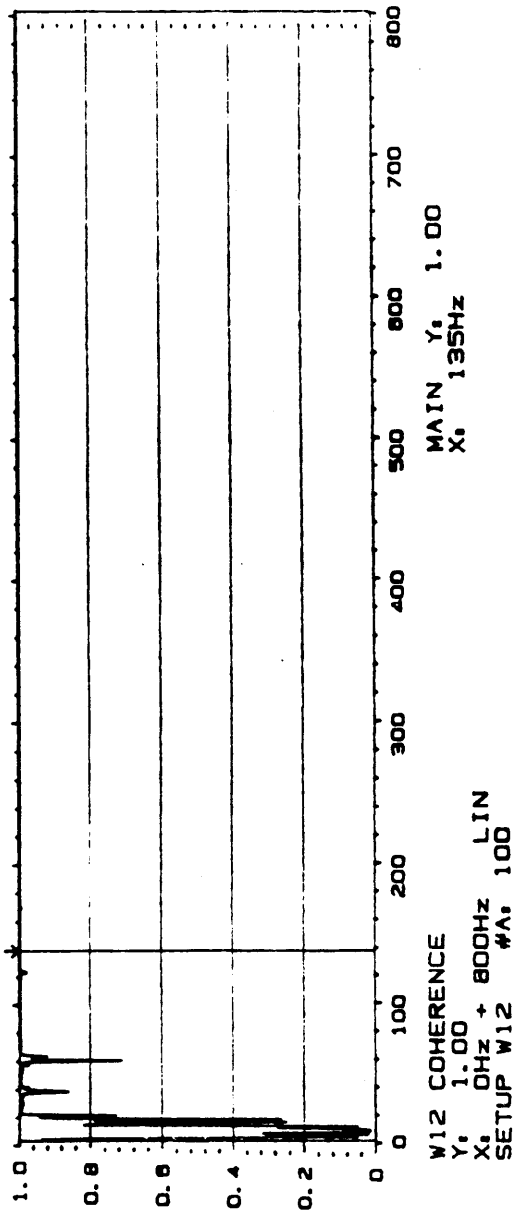
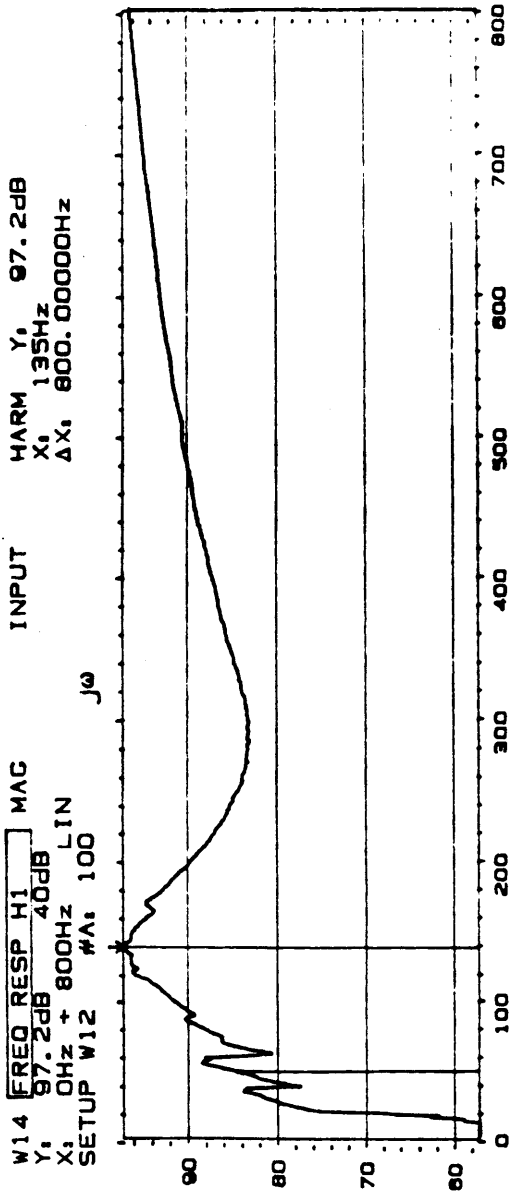
Sign.:

Meas.  
Object:

\_\_\_\_\_  
\_\_\_\_\_  
\_\_\_\_\_  
\_\_\_\_\_

Comments:

\_\_\_\_\_  
\_\_\_\_\_  
\_\_\_\_\_  
\_\_\_\_\_



Resonant frequency and loss factor measurement for a short rod with a single isolator located very closely to the drive point (frequency span 800Hz).



Brüel & Kjær

Type 2032

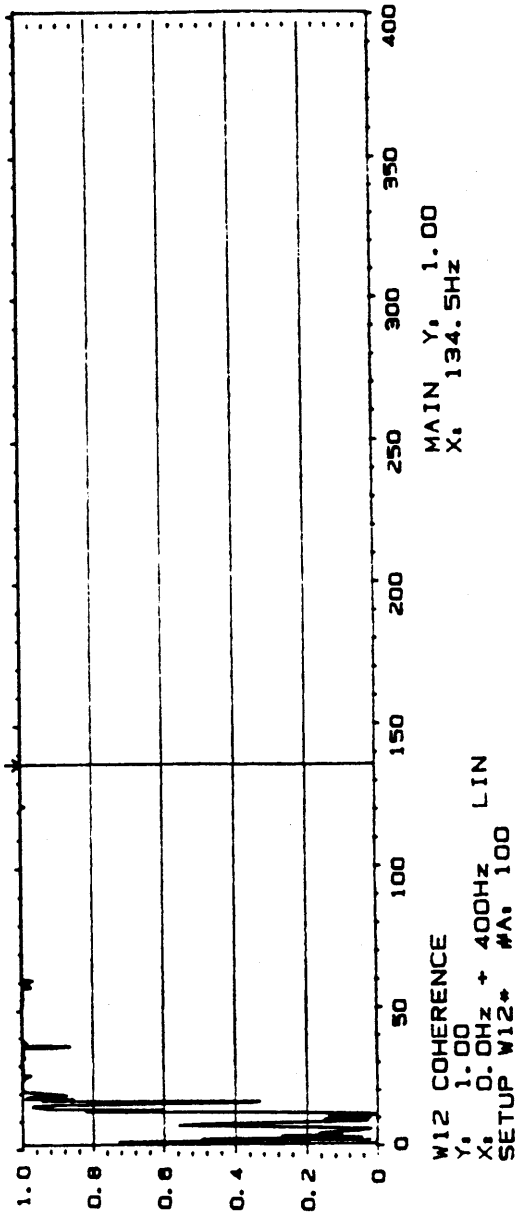
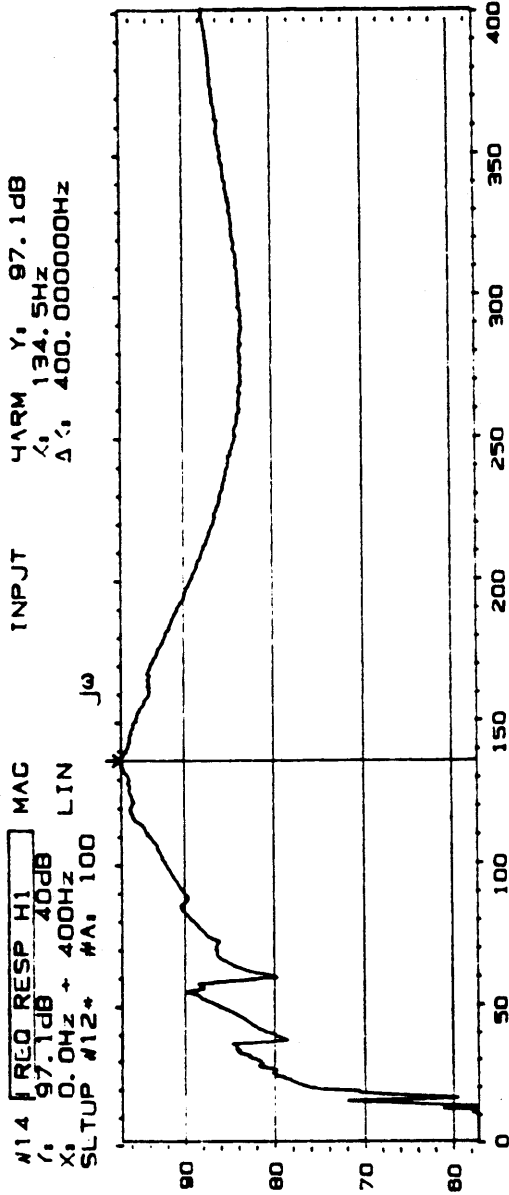
Page No.  
44

Sign.:

Meas.

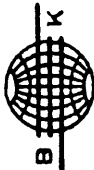
Object:

Comments:



Resonant frequency and loss factor measurement for a short rod with a single isolator located very closely to the drive point (frequency span 400Hz).





Brüel & Kjær

Type 2032

Page No.  
42

Sign.:

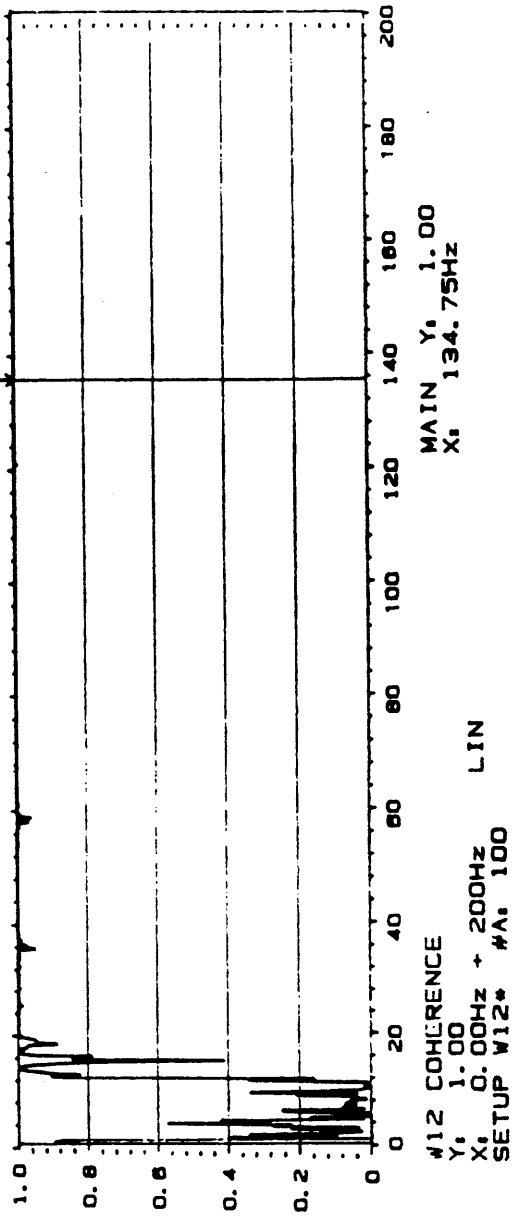
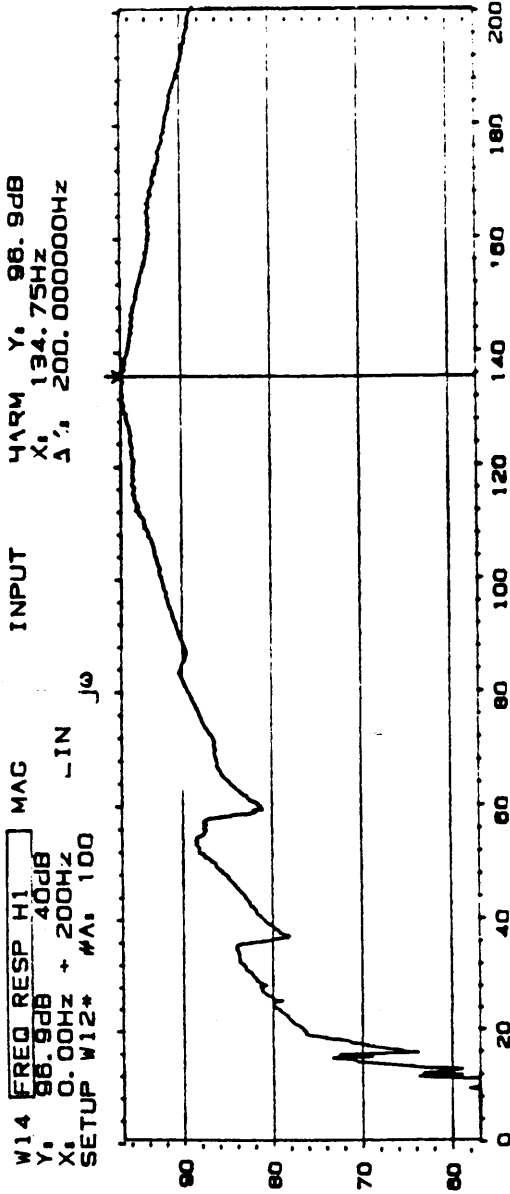
Meas.

Object:

\_\_\_\_\_  
\_\_\_\_\_  
\_\_\_\_\_  
\_\_\_\_\_

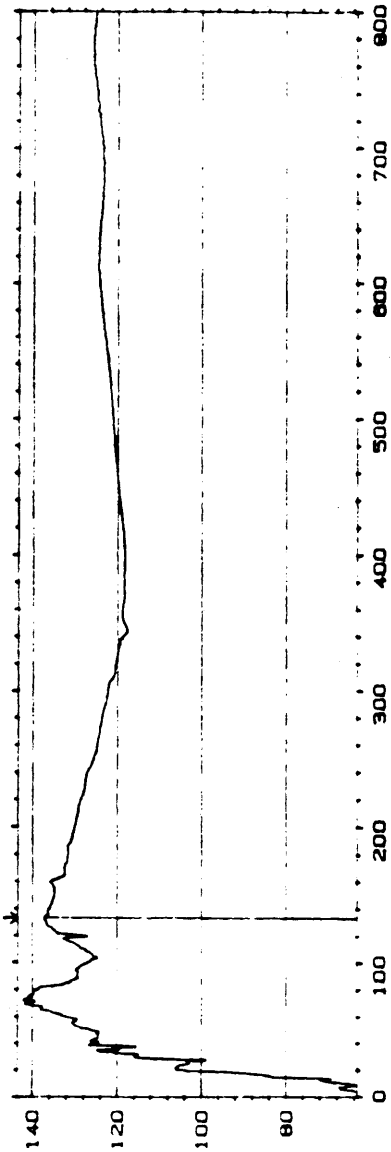
Comments:

\_\_\_\_\_  
\_\_\_\_\_  
\_\_\_\_\_  
\_\_\_\_\_



Resonant frequency and loss factor measurement for a short rod with a single isolator located very closely to the drive point (frequency span 200Hz).

W12 FREQ RESP HI MAG  
 Y1 143.5dB 80dB  
 X1 0Hz + 800Hz LIN  
 SETUP W12 #A: 100



Brüel & Kjær

Type 2032

Page No.  
27

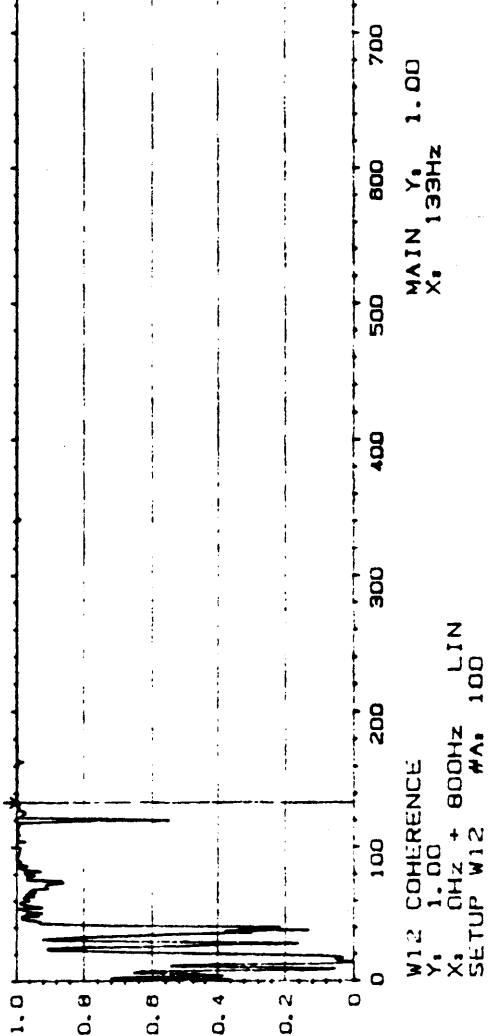
Sign.

Meas.  
Object:

\_\_\_\_\_  
 \_\_\_\_\_  
 \_\_\_\_\_  
 \_\_\_\_\_

Comments:

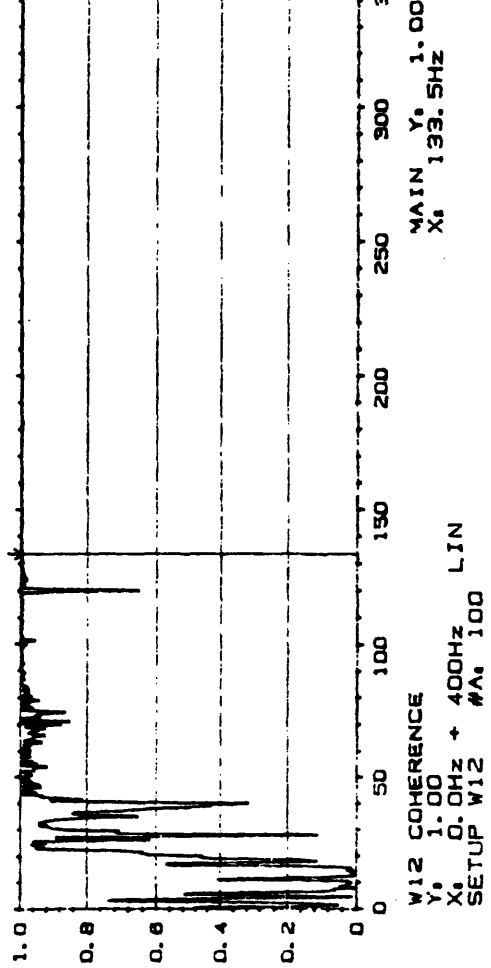
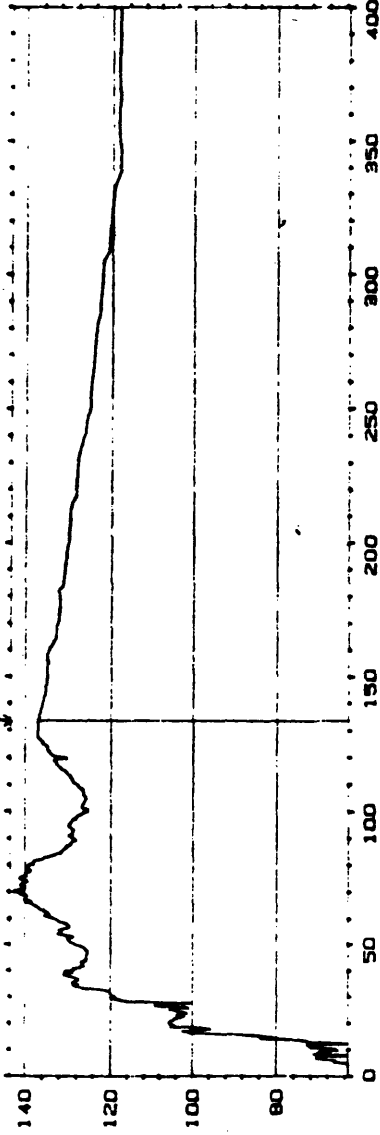
\_\_\_\_\_  
 \_\_\_\_\_  
 \_\_\_\_\_  
 \_\_\_\_\_



W12 COHERENCE  
 Y1 1.00  
 X1 0Hz + 800Hz LIN  
 SETUP W12 #A: 100

MAIN Y: 1.00  
 X: 133Hz

W12 FREQ RESP HI MAG INPUT MAIN Y: 137.3dB  
 Y: 143.5dB 80dB X: 133.5Hz  
 X: 0.0Hz + 400Hz LIN #A: 100  
 SETUP W12 #A: 100 J0



B K  
 Brual & Kjaer

Type 2032

Page No. 26

Sign.:

Meas. Object:

Comments:



Brüel & Kjær

Type 2032

Page No.  
25

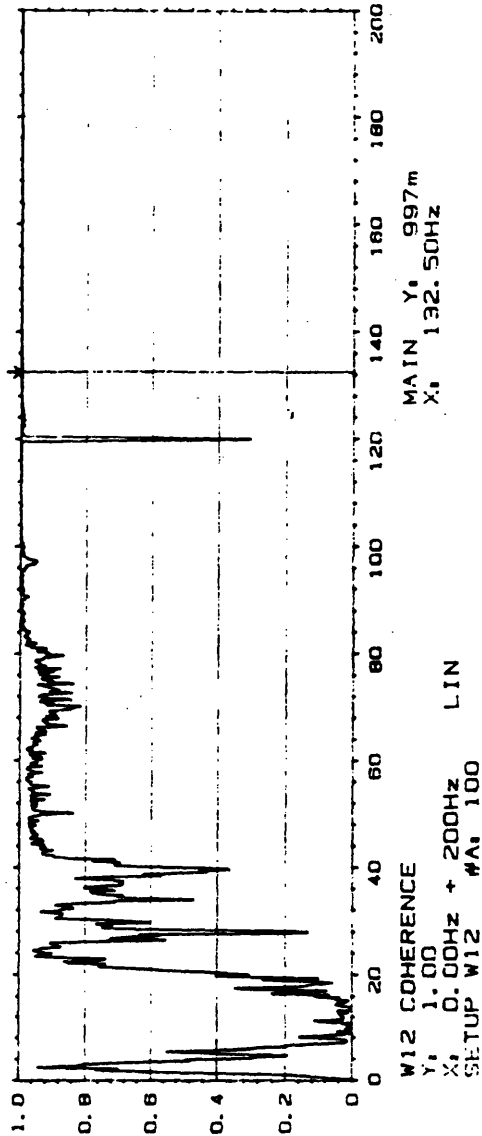
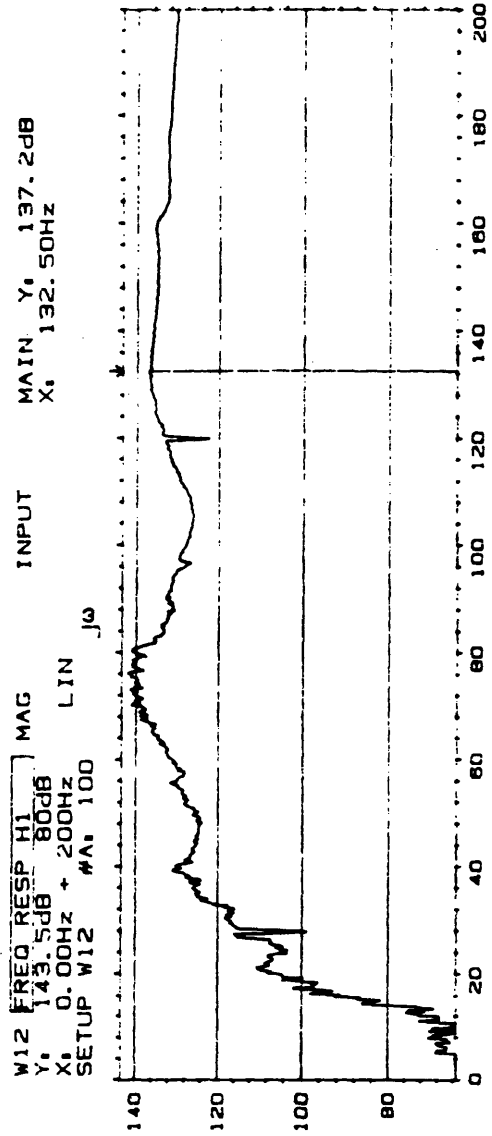
Sign.:

Meas.  
Object:

\_\_\_\_\_  
\_\_\_\_\_  
\_\_\_\_\_  
\_\_\_\_\_

Comments:

\_\_\_\_\_  
\_\_\_\_\_  
\_\_\_\_\_  
\_\_\_\_\_



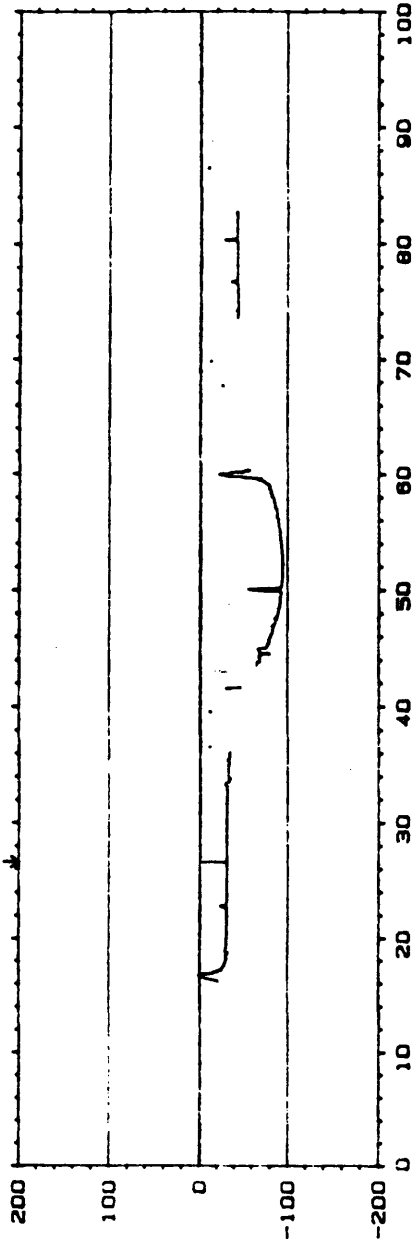
### Appendix C: Cross Spectrum Data

#### Cross spectrum data

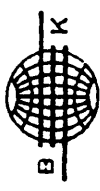
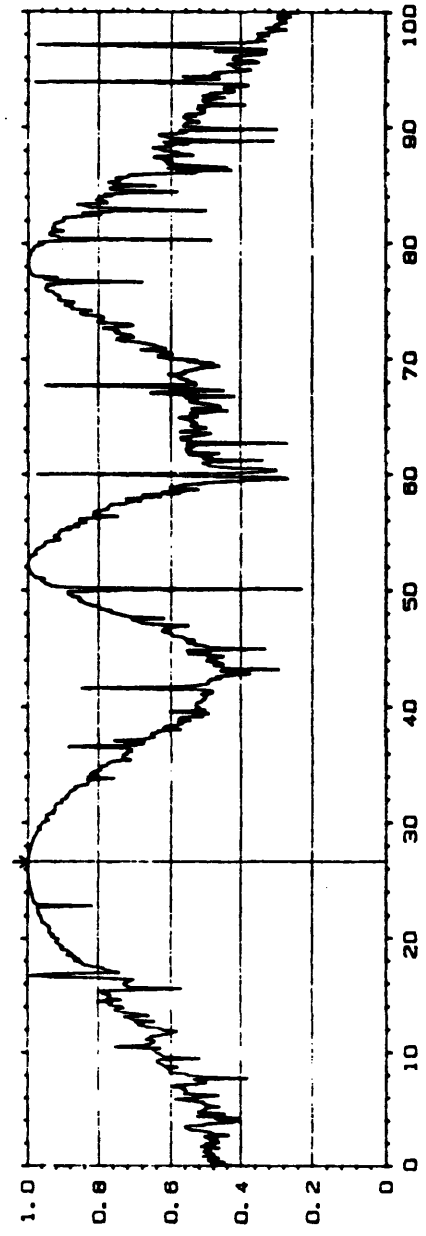
$\beta = 3.23$ ,  $\eta = 0.348$ ,  $f_o = 134.75$  Hz

$f/f_o$	$f$ (Hz)	phase delay (degree/120.0cm)	$\lambda$ (m)	phase speed (m/s)
0.20	26.625	31.0	13.94	371.0
0.31	41.687	34.4	12.56	523.5
0.56	74.00	91.2	4.737	350.5
0.63	84.00	79.0	5.468	459.3
0.70	93.00	79.4	5.441	506.0
0.73	97.00	88.4	4.887	474.0
0.77	103.00	100.5	4.299	442.7
0.84	112.00	104.5	4.134	463.0
0.99	132.00	107.8	4.007	529.0
1.27	168.25	77.1	5.603	942.7
1.41	187.25	67.9	6.362	1191
1.73	229.5	53.4	8.090	1857
1.80	239.0	50.9	8.487	2028
1.92	256.0	59.7	7.236	1852
2.68	356.0	101.2	4.269	1520
3.43	456.0	145.0	2.979	1359
4.24	564.0	180.0	2.400	1354
4.80	638.0	255.9	1.688	1077
5.66	753.0	279.3	1.547	1165

W22 CROSS SPEC PHASE INPUT MAIN Y, -31.0DEG  
 Y, -200 TO +200 DEG X, 26.625Hz  
 X, 0.000Hz + 100Hz LIN  
 SETUP W22 #A, 100



W20 COHERENCE MAIN Y, 1.00  
 Y, 1.00 X, 26.625Hz  
 X, 0.000Hz + 100Hz LIN  
 SETUP W22 #A, 100



Brüel & Kjær

Type 2032

Page No.  
83

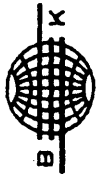
Sign.:

Meas.  
Object:

\_\_\_\_\_  
 \_\_\_\_\_  
 \_\_\_\_\_  
 \_\_\_\_\_

Comments:

\_\_\_\_\_  
 \_\_\_\_\_  
 \_\_\_\_\_  
 \_\_\_\_\_



Brüel & Kjær

Type 2032

Page No.  
80

Sign.:

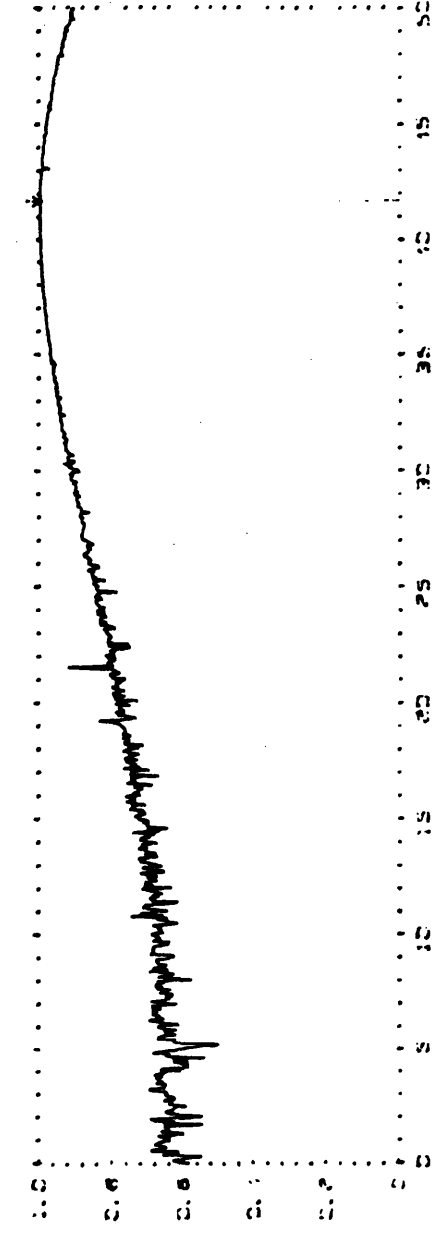
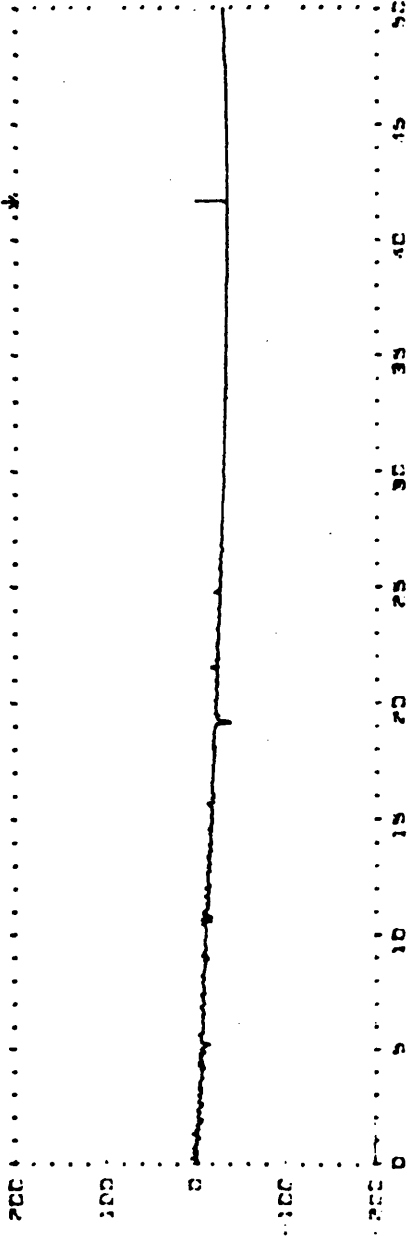
Meas.  
Object:

\_\_\_\_\_  
\_\_\_\_\_  
\_\_\_\_\_  
\_\_\_\_\_

Comments:

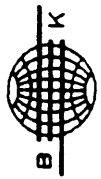
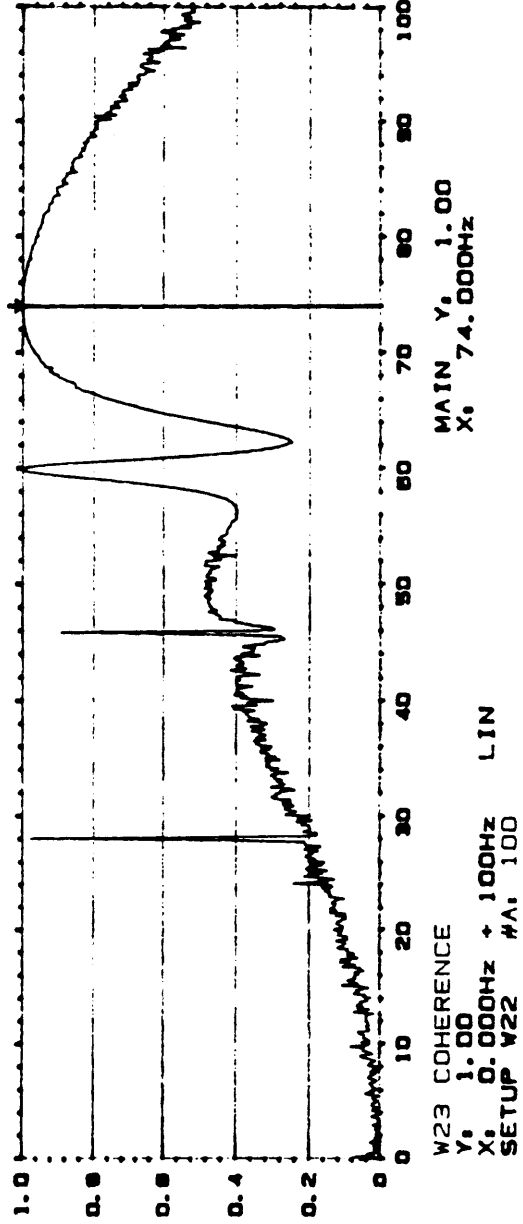
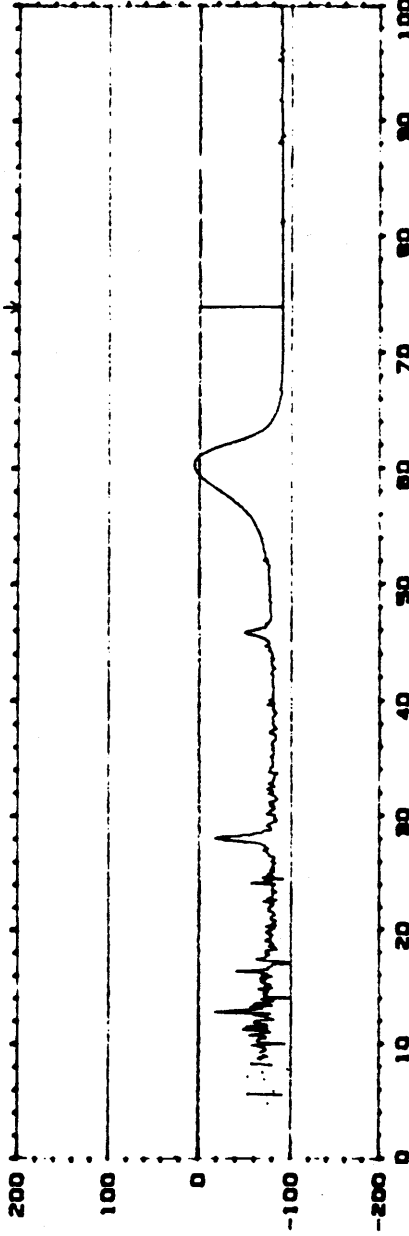
\_\_\_\_\_  
\_\_\_\_\_  
\_\_\_\_\_  
\_\_\_\_\_

W22 CROSS SPEC PHASE INPUT MAIN Y<sub>1</sub> -34.4DEG  
X<sub>1</sub> 41.687Hz  
Y<sub>1</sub> 2.000000  
X<sub>1</sub> 2.000000  
SETUP #23 #A<sub>1</sub> 100



W20 COHERENCE  
Y<sub>1</sub> 2.000000  
X<sub>1</sub> 2.000000  
SETUP #23 #A<sub>1</sub> 100

W22 CROSS SPEC PHASE INPUT MAIN Y, -91.2DEG  
 Y, -200 TO +200 DEG X, 74.000Hz  
 X, 0.000Hz + 100Hz LIN  
 SETUP W22 #A: 100



Brüel & Kjær

Type 2032

Page No.  
39

Sign.:

Meas.  
Object:

\_\_\_\_\_  
 \_\_\_\_\_  
 \_\_\_\_\_  
 \_\_\_\_\_

Comments:

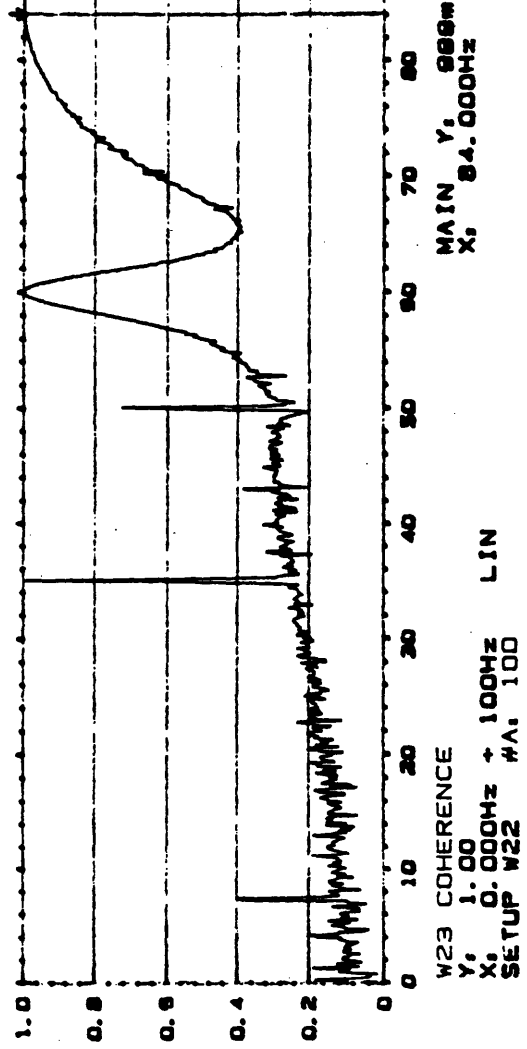
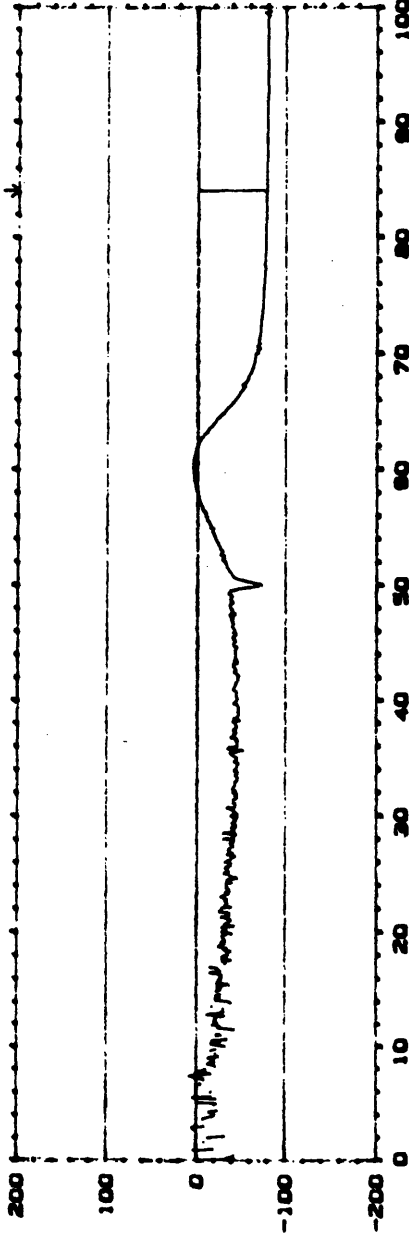
\_\_\_\_\_  
 \_\_\_\_\_  
 \_\_\_\_\_  
 \_\_\_\_\_

MAIN Y, 1.00  
 X, 74.000Hz

W23 COHERENCE  
 Y, 1.00  
 X, 0.000Hz + 100Hz LIN  
 SETUP W22 #A: 100



W22 CROSS SPEC PHASE INPUT MAIN Y, -79.0DEG  
 Y, -200 TO +200 DEG X, 84.000Hz  
 X, 0.000Hz + 100Hz LIN  
 SETUP W22 #A, 100



Brüel & Kjær

Type 2032

Page No.  
42

Sign.:

Meas.  
Object:

---



---



---



---

Comments:

---



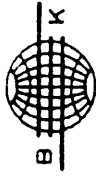
---



---



---



Brüel & Kjær

Type 2032

Page No.  
48

Sign.:

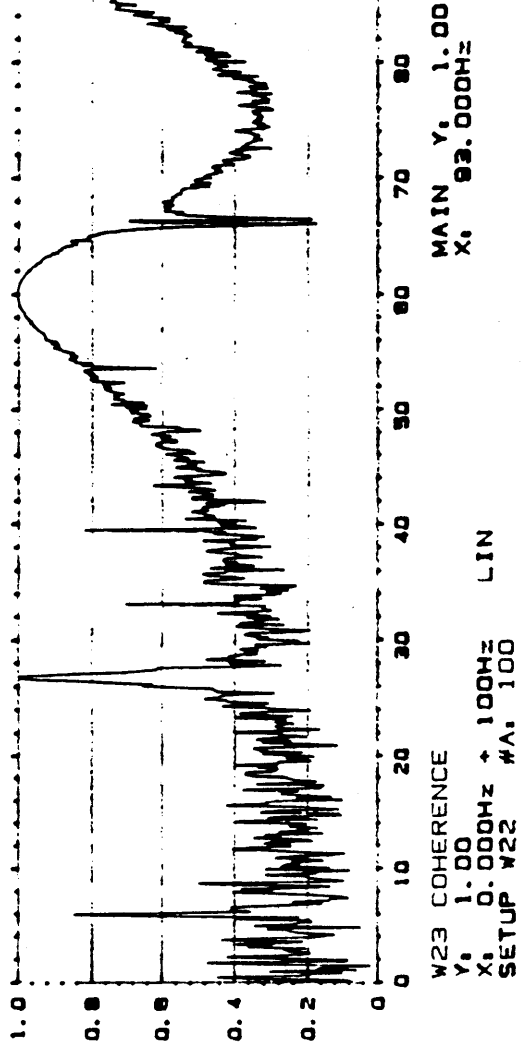
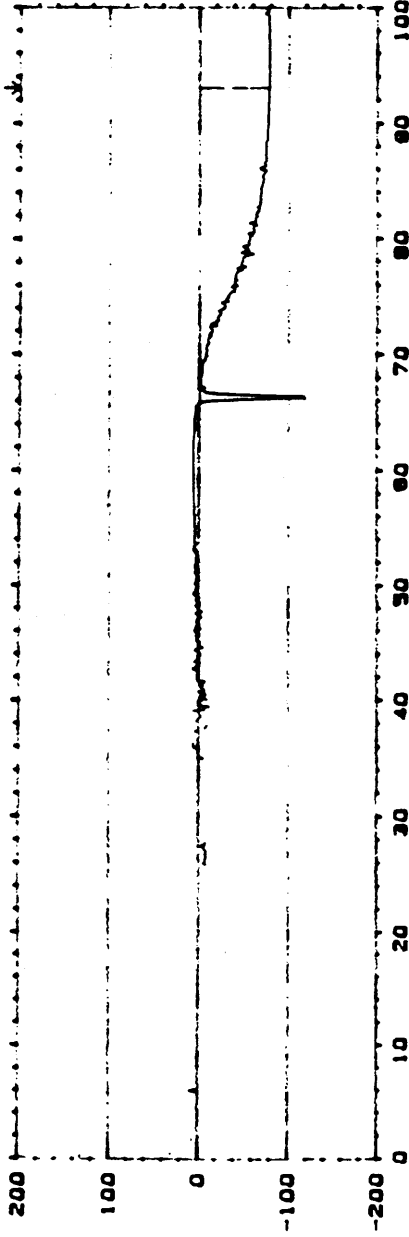
Meas.  
Object:

\_\_\_\_\_  
\_\_\_\_\_  
\_\_\_\_\_  
\_\_\_\_\_  
\_\_\_\_\_

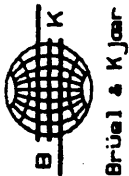
Comments:

\_\_\_\_\_  
\_\_\_\_\_  
\_\_\_\_\_  
\_\_\_\_\_

W22 CROSS SPEC PHASE INPUT MAIN Y: -79.4DEG  
Y: -200 TO +200 DEG X: 93.000Hz  
X: 0.000Hz + 100Hz LIN  
SETUP W22 #A: 100



W22 CROSS SPEC PHASE  
 Y<sub>0</sub> -200 YD +200 DEG  
 X<sub>0</sub> 0.00HZ + 200HZ LIN  
 SETUP W22 #A, 100



Type 2032

Page No. 44

Sign.:

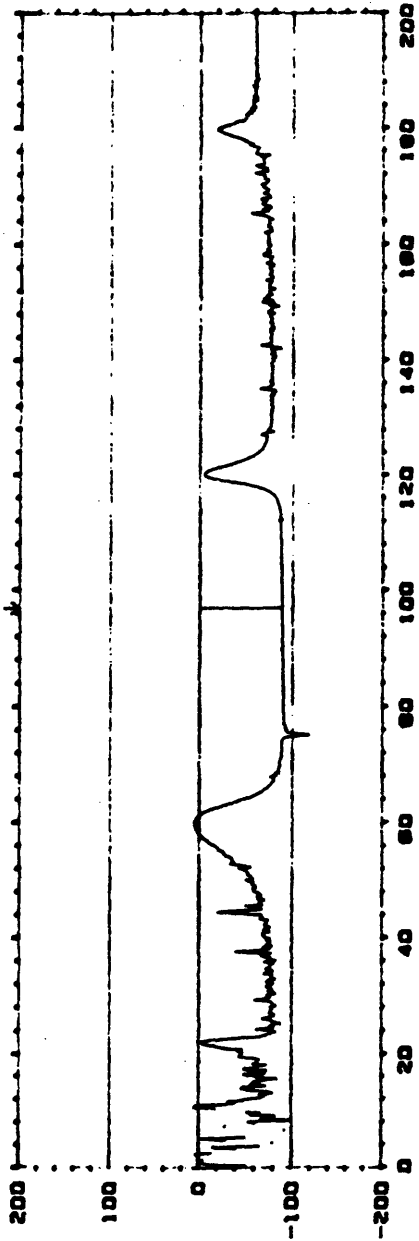
Meas. Object:

\_\_\_\_\_  
 \_\_\_\_\_  
 \_\_\_\_\_  
 \_\_\_\_\_

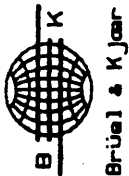
Comments:

\_\_\_\_\_  
 \_\_\_\_\_  
 \_\_\_\_\_  
 \_\_\_\_\_

INPUT  
 MAIN Y<sub>0</sub> -88.4 DEG  
 X<sub>0</sub> 97.00HZ



W23 COHERENCE  
 Y<sub>0</sub> 1.00  
 X<sub>0</sub> 0.00HZ + 200HZ LIN  
 SETUP W22 #A, 100



Type 2032

Page No. 44

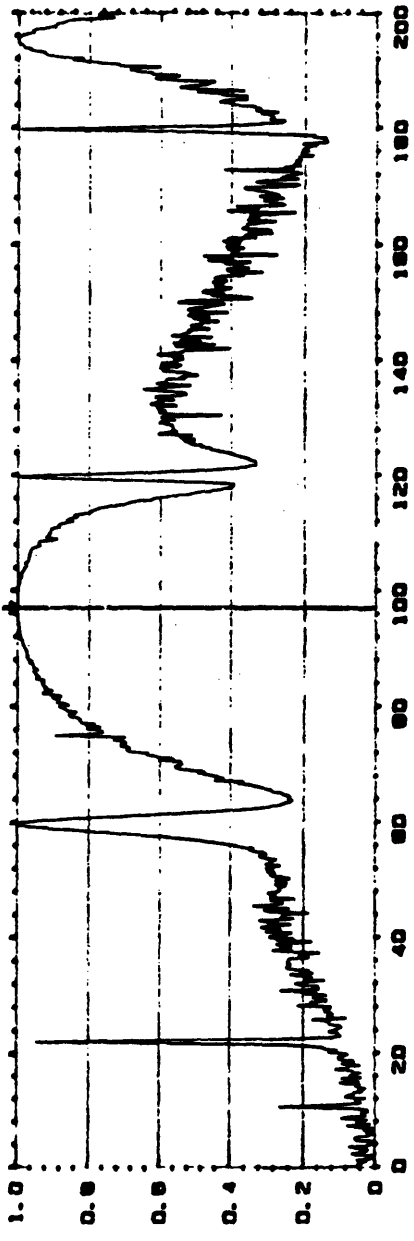
Sign.:

Meas. Object:

\_\_\_\_\_  
 \_\_\_\_\_  
 \_\_\_\_\_  
 \_\_\_\_\_

Comments:

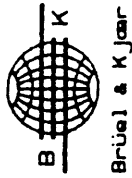
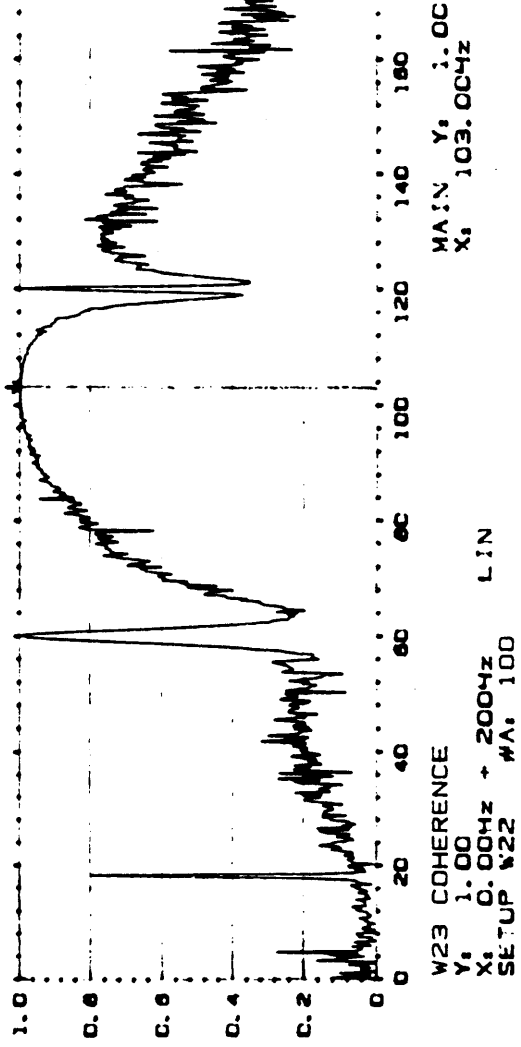
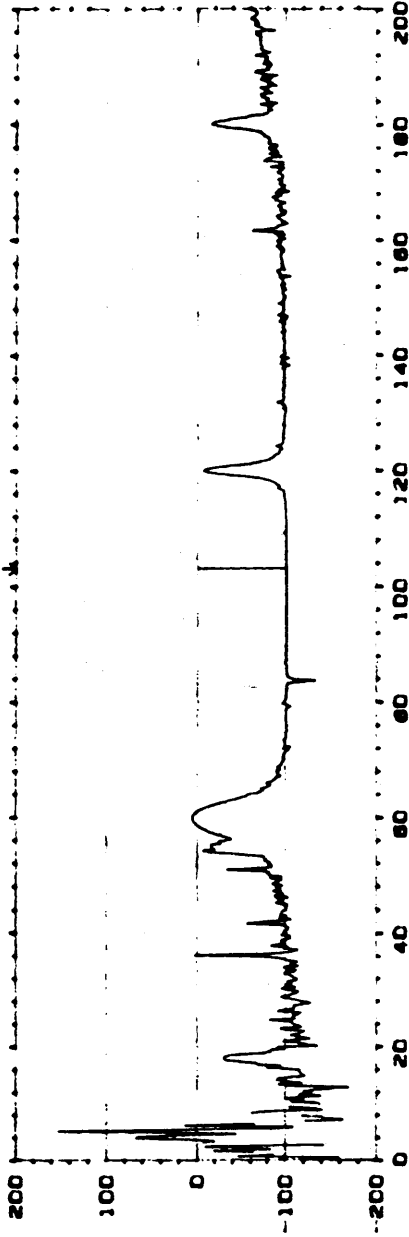
\_\_\_\_\_  
 \_\_\_\_\_  
 \_\_\_\_\_  
 \_\_\_\_\_



MAIN Y<sub>0</sub> 1.00  
 X<sub>0</sub> 97.00HZ

W23 COHERENCE  
 Y<sub>0</sub> 1.00  
 X<sub>0</sub> 0.00HZ + 200HZ LIN  
 SETUP W22 #A, 100

W22 CROSS SPEC PHASE INPUT MAIN Y: -100.5DEG  
 Y: -200 TO +200 DEG X: 103.00Hz  
 X: 0.00Hz + 200Hz LIN  
 SETUP W22 #A: 100



Type 2032

Page No. 55

Sign.:

Meas. Object:

---

---

---

---

---

Comments:

---

---

---

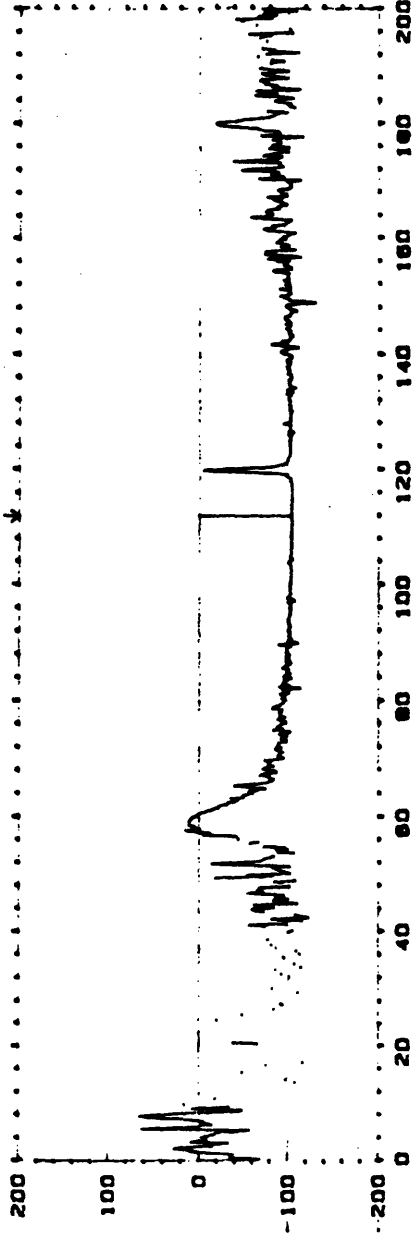
---

---

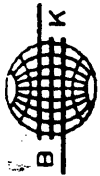
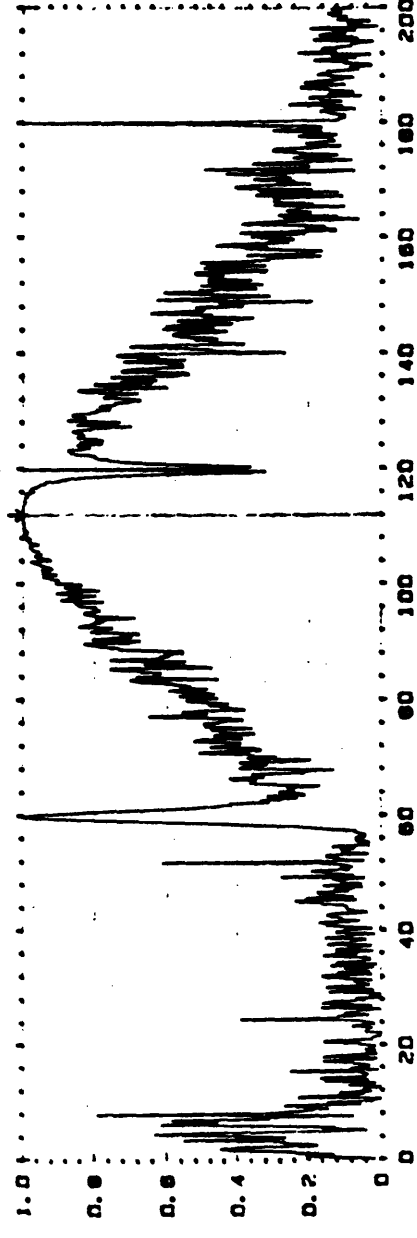
W23 COHERENCE  
 Y: 1.00  
 X: 0.00Hz + 200Hz LIN  
 SETUP W22 #A: 100

MAIN Y: 1.00  
 X: 103.00Hz

W22 CROSS SPEC PHASE INPUT MAIN Y: -104.5DEG  
 Y: 200 TO +200 DEG X: 112.00HZ  
 X: 0.00HZ + 200HZ L.IN  
 SETUP W22 #A: 100



W23 COHERENCE MAIN Y: 1.00  
 Y: 1.00 X: 112.00HZ  
 X: 0.00HZ + 200HZ L.IN  
 SETUP W22 #A: 100



Brüel & Kjær

Type 2032

Page No.  
58

Sign.:

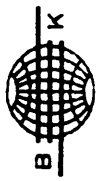
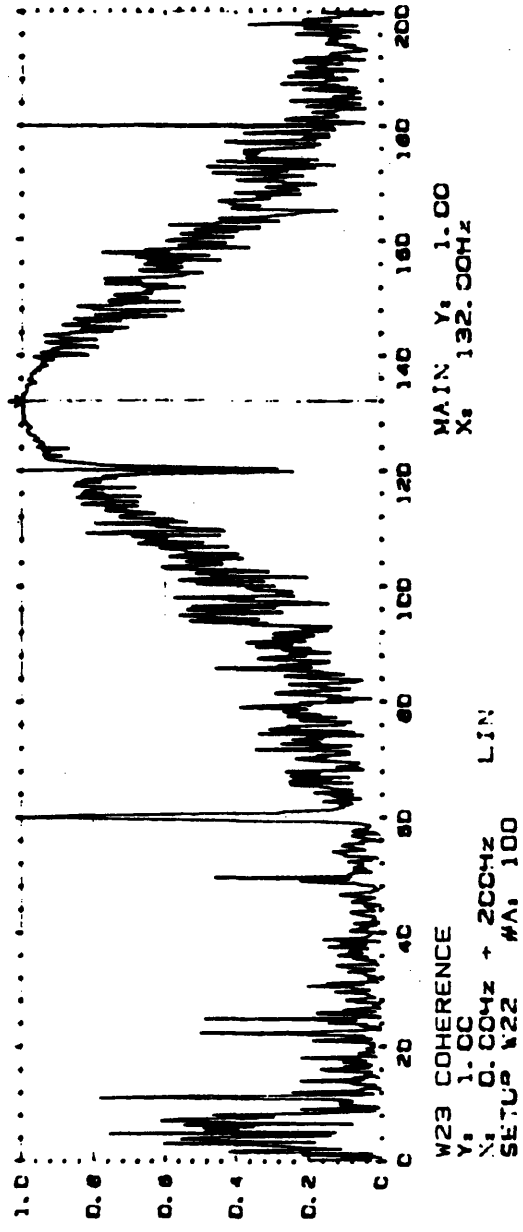
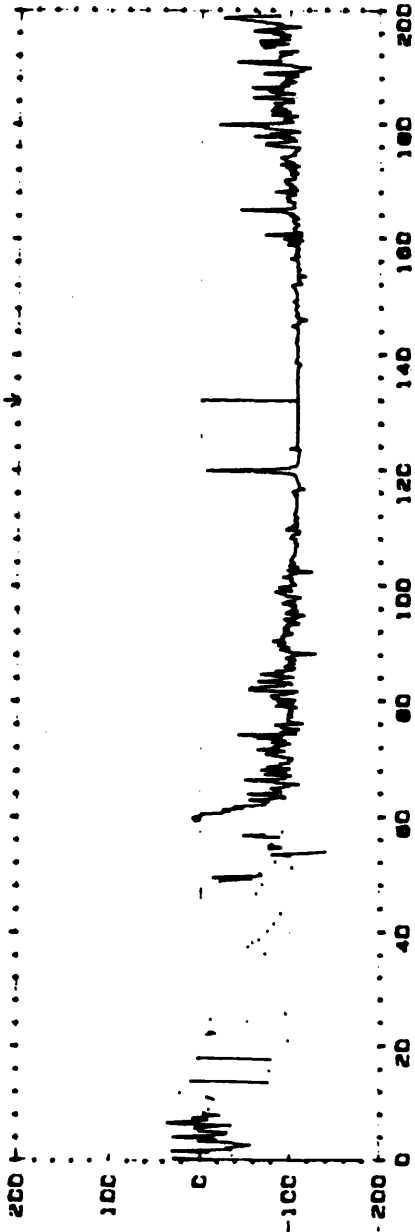
Meas.  
Object:

\_\_\_\_\_  
 \_\_\_\_\_  
 \_\_\_\_\_  
 \_\_\_\_\_

Comments:

\_\_\_\_\_  
 \_\_\_\_\_  
 \_\_\_\_\_  
 \_\_\_\_\_

W22 CROSS SPEC PHASE INPUT MAIN Y: -107.6DEG  
 Y: -200 TO +200 DEC X: 132.00HZ  
 X: 0.00HZ + 200HZ LIN  
 SETUP W22 #A: 100



Brüel & Kjær

Type 2032

Page No.  
59

Sign.:

Meas.  
Object:

\_\_\_\_\_

\_\_\_\_\_

\_\_\_\_\_

\_\_\_\_\_

Comments:

\_\_\_\_\_

\_\_\_\_\_

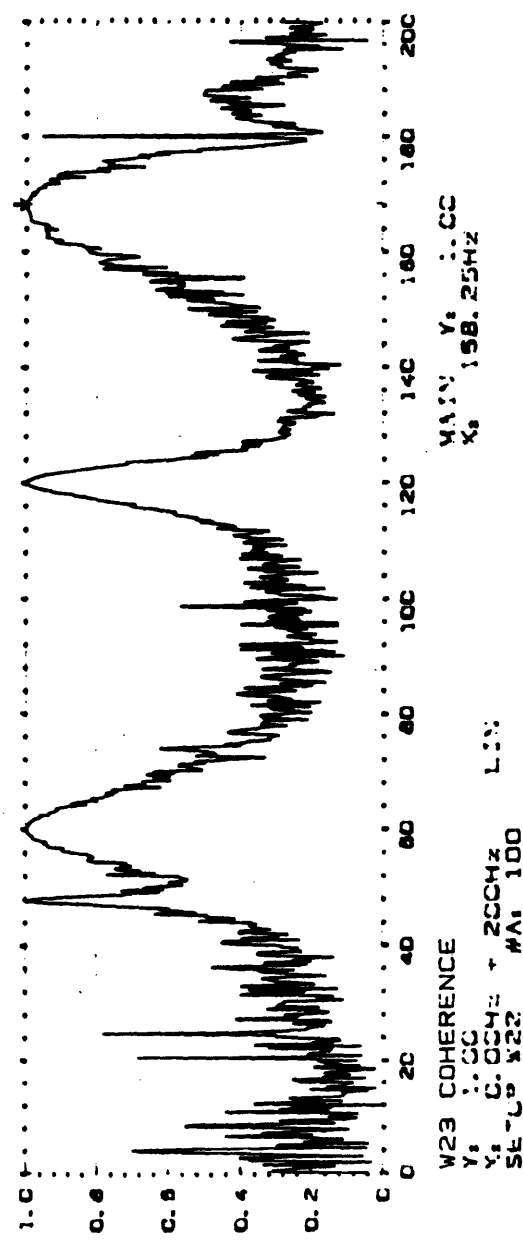
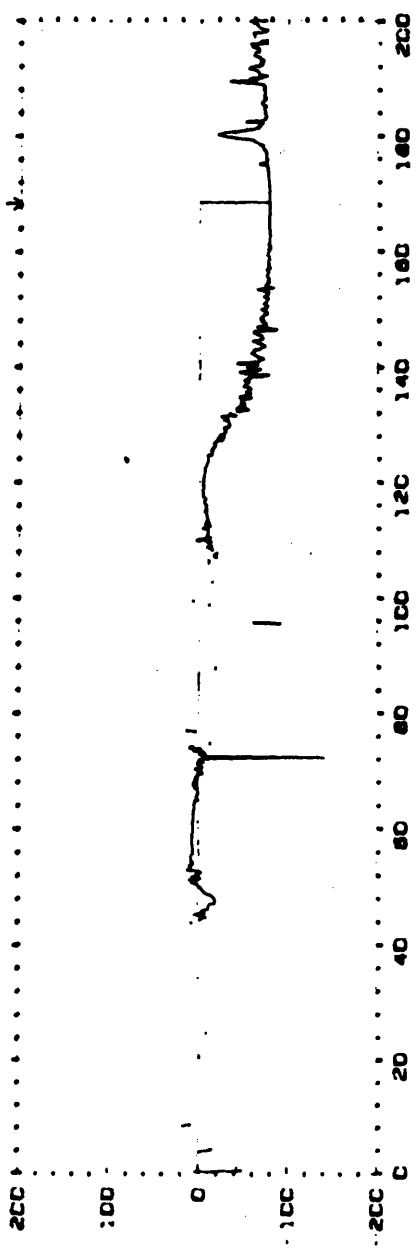
\_\_\_\_\_

\_\_\_\_\_

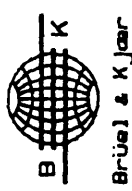
W23 COHERENCE  
 Y: 1.00  
 X: 0.00HZ + 200HZ LIN  
 SETUP W22 #A: 100

MAIN Y: 1.00  
 X: 132.00HZ

W22 CROSS SPEC PHASE INPUT MAIN Y: -77.1 DEG  
 X: 168.25HZ  
 Y: -200 G + 200 DEG  
 X: 0.004z + 200Hz LIN  
 SETUP W22 #A: 100



W23 COHERENCE  
 Y: 1.00  
 X: 0.004z + 200Hz LIN  
 SETUP W22 #A: 100  
 MAIN Y: 1.00  
 X: 158.25HZ



Brüel & Kjær

Type 2032

Page No.  
64

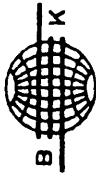
Sign.:

Meas.  
Object:

\_\_\_\_\_  
 \_\_\_\_\_  
 \_\_\_\_\_  
 \_\_\_\_\_

Comments:

\_\_\_\_\_  
 \_\_\_\_\_  
 \_\_\_\_\_  
 \_\_\_\_\_



Brüel & Kjær

Type 2032

Page No.  
61

Sign.:

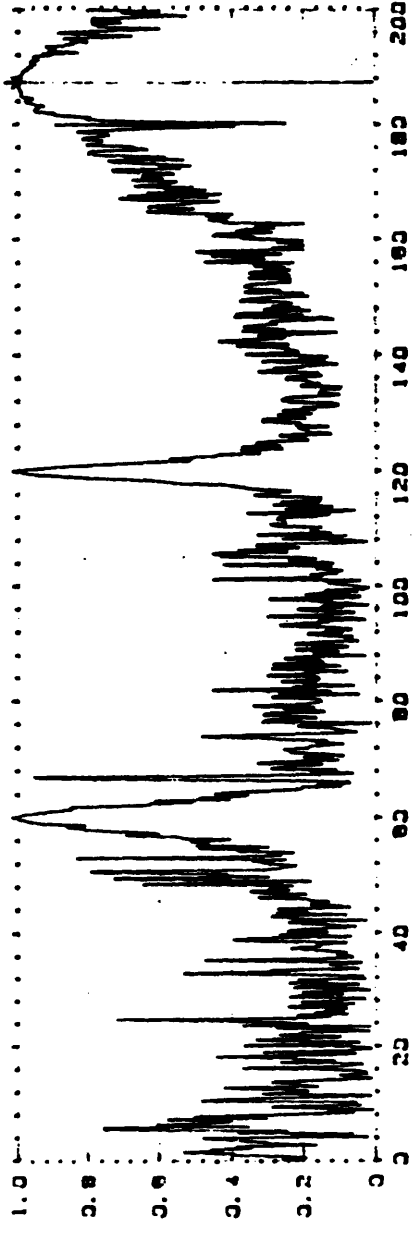
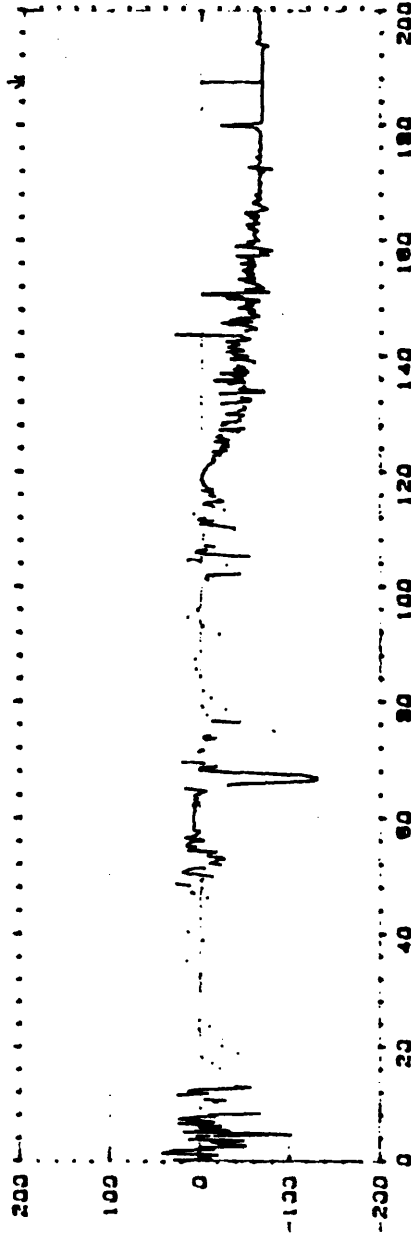
Meas.  
Object:

\_\_\_\_\_  
\_\_\_\_\_  
\_\_\_\_\_  
\_\_\_\_\_

Comments:

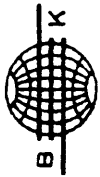
\_\_\_\_\_  
\_\_\_\_\_  
\_\_\_\_\_  
\_\_\_\_\_

W22 CROSS SPEC PHASE INPUT MAIN Y: -67.9DEG  
Y: 200 TO +200 DEG X: 187.25HZ  
X: 0.00HZ + 200HZ -IN  
SETJP W22 WA: 100



W23 COHERENCE MAIN Y: 1.00  
Y: 1.00 X: 187.25HZ  
X: 0.00HZ + 200HZ -IN  
SETJP W23 WA: 100





Brüel & Kjær

Type 2032

Page No.  
69

Sign.:

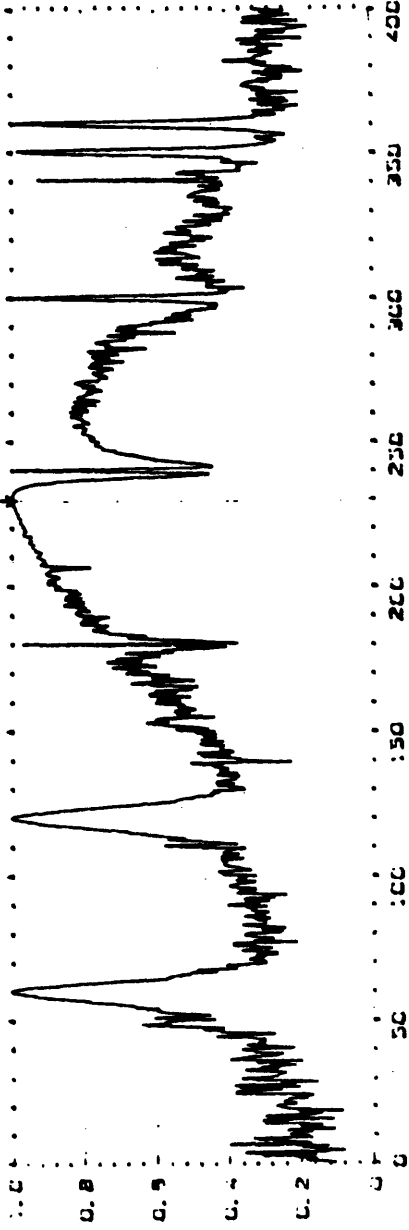
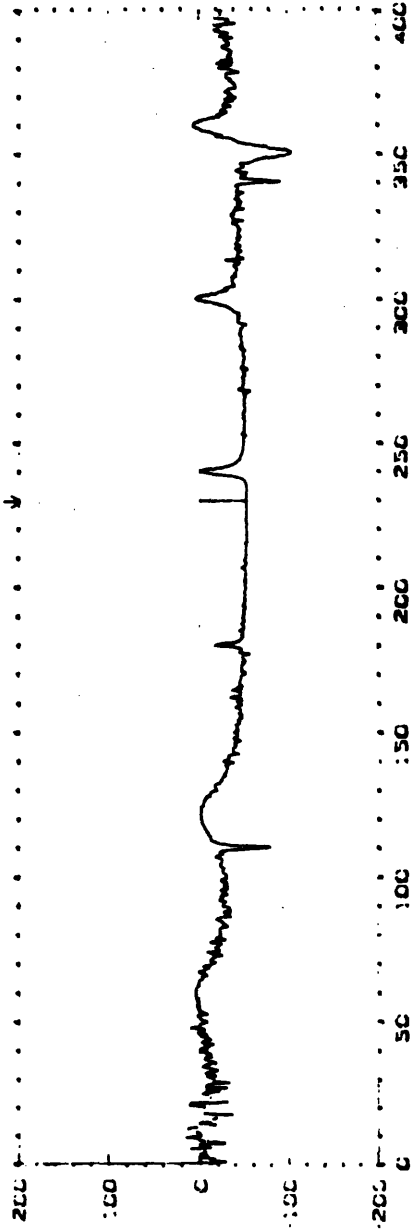
Magn.  
Object:

\_\_\_\_\_  
\_\_\_\_\_  
\_\_\_\_\_  
\_\_\_\_\_

Comments:

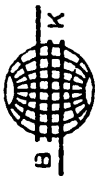
\_\_\_\_\_  
\_\_\_\_\_  
\_\_\_\_\_  
\_\_\_\_\_

W22 CROSS SPEC PHASE INPUT MAIN Y: -53.4DEG  
Y: -200 X: 229.5HZ  
X: 0.042 #A: 100  
SATUR 422 #A: 100



W23 COHERENCE  
Y: 1.00  
X: 0.042 #A: 100  
SATUR 422 #A: 100

MA: 1.00  
Y: 1.00  
X: 229.5HZ



Brüel & Kjær

Type 2032

Page No.  
75

Sign.:

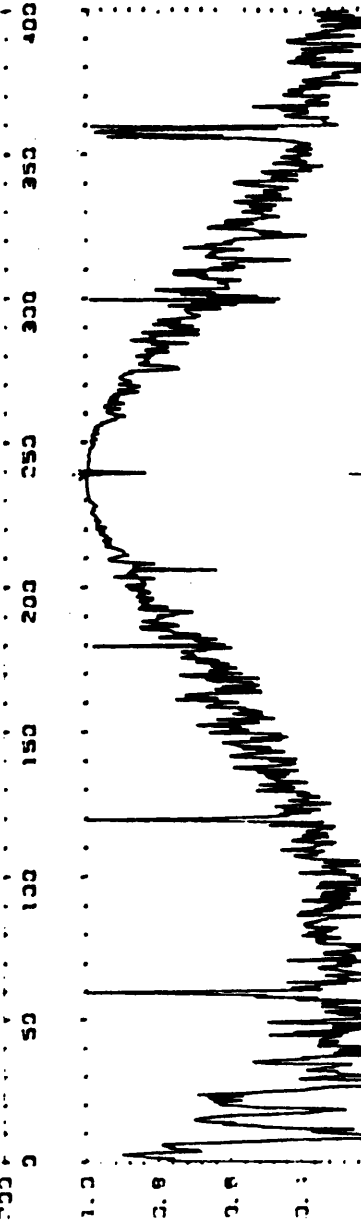
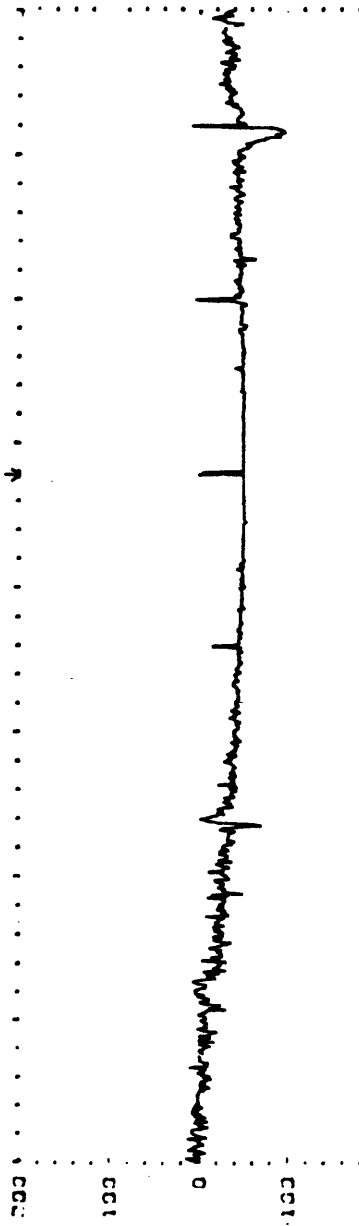
Meas.  
Object:

\_\_\_\_\_  
\_\_\_\_\_  
\_\_\_\_\_  
\_\_\_\_\_

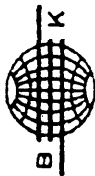
Comments:

\_\_\_\_\_  
\_\_\_\_\_  
\_\_\_\_\_  
\_\_\_\_\_

W22 CROSS SPEC PHASE INPUT MAIN Y: -50.9 DEG  
X: 239.0 Hz  
% 1.00  
% 239.0 Hz  
MA: 100



W23 COHERENCE  
% 1.00  
% 239.0 Hz  
MA: 100  
MAIN Y: 1.00  
X: 239.0 Hz



Brüel & Kjær

Type 2032

Page No.  
66

Sign.:

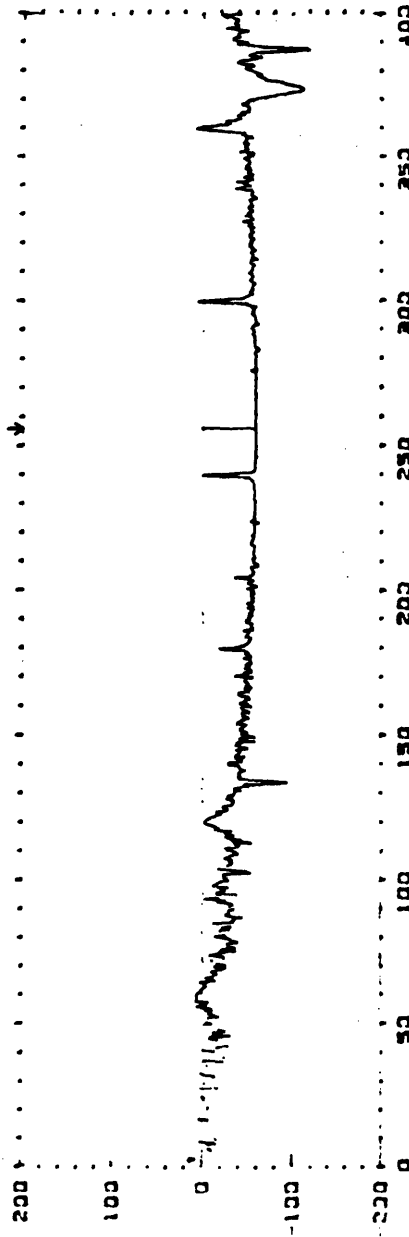
Meas.  
Obj Ject:

\_\_\_\_\_  
\_\_\_\_\_  
\_\_\_\_\_  
\_\_\_\_\_  
\_\_\_\_\_

Comments:

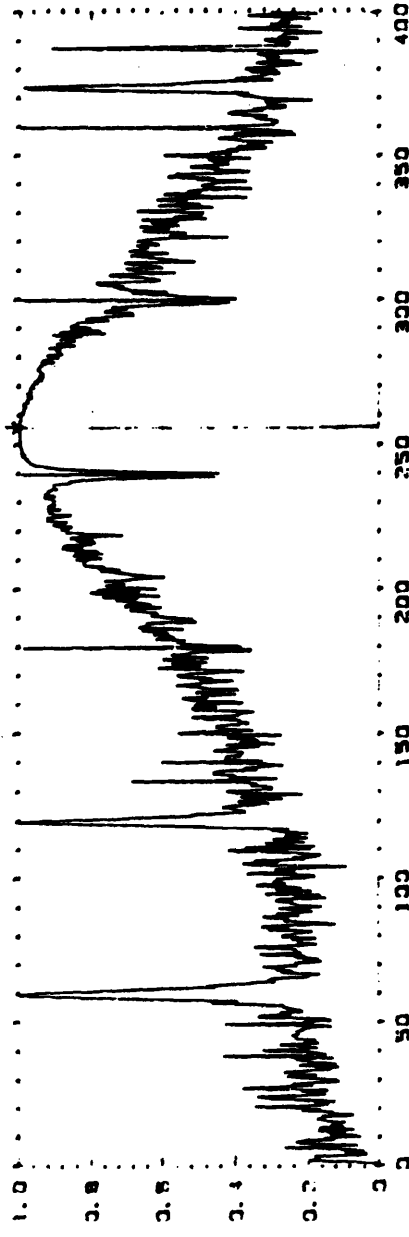
\_\_\_\_\_  
\_\_\_\_\_  
\_\_\_\_\_  
\_\_\_\_\_

W22 CROSS SPEC PHASE INPUT MAIN Y: -59.7DEG  
% 200 TO 400 Hz X: 256.0Hz  
% 0.0Hz + 400Hz  
SETUP W22 MA: 100

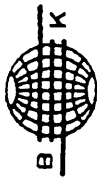


100

W23 COHERENCE  
% 1.00  
% 0.0Hz + 400Hz  
SETUP W23 MA: 100



MAIN Y: 1.00  
% 256.0Hz



Brüel & Kjær

Type 2032

Page No.  
67

Sign.:

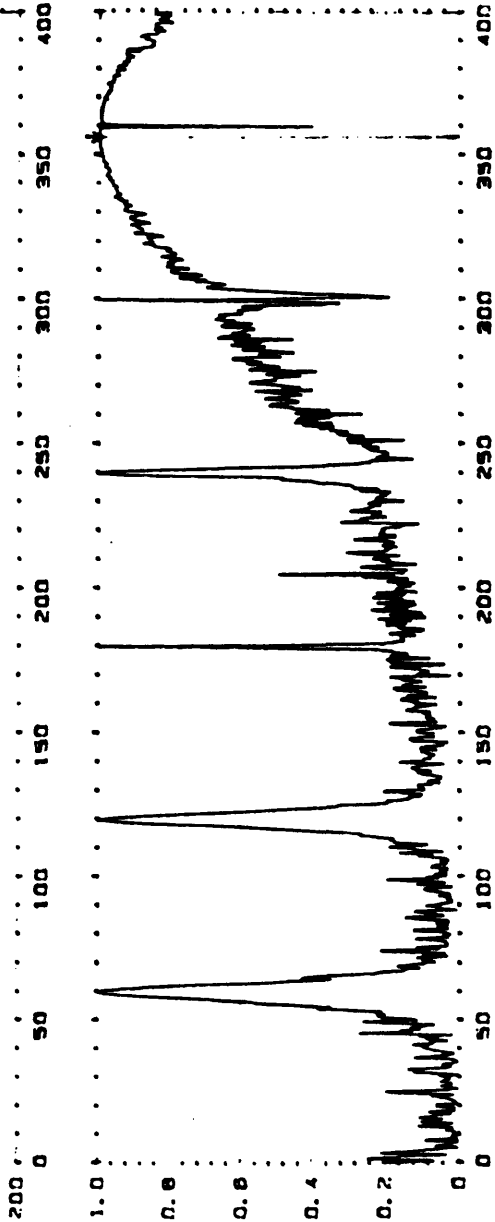
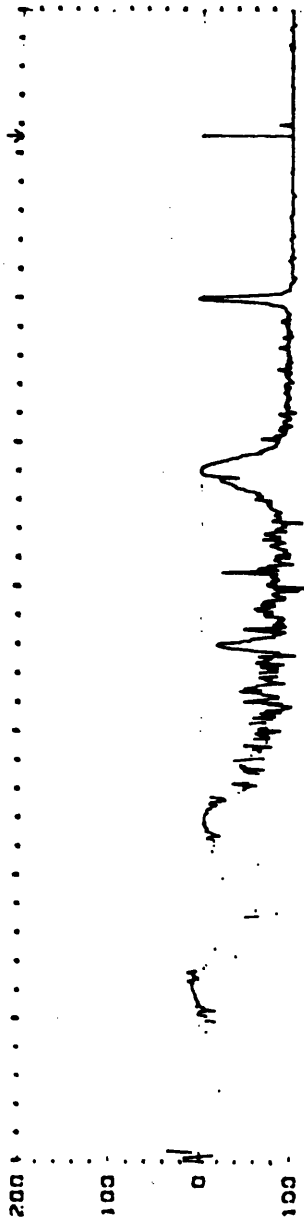
Meas.  
Object:

\_\_\_\_\_  
\_\_\_\_\_  
\_\_\_\_\_  
\_\_\_\_\_

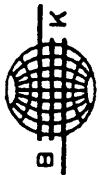
Comments:

\_\_\_\_\_  
\_\_\_\_\_  
\_\_\_\_\_  
\_\_\_\_\_

W22 CROSS SPEC PHASE INPUT MAIN Y: -101.2DEG  
Y: 200 TO +200 DFC X: 356.0Hz  
X: 0.0Hz + 400Hz L.II:  
SETUP W22 #A: 100



W23 COHERENCE MAIN Y: 1.00  
Y: 1.00 X: 356.0Hz  
X: 0.0Hz + 400Hz L.II:  
SETUP W22 #A: 100



Brüel & Kjær

Type 2032

Page No.  
53

Sign.:

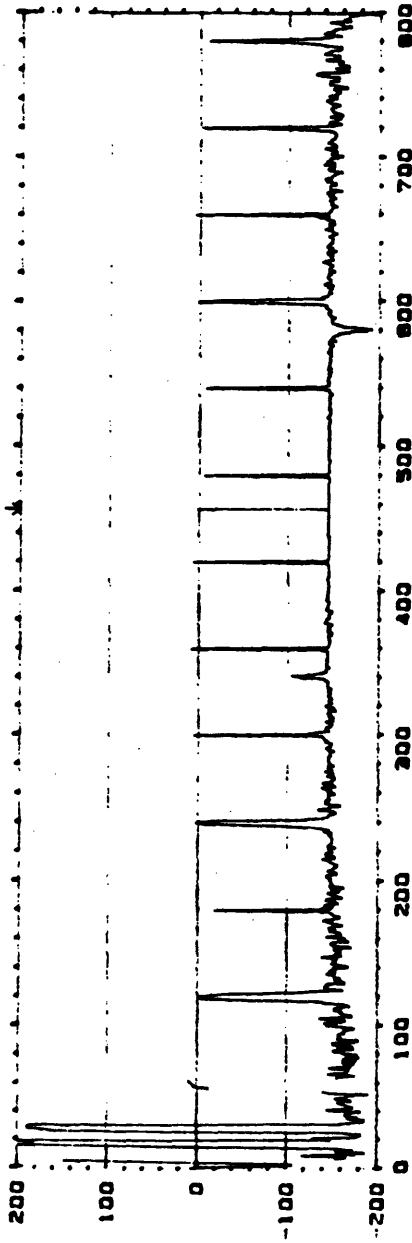
Made.  
Object:

\_\_\_\_\_  
\_\_\_\_\_  
\_\_\_\_\_  
\_\_\_\_\_

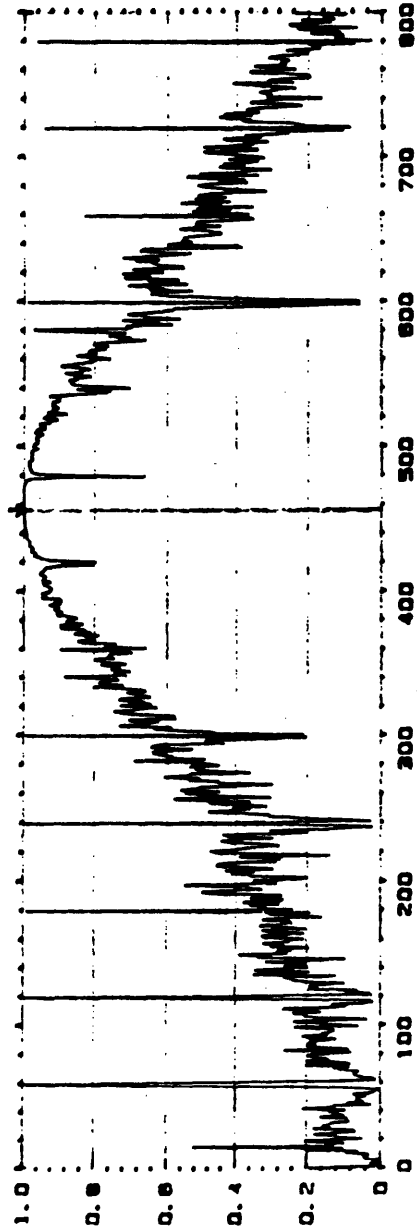
Comments:

\_\_\_\_\_  
\_\_\_\_\_  
\_\_\_\_\_  
\_\_\_\_\_

W22 FREQ RESP H1 PHASE INPUT MAIN Y<sub>1</sub> -145.0DEG  
Y<sub>1</sub> -200 TO +200 DEC X<sub>1</sub> 456Hz  
X<sub>1</sub> 0Hz ± 800Hz LIN  
SETUP #22 #A: 100

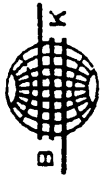


-85-



W23 COHERENCE MAIN Y<sub>1</sub> 1.00  
Y<sub>1</sub> 1.00 X<sub>1</sub> 456Hz

X<sub>1</sub> 0Hz ± 800Hz LIN  
SETUP #22 #A: 100



Brüel & Kjær

Type 2032

Page No.  
71

Sign.:

Meas.

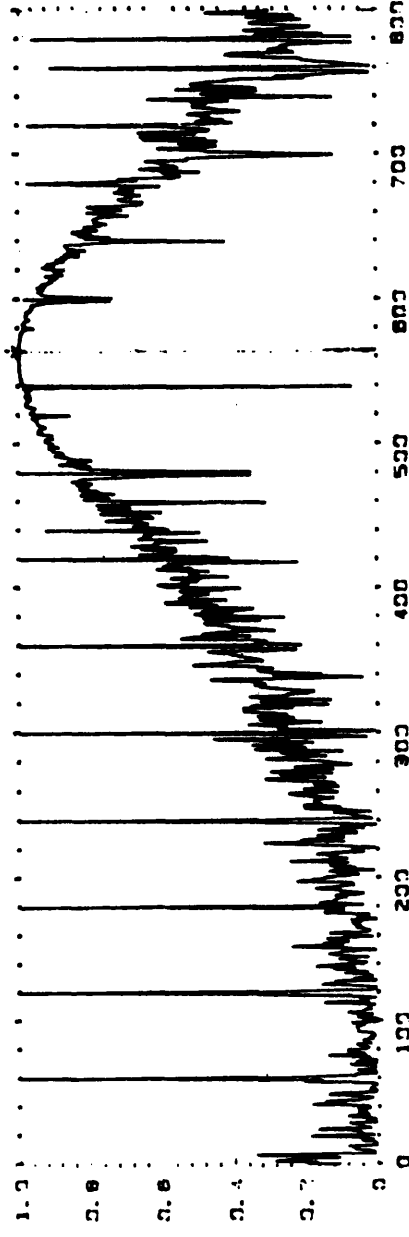
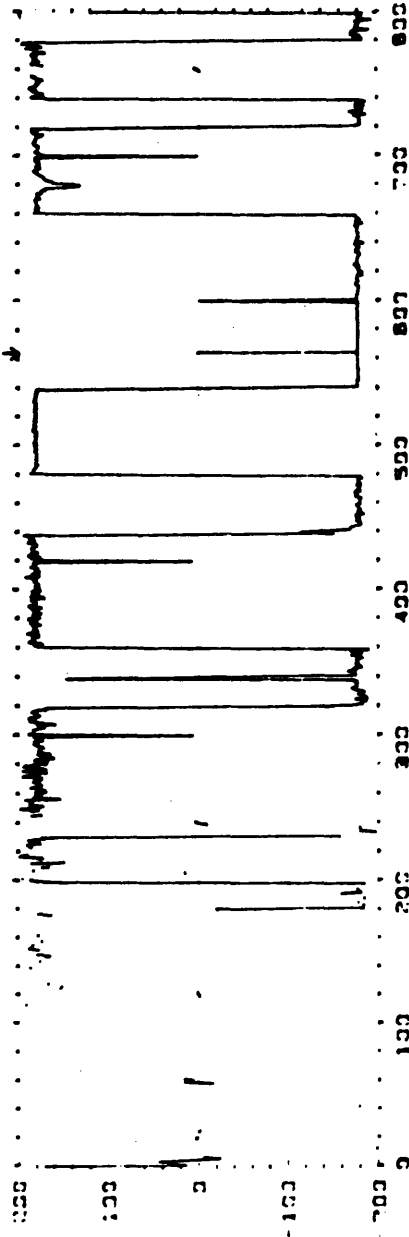
Object:

\_\_\_\_\_  
\_\_\_\_\_  
\_\_\_\_\_  
\_\_\_\_\_

Comments:

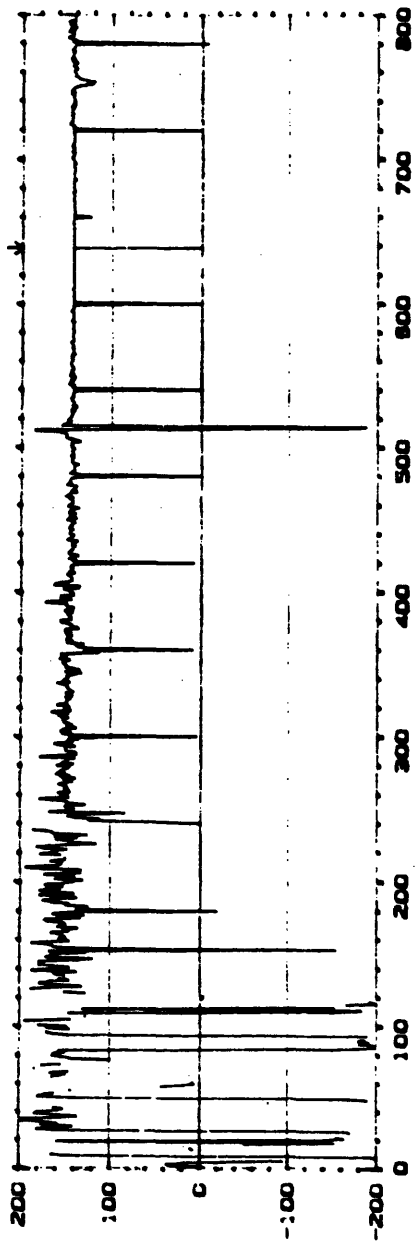
\_\_\_\_\_  
\_\_\_\_\_  
\_\_\_\_\_  
\_\_\_\_\_

W22 CROSS SPEC PHASE INPUT MAIN Y: -180.0DEG  
X: 564Hz  
Y: 200 TO 800 Hz  
X: 0Hz TO 800Hz  
S: 100 200 #A: 100

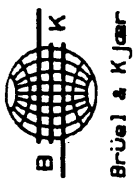
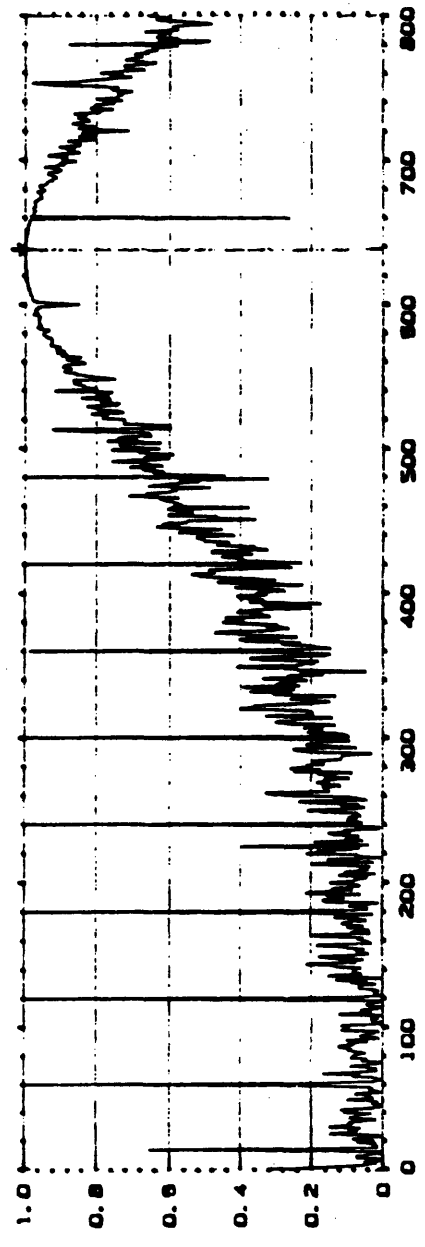


W23 COHERENCE  
Y: 1.00  
X: 0Hz TO 800Hz  
S: 100 200 #A: 100  
MAIN Y: 1.00  
X: 564Hz

W22 CROSS SPEC PHASE INPUT MAIN Y: 144.1 DEG  
 Y: -200 TO +200 DEG X: 638Hz  
 X: 0Hz ~ 800Hz LIN  
 SETUP W22 #A: 100



W23 COHERENCE MAIN Y: 1.00  
 Y: 1.00 X: 638Hz  
 X: 0Hz ~ 800Hz LIN  
 SETUP W22 #A: 100



Type 2032

Page No. 51

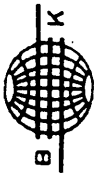
Sign.:

Mass.  
Object:

\_\_\_\_\_  
 \_\_\_\_\_  
 \_\_\_\_\_  
 \_\_\_\_\_

Comments:

\_\_\_\_\_  
 \_\_\_\_\_  
 \_\_\_\_\_  
 \_\_\_\_\_



Brüel & Kjær

Type 2032

Page No.  
49

Sign.:

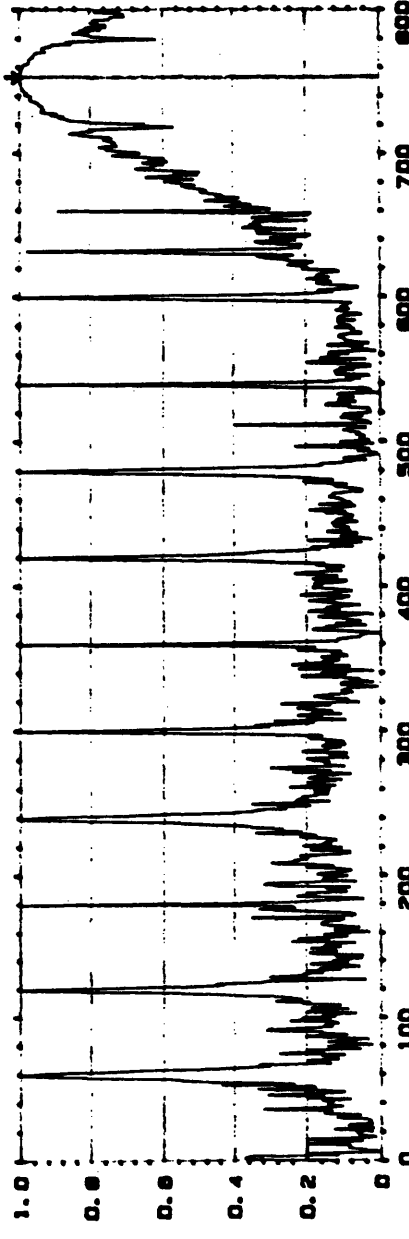
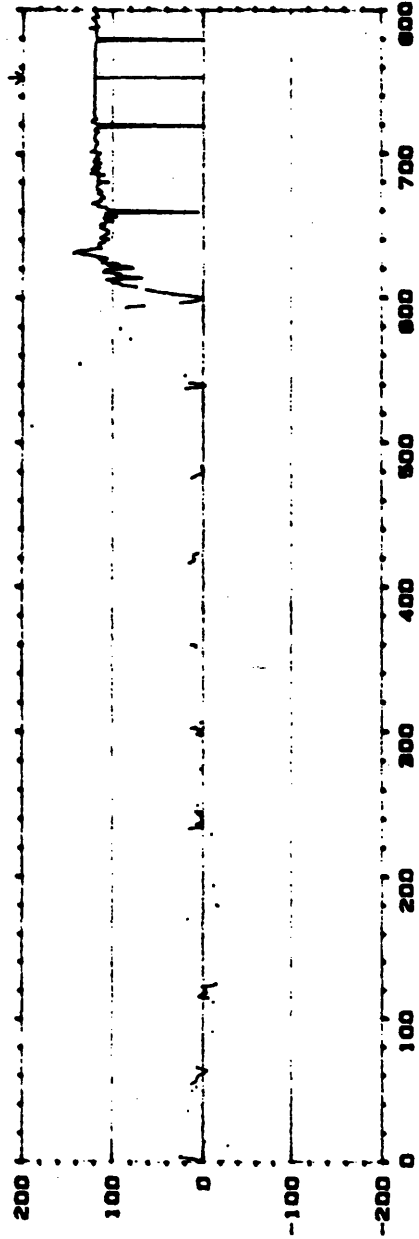
Meas.  
Object:

\_\_\_\_\_  
\_\_\_\_\_  
\_\_\_\_\_  
\_\_\_\_\_

Comments:

\_\_\_\_\_  
\_\_\_\_\_  
\_\_\_\_\_  
\_\_\_\_\_

W22 CROSS SPEC PHASE INPUT MAIN Y: 120.7DEG  
Y: -200 TO +200 DEG X: 753Hz  
X: 0Hz + 800Hz LIN  
SETUP W22 #A: 100



W23 COHERENCE MAIN Y: 1.00  
Y: 1.00 X: 753Hz  
X: 0Hz + 800Hz LIN  
SETUP W22 #A: 100

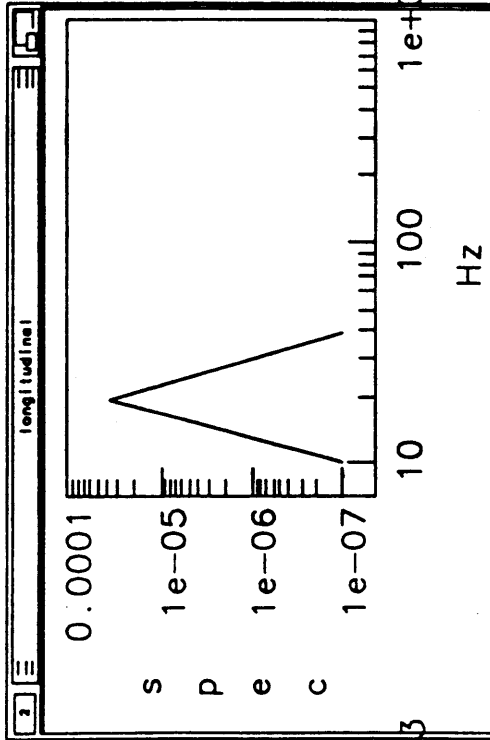
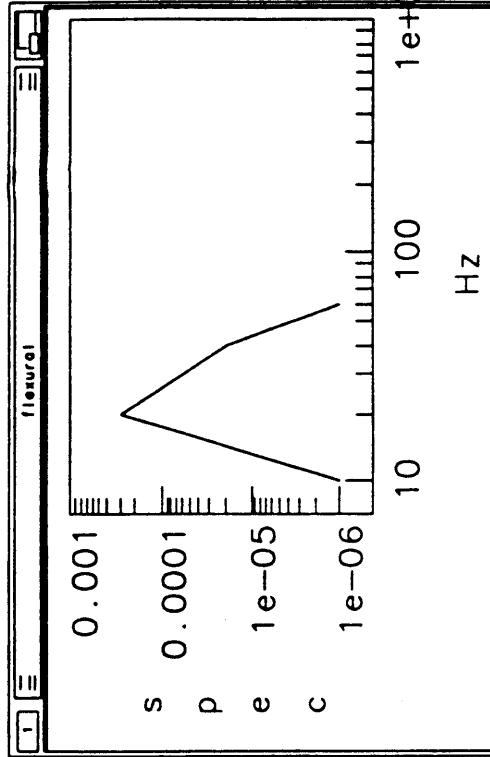
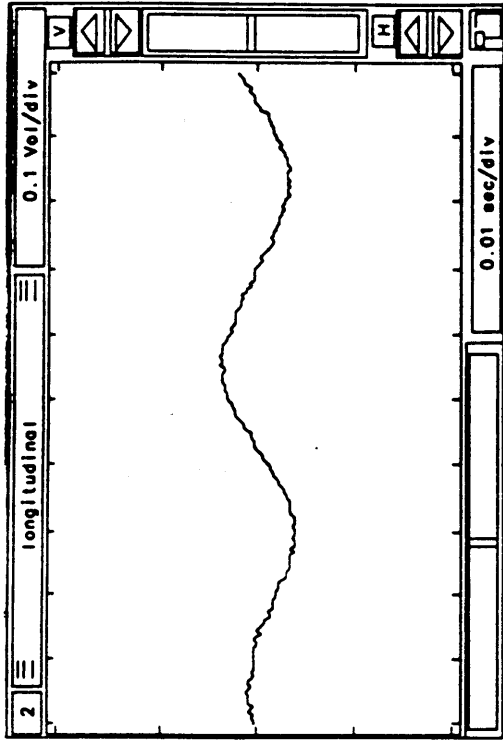
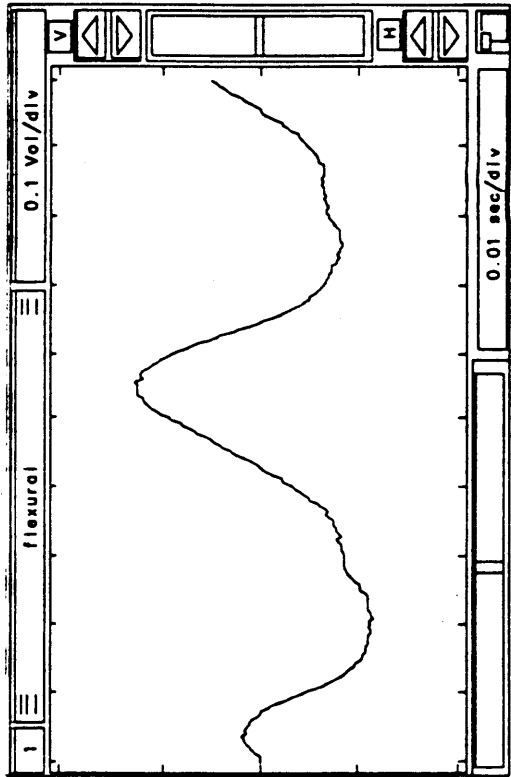


Appendix D: Longitudinal-Flexural Coupling Data(Symmetric Loading)

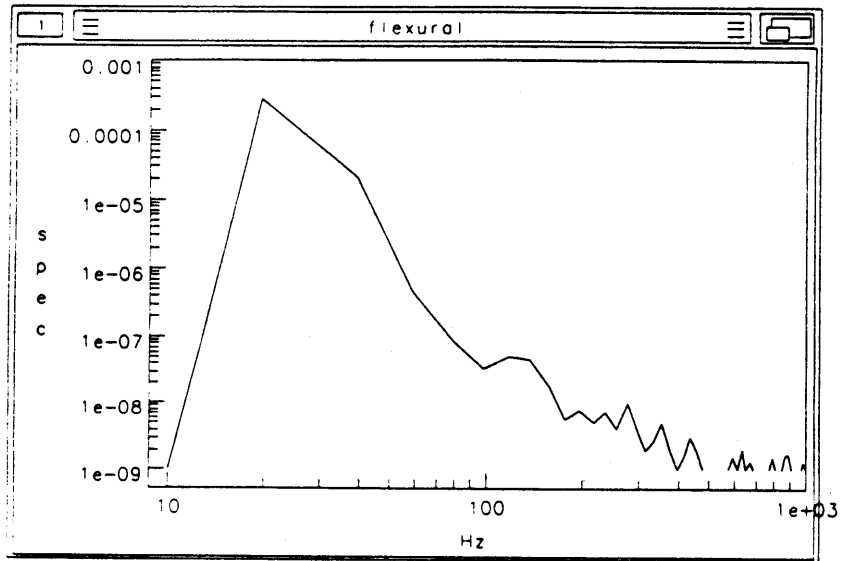
**Power Spectrum Data**

Symmetric loading

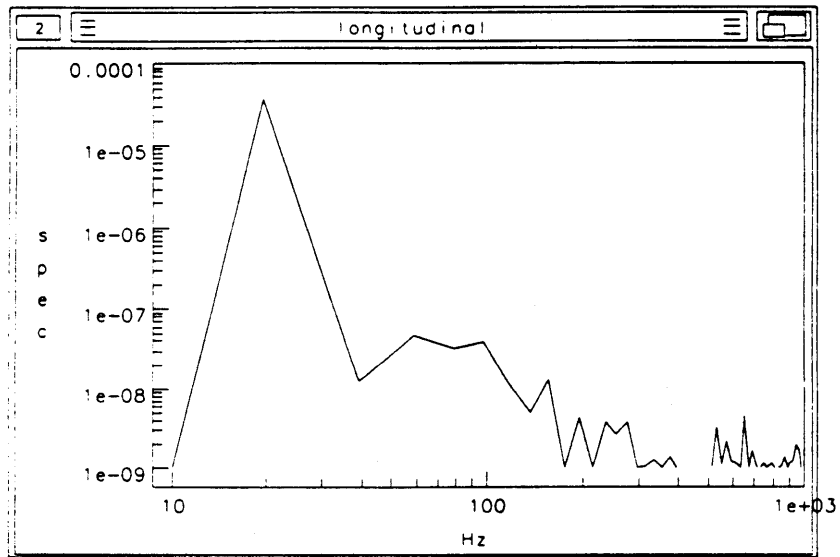
frequency (Hz)	longitudinal ( $\times 10^{-5}$ )	flexural ( $\times 10^{-5}$ )	Energy ratio F/L (dB)
19.531	3.5757	26.916	9
39.531	1.6365	2.6093	2
58.594	1.1876	$5.9952 \times 10^{-2}$	-13
78.125	1.1569	$4.4431 \times 10^{-2}$	-8
117.19	1.2238	$5.3225 \times 10^{-3}$	-24
156.25	0.88226	$8.3782 \times 10^{-5}$	-40
195.31	0.65999	$2.1529 \times 10^{-4}$	-35
410.16	0.69702	$2.7302 \times 10^{-5}$	-44
800.78	0.31303	$1.5111 \times 10^{-6}$	-53



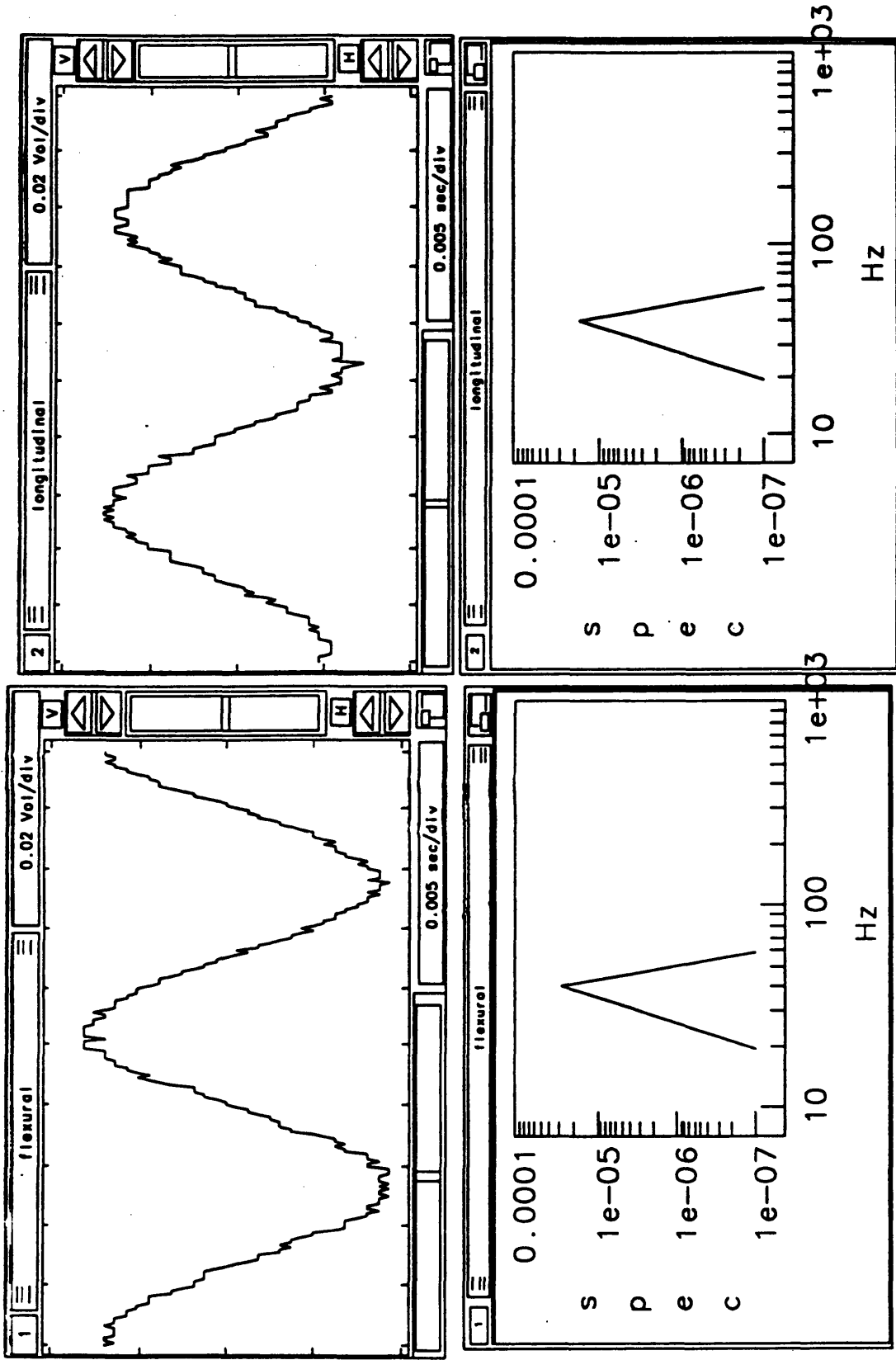
Time series/frequency response of pure tone longitudinal excitation @ 19.531 Hz



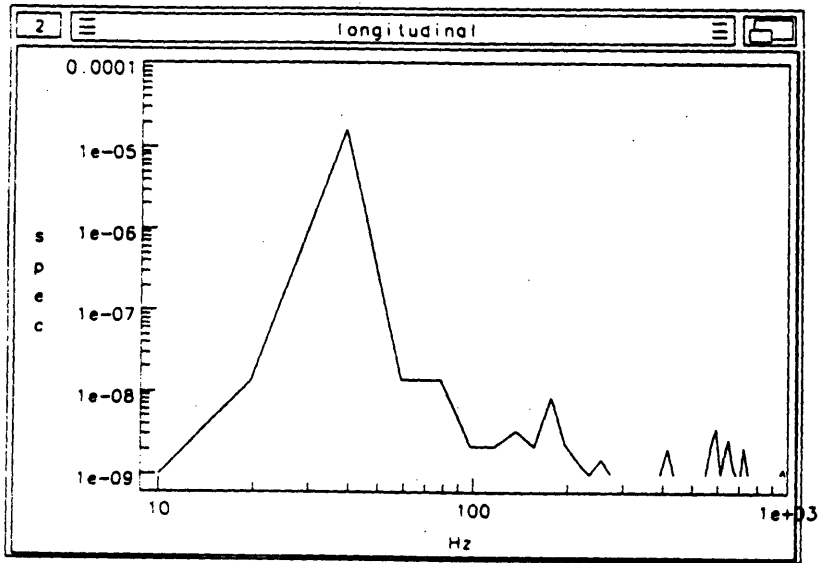
Longitudinal wave power spectrum  
for pure tone excitation @ 19.531 Hz



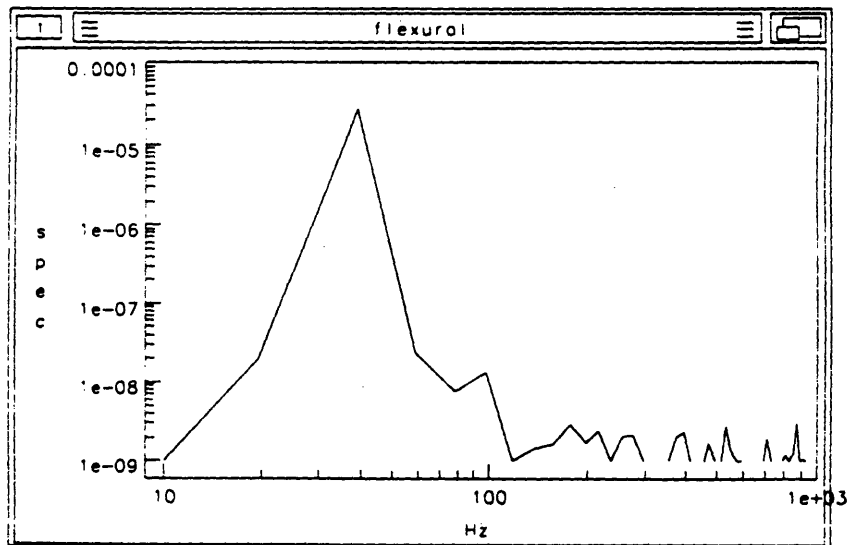
Flexural wave power spectrum for  
pure tone excitation @ 19.531 Hz



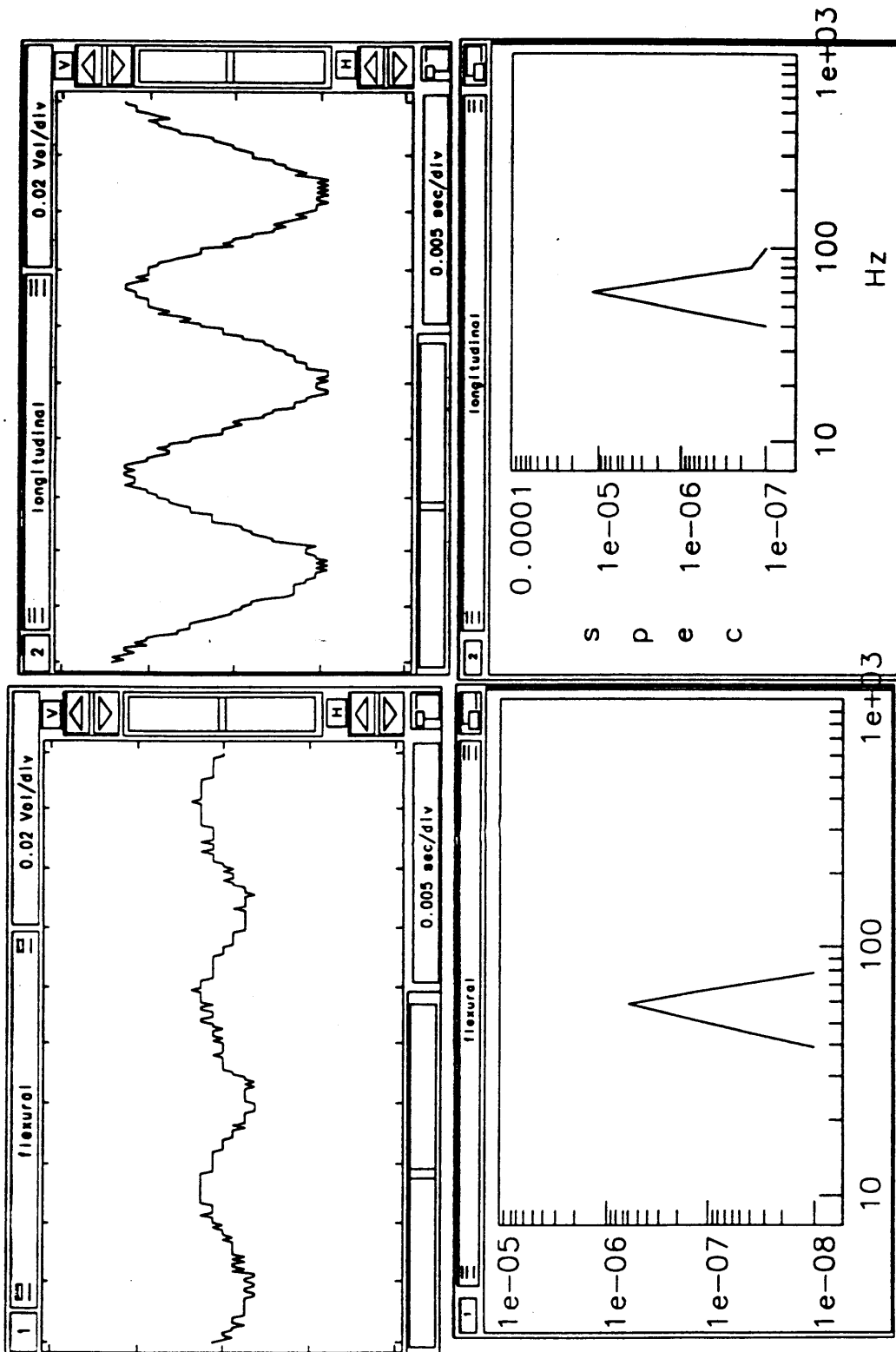
Time series/frequency response of pure tone longitudinal excitation @ 39.531 Hz



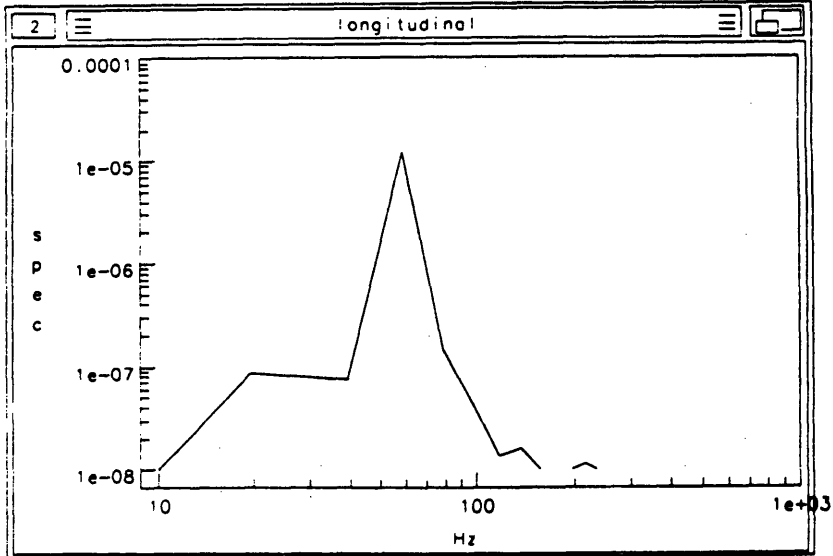
Longitudinal wave power spectrum  
for pure tone excitation @ 39.531 Hz



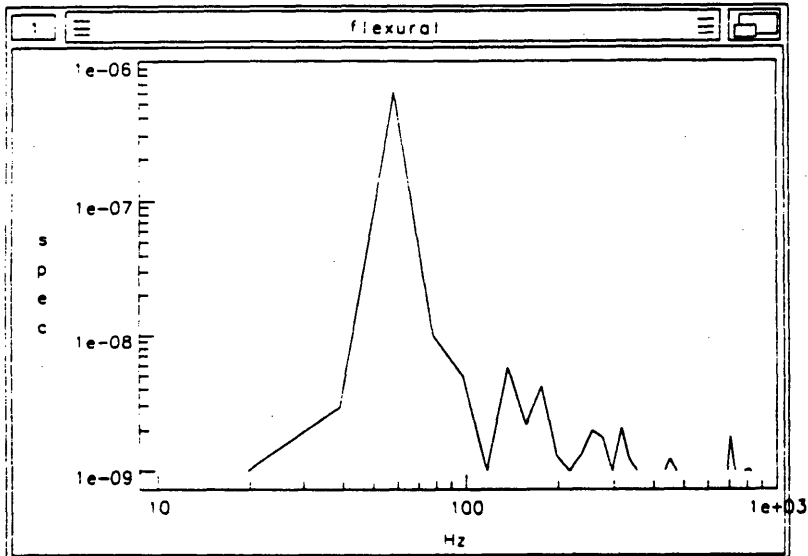
Flexural wave power spectrum for  
pure tone excitation @ 39.531 Hz



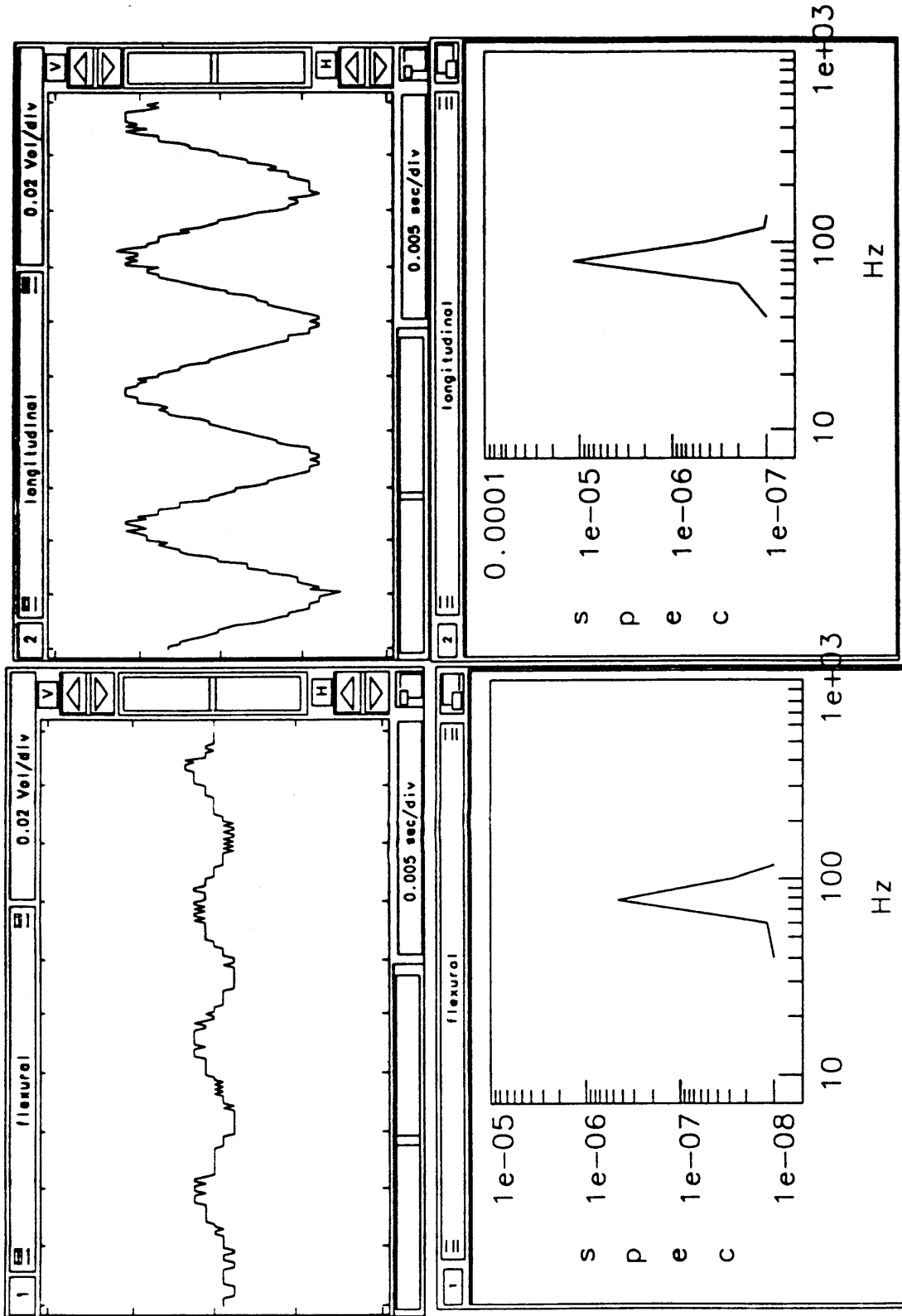
Time series/frequency response of pure tone longitudinal excitation @ 58.594 Hz



Longitudinal wave power spectrum  
for pure tone excitation @ 58.594 Hz

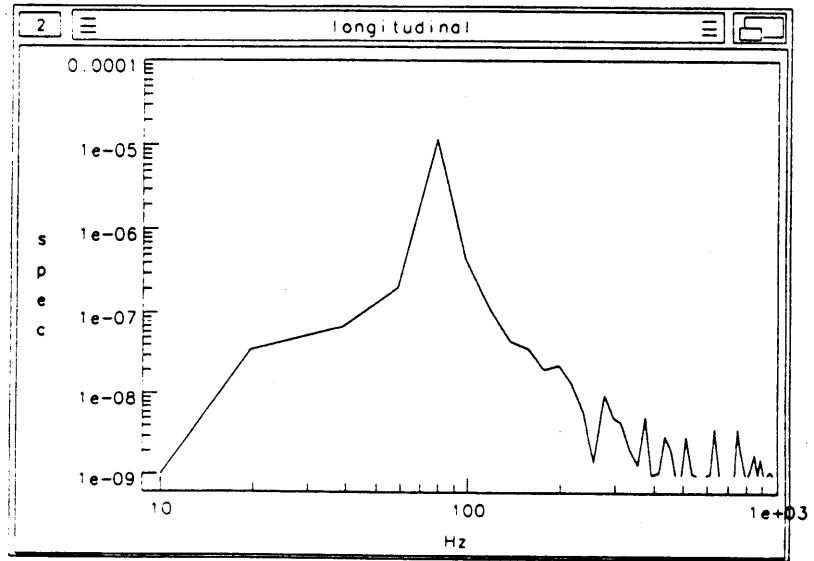


Flexural wave power spectrum for  
pure tone excitation @ 58.594 Hz

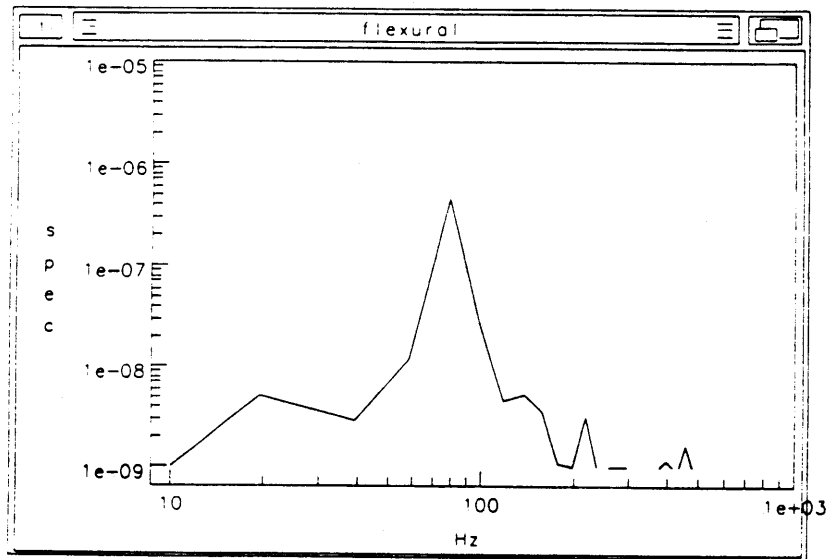


Time series/frequency response of pure tone longitudinal excitation @ 78.125 Hz

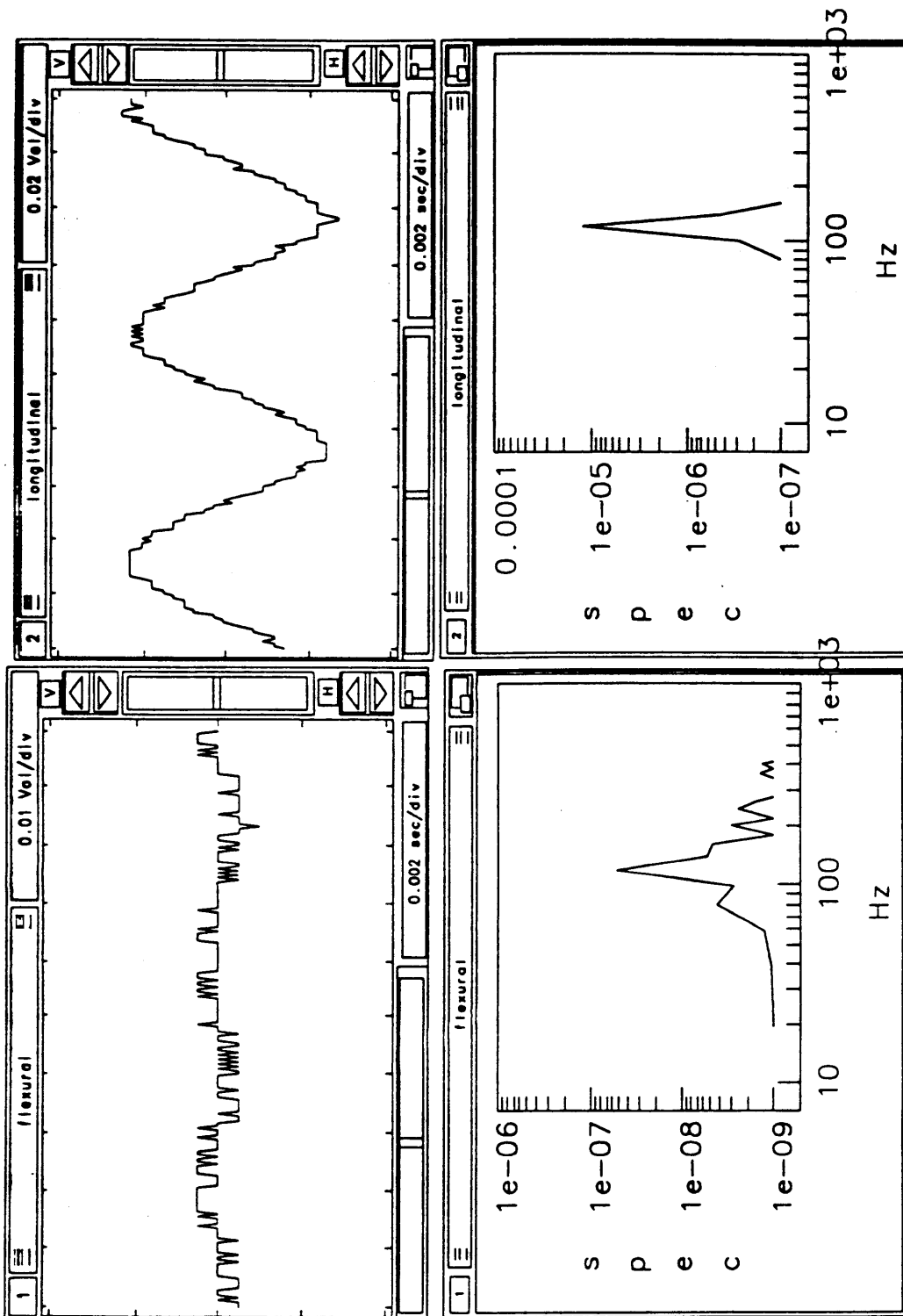




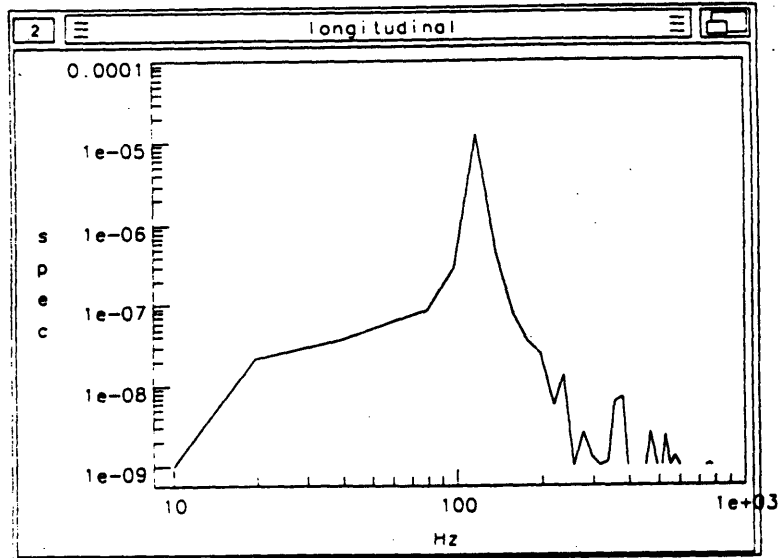
Longitudinal wave power spectrum  
for pure tone excitation @ 78.125 Hz



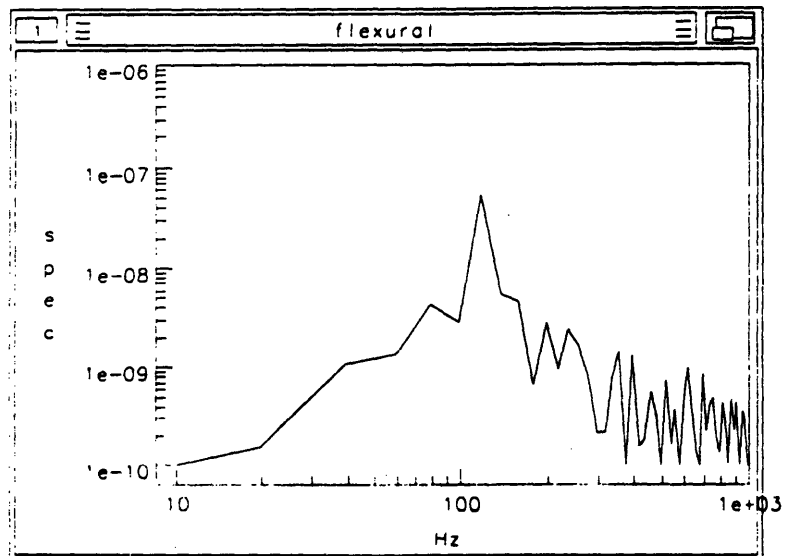
Flexural wave power spectrum for  
pure tone excitation @ 78.125 Hz



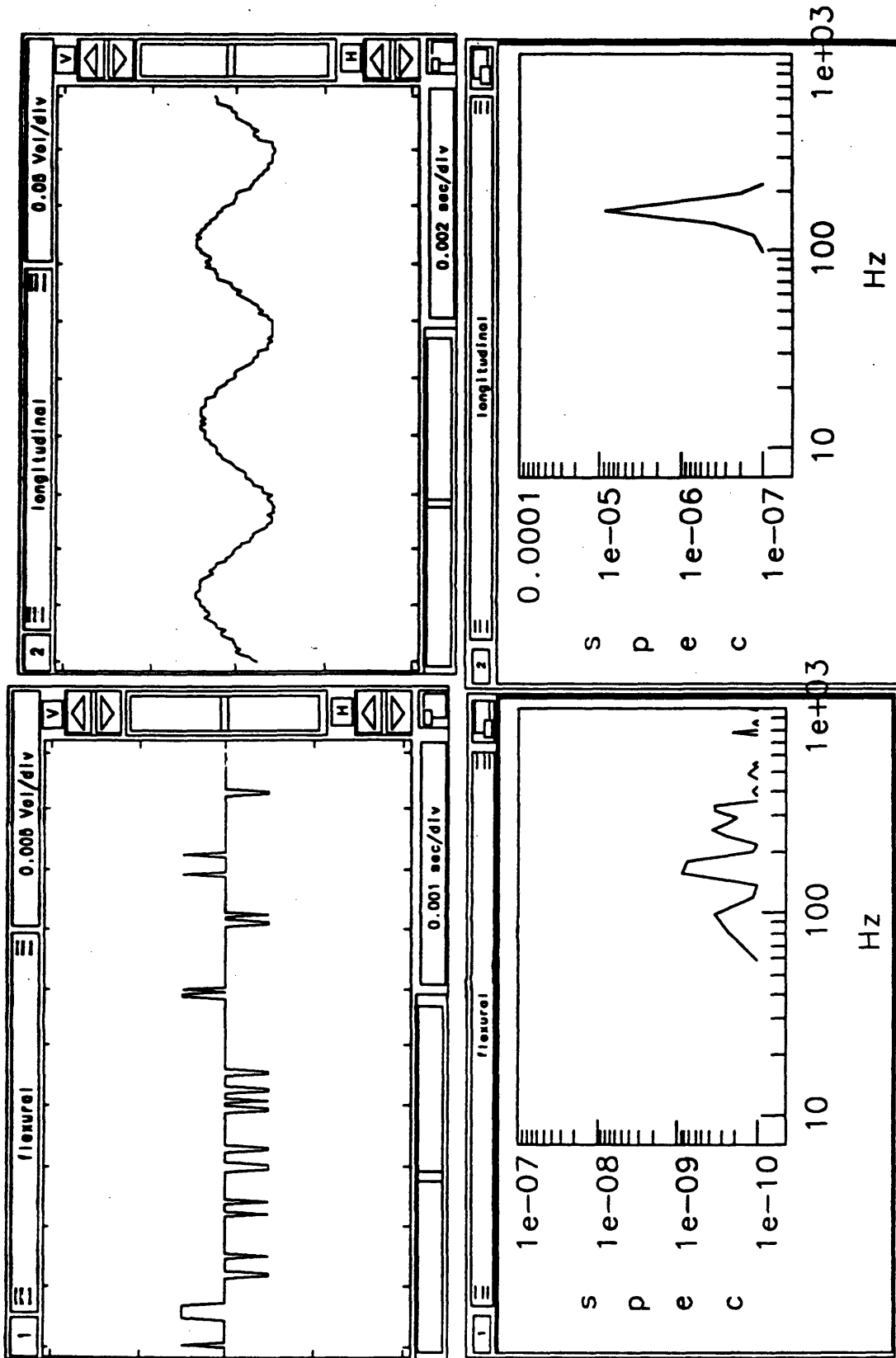
Time series/frequency response of pure tone longitudinal excitation @ 117.19 Hz



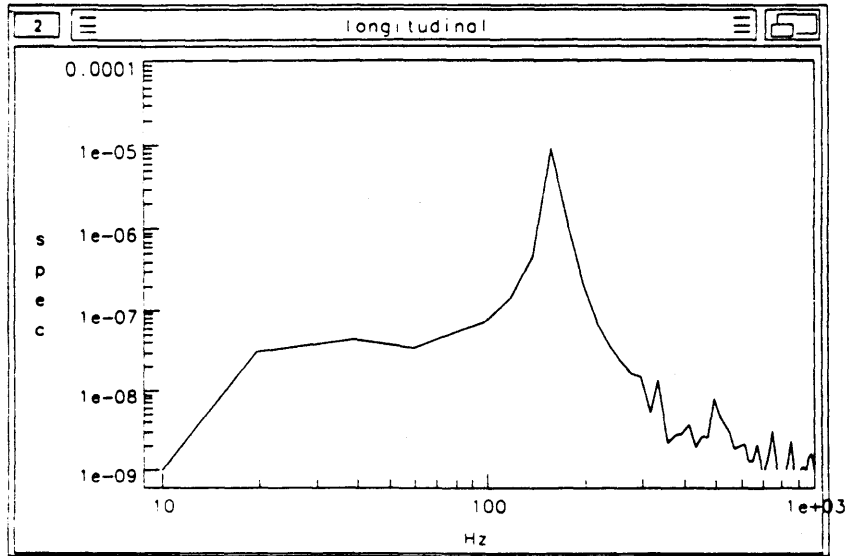
Longitudinal wave power spectrum  
for pure tone excitation @ 117.19 Hz



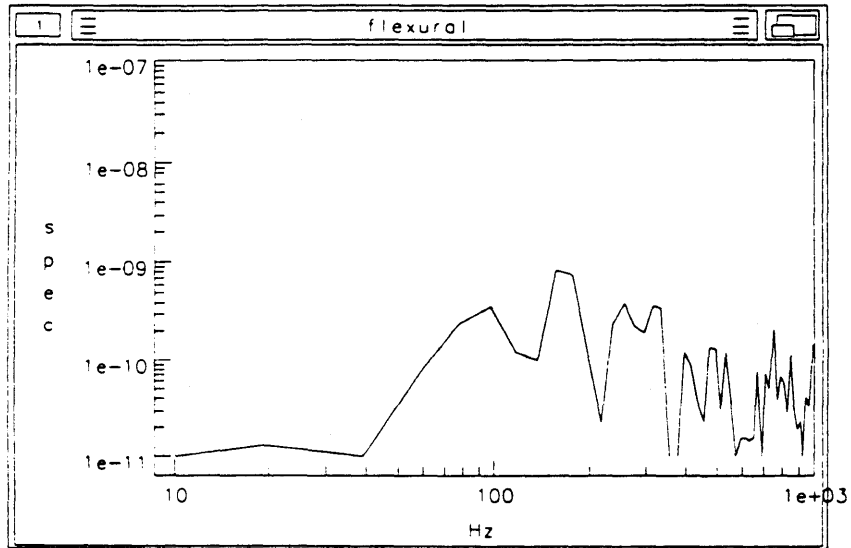
Flexural wave power spectrum for  
pure tone excitation @ 117.19 Hz



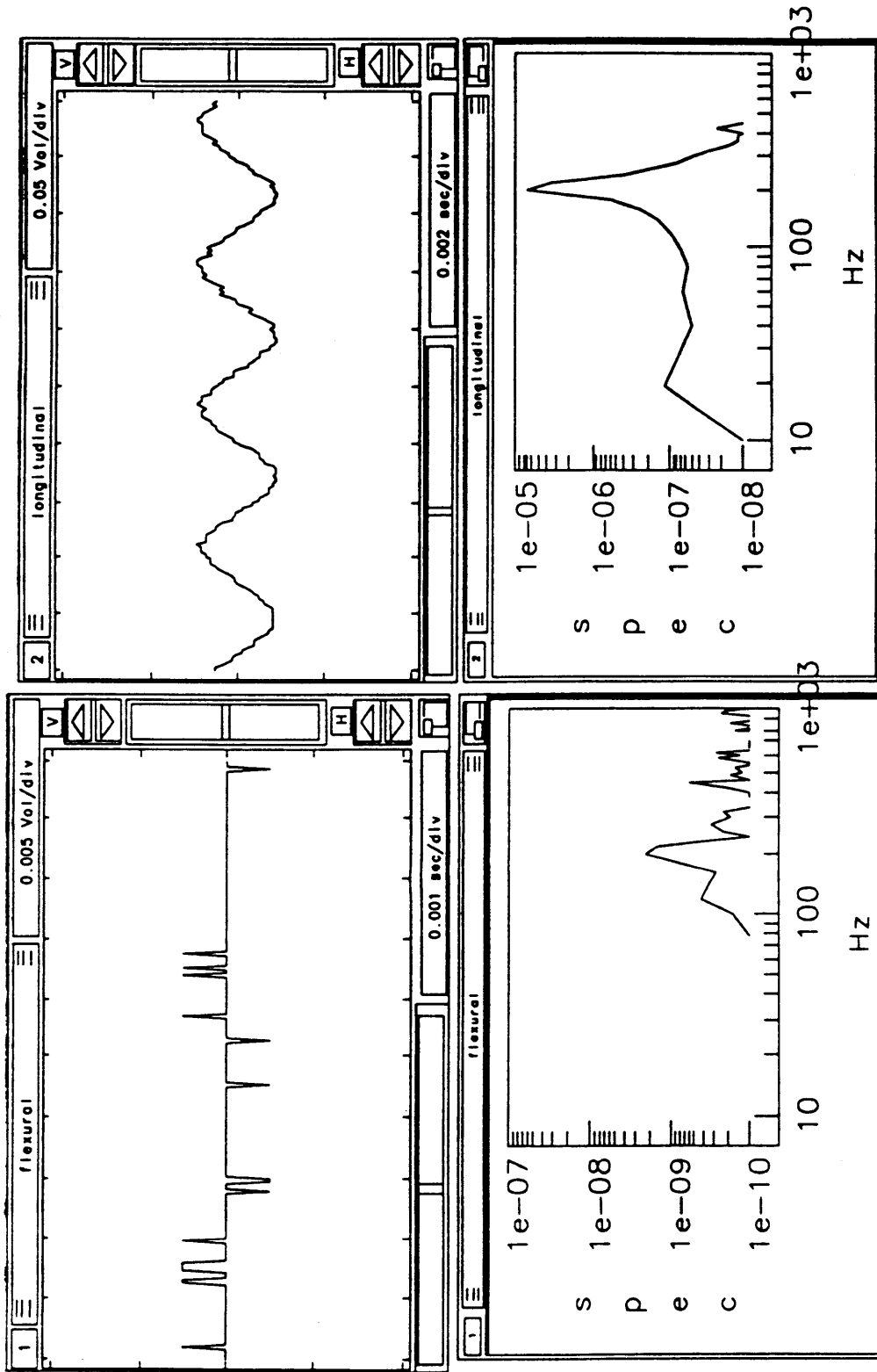
Time series/frequency response of pure tone longitudinal excitation @ 156.25 Hz



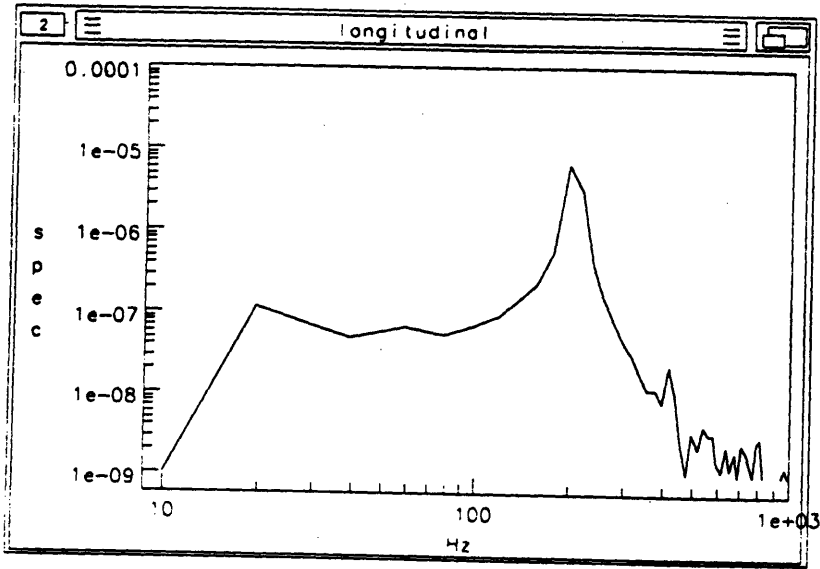
Longitudinal wave power spectrum  
for pure tone excitation @ 156.25 Hz



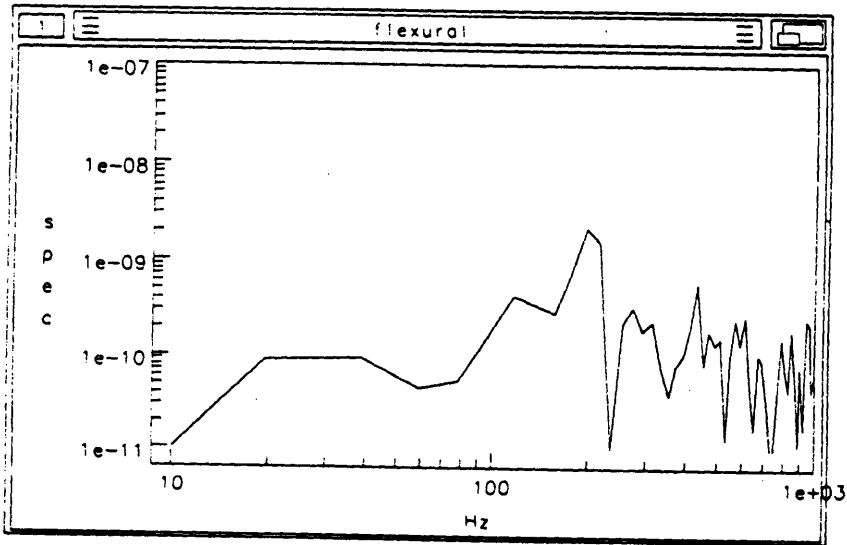
Flexural wave power spectrum for  
pure tone excitation @ 156.25 Hz



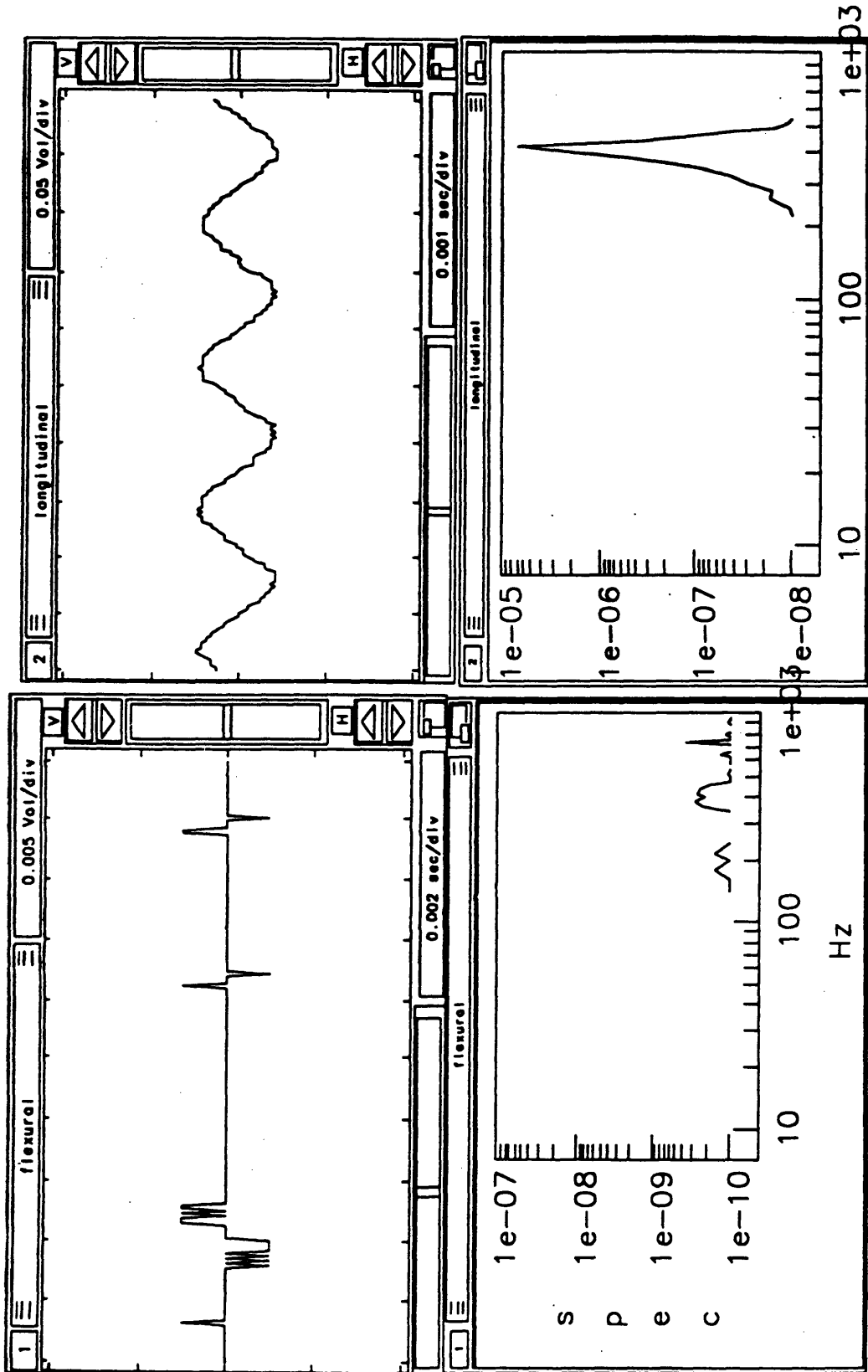
Time series/frequency response of pure tone longitudinal excitation @ 195.31 Hz



Longitudinal wave power spectrum  
for pure tone excitation @ 195.31 Hz

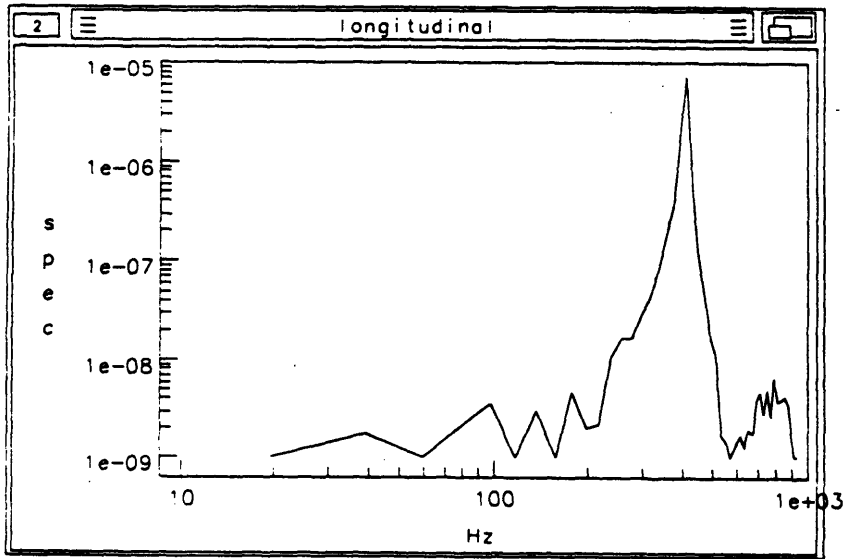


Flexural wave power spectrum for  
pure tone excitation @ 195.31 Hz

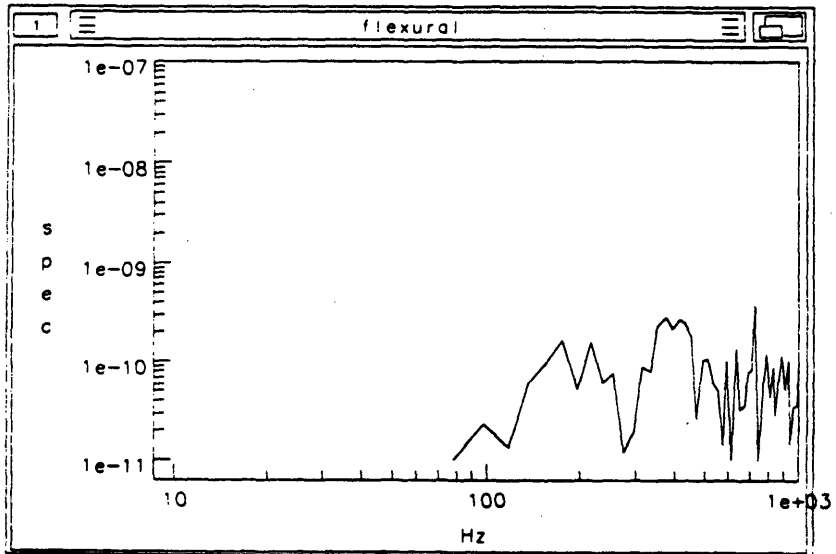


Time series/frequency response of pure tone longitudinal excitation @ 410.16 Hz

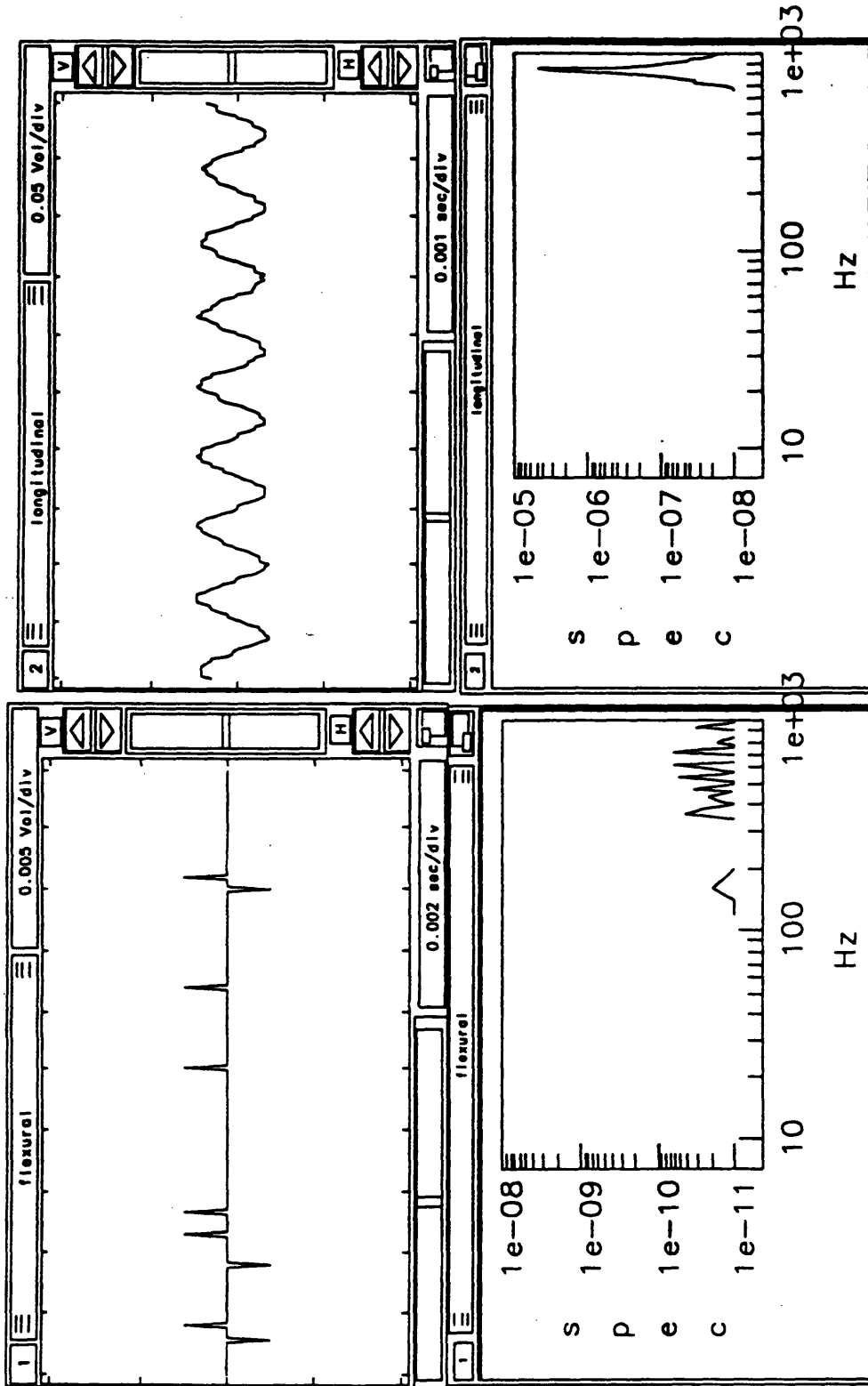




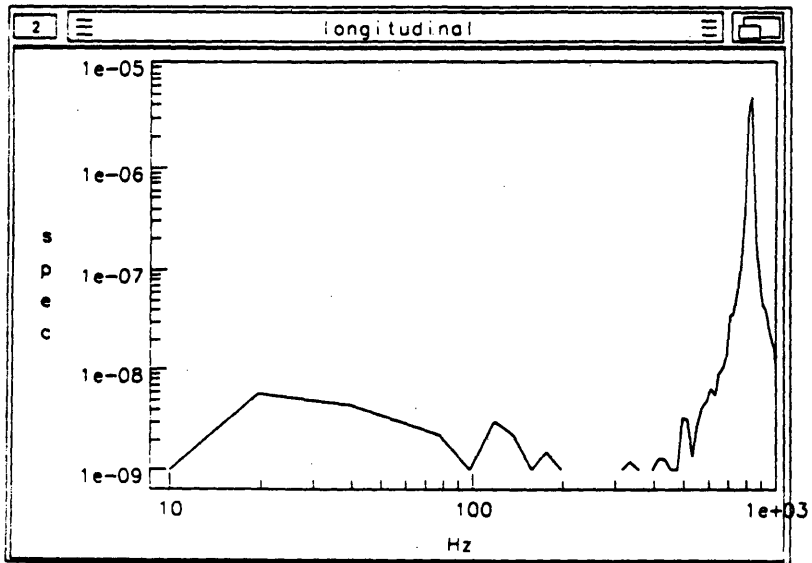
Longitudinal wave power spectrum  
for pure tone excitation @ 410.16 Hz



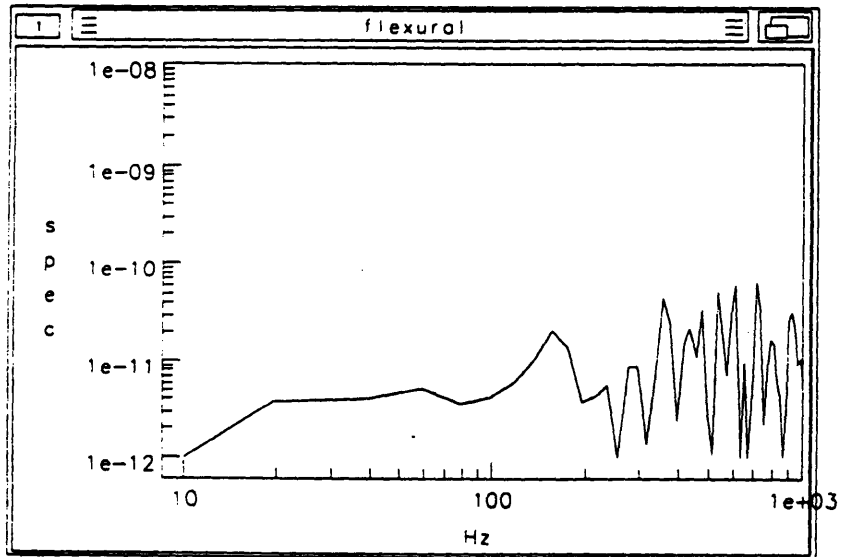
Flexural wave power spectrum for  
pure tone excitation @ 410.16 Hz



Time series/frequency response of pure tone longitudinal excitation @ 800.78 Hz



Longitudinal wave power spectrum  
for pure tone excitation @ 800.78 Hz

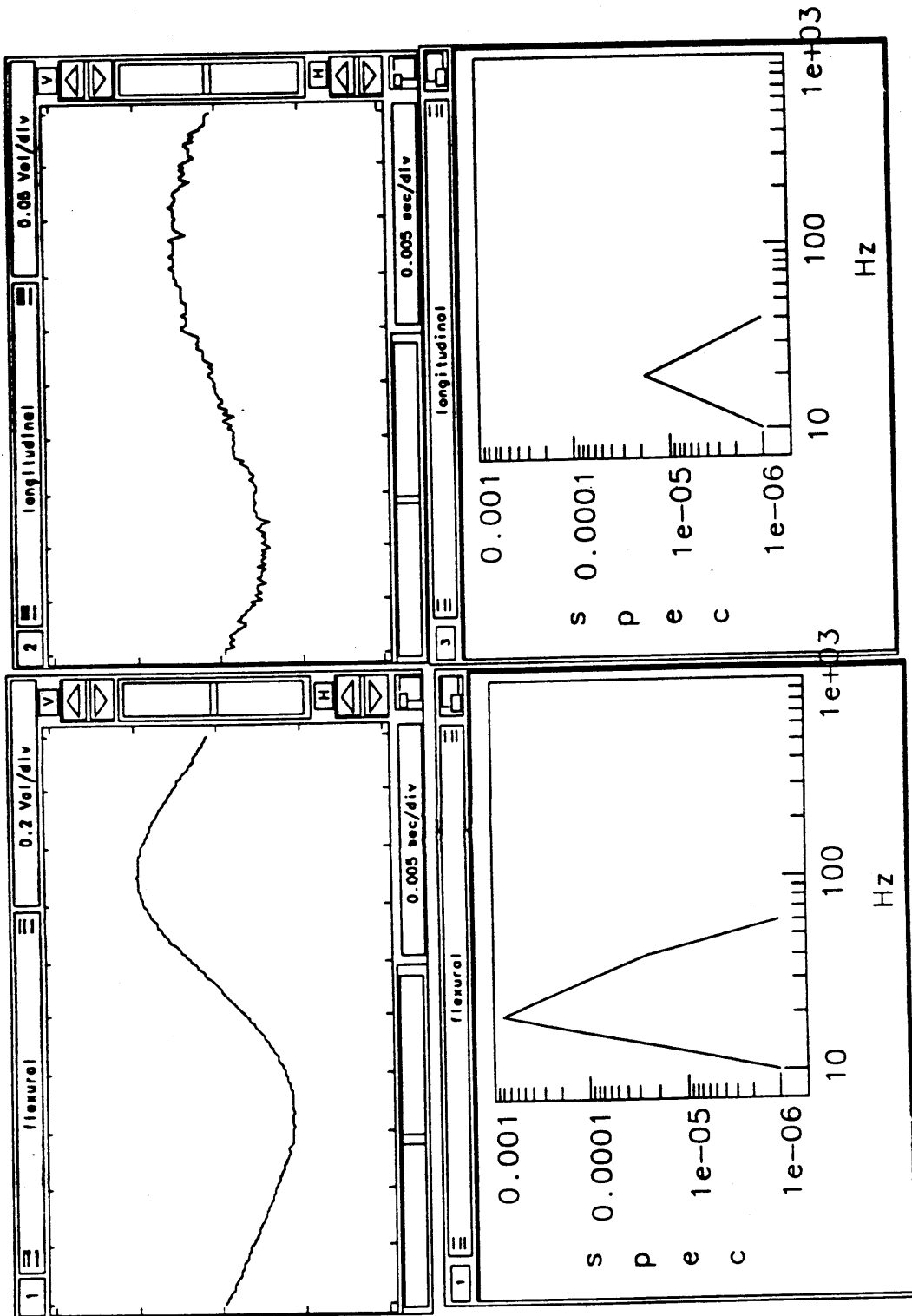


Flexural wave power spectrum for  
pure tone excitation @ 800.78 Hz

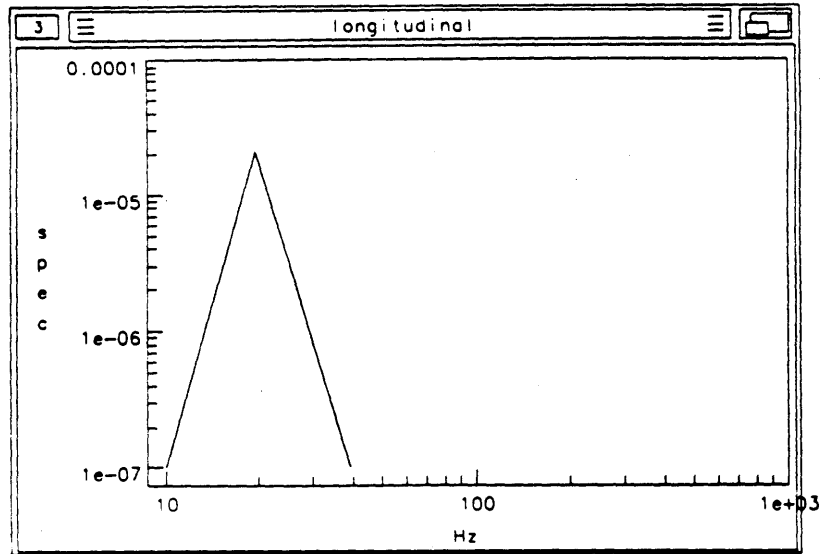
**Appendix E: Longitudinal-Flexural Coupling Data(Asymmetric Loading)**

**Power Spectrum Data**  
Asymmetric loading

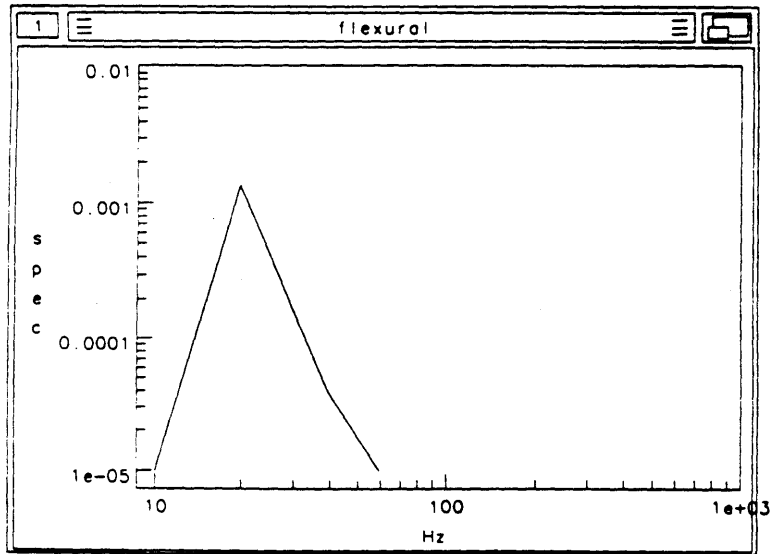
frequency (Hz)	longitudinal ( $\times 10^{-5}$ )	flexural ( $\times 10^{-5}$ )	Energy ratio F/L (dB)
19.531	2.0705	133.37	18
39.063	1.9188	40.502	13
58.594	1.1283	7.7021	8
78.125	1.6532	4.7221	5
117.19	1.6897	0.92276	- 3
156.25	1.1827	0.20135	- 8
195.31	0.83341	$2.8741 \times 10^{-3}$	-25
410.16	0.4790	$4.7251 \times 10^{-3}$	-20
800.78	0.86933	$2.8937 \times 10^{-2}$	-15



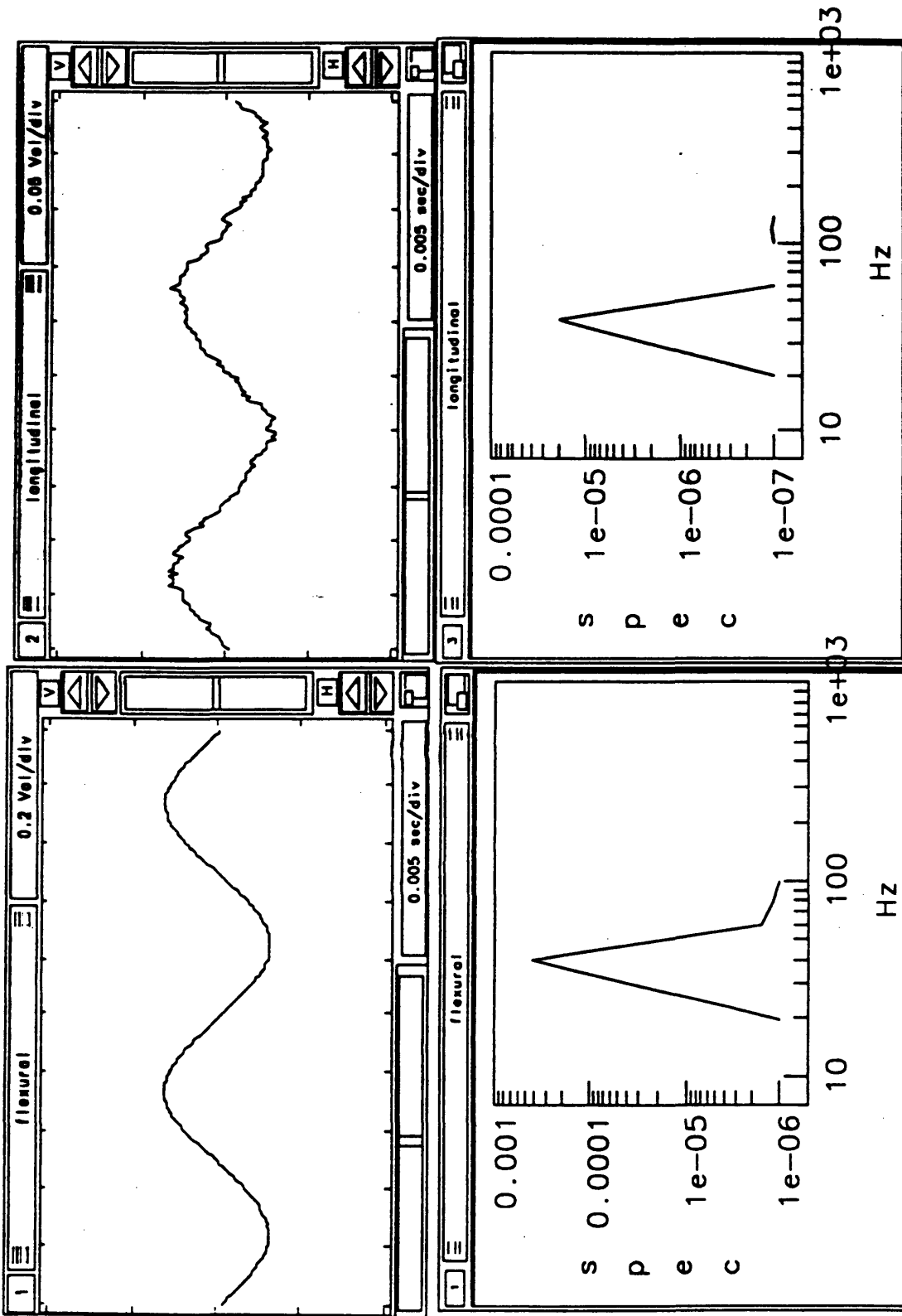
Time series/frequency response of pure tone longitudinal excitation @ 19.531 Hz



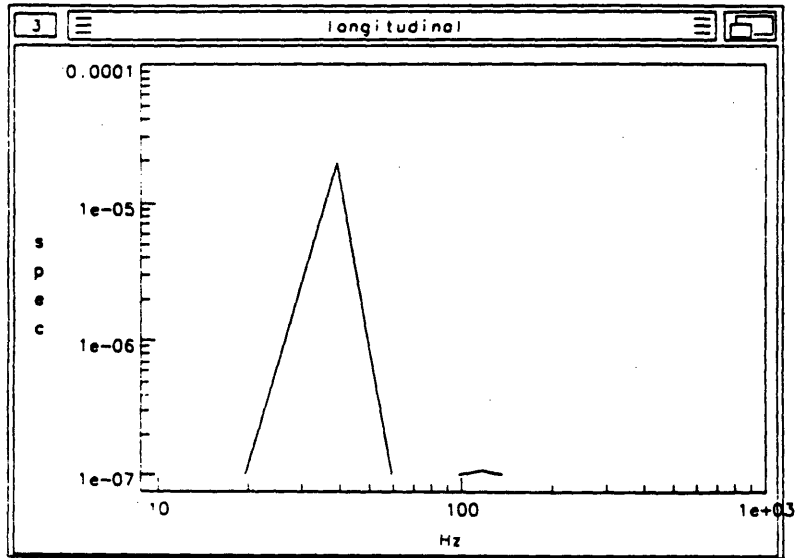
Longitudinal wave power spectrum  
for pure tone excitation @ 19.531 Hz



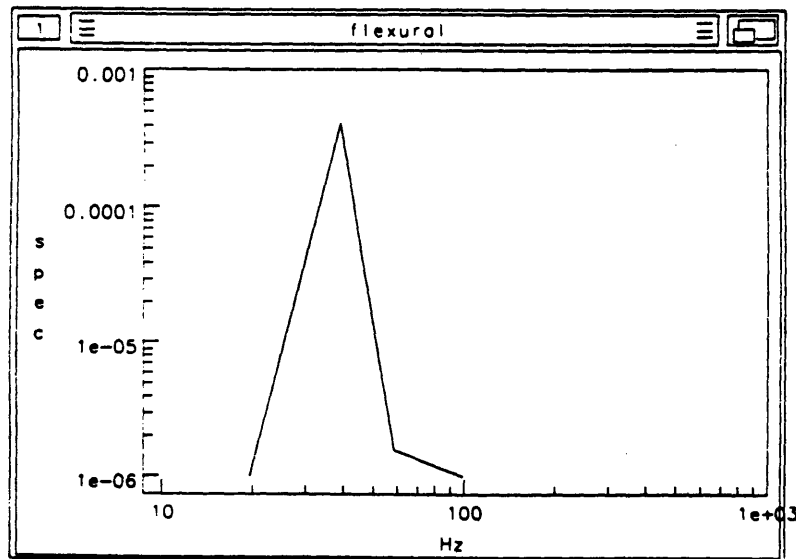
Flexural wave power spectrum for  
pure tone excitation @ 19.531 Hz



Time series/frequency response of pure tone longitudinal excitation @ 39.531 Hz

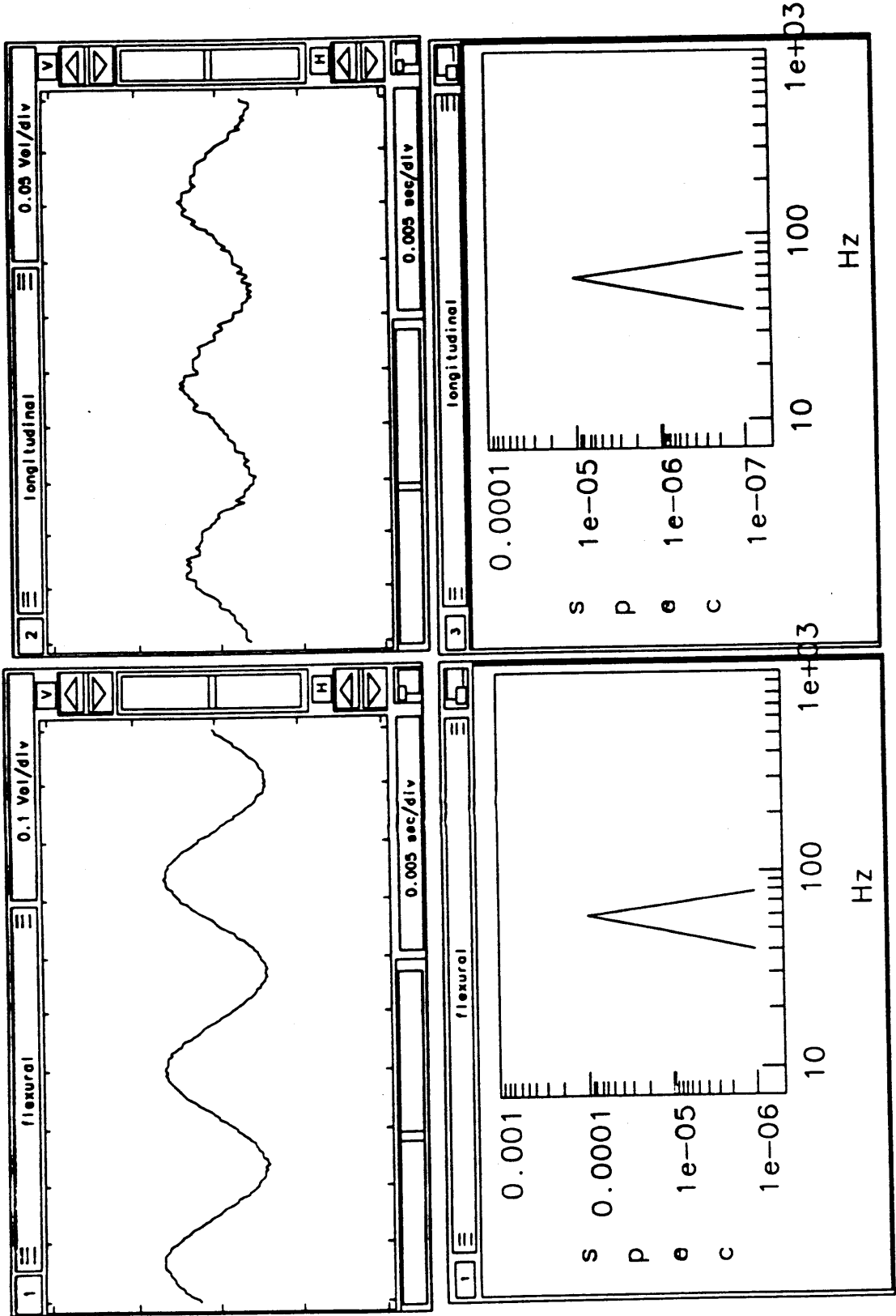


Longitudinal wave power spectrum  
for pure tone excitation @ 39.531 Hz

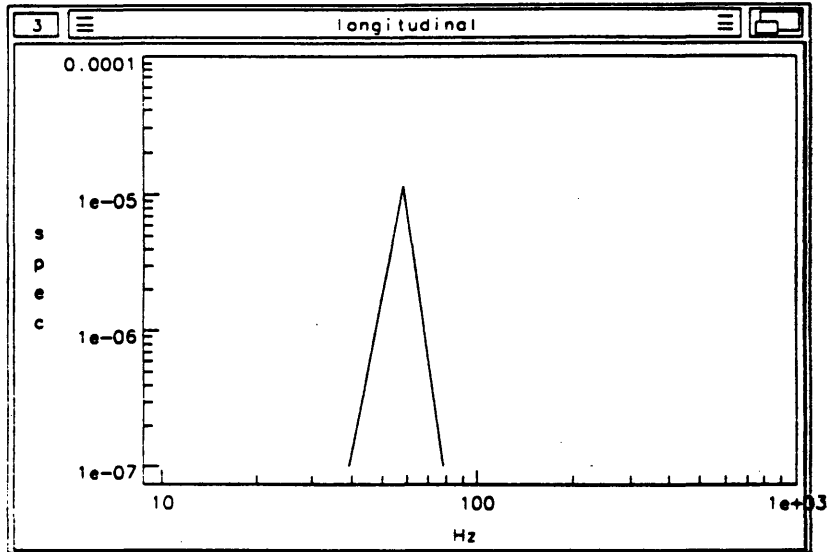


Flexural wave power spectrum for  
pure tone excitation @ 39.531 Hz

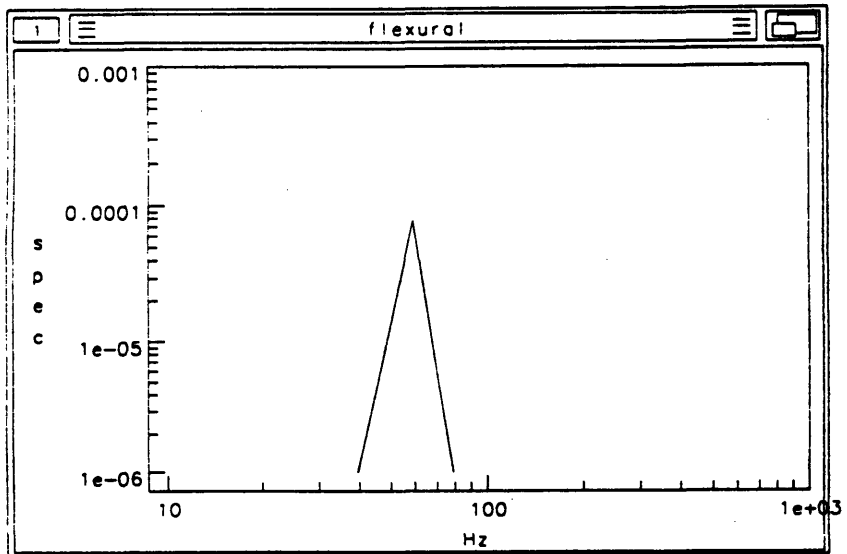




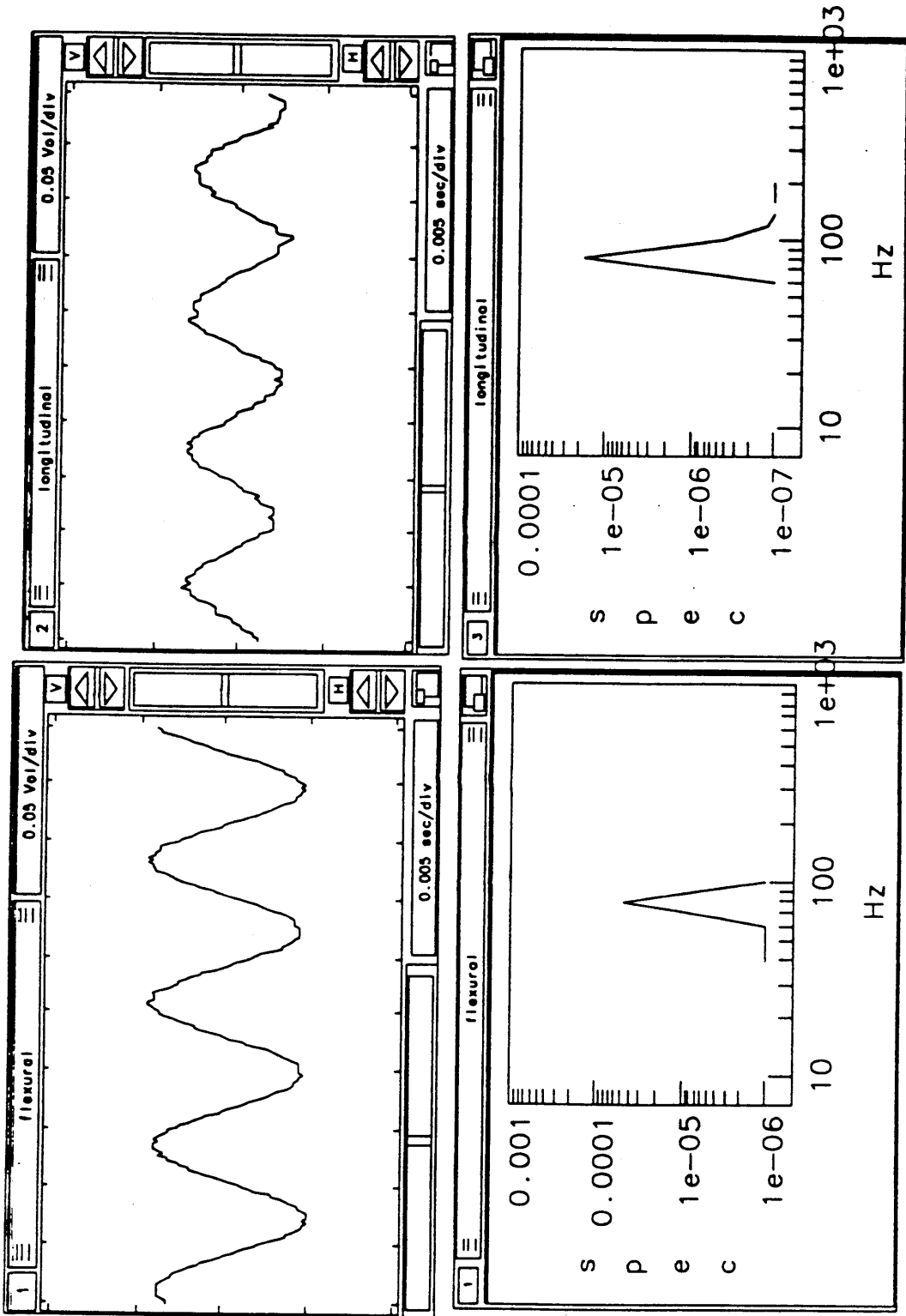
Time series/frequency response of pure tone longitudinal excitation @ 58.594 Hz



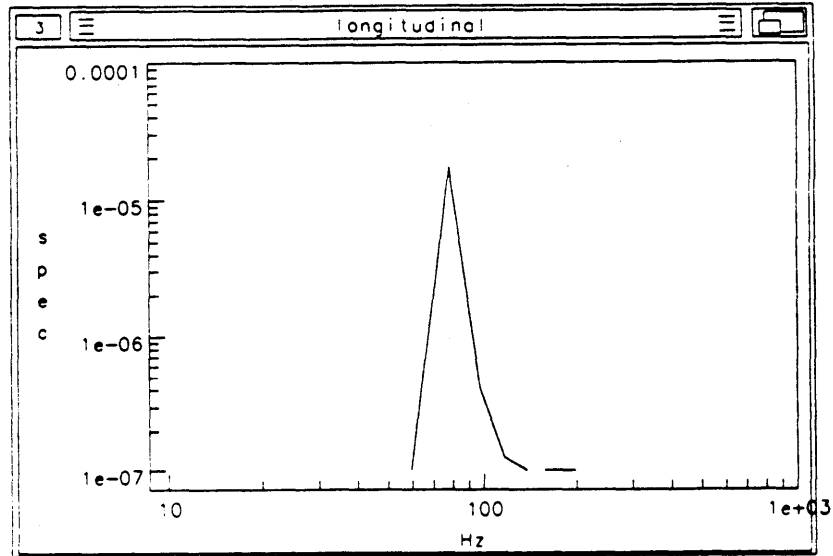
Longitudinal wave power spectrum  
for pure tone excitation @ 58.594 Hz



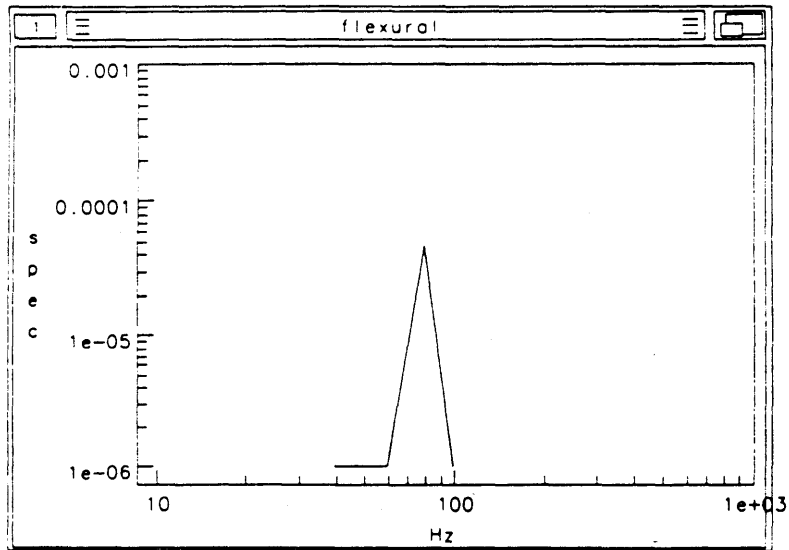
Flexural wave power spectrum for  
pure tone excitation @ 58.594 Hz



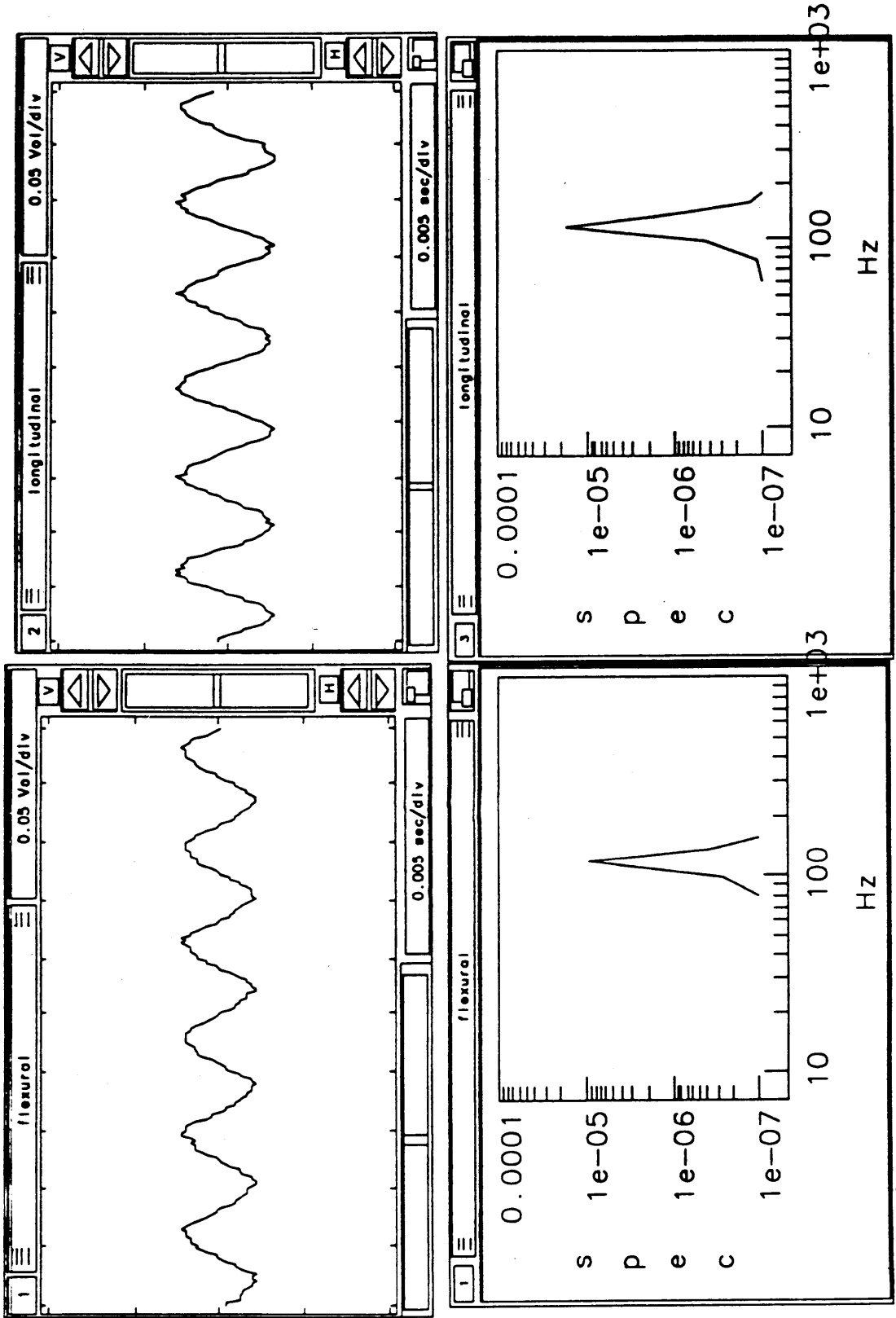
Time series/frequency response of pure tone longitudinal excitation @ 78.125 Hz



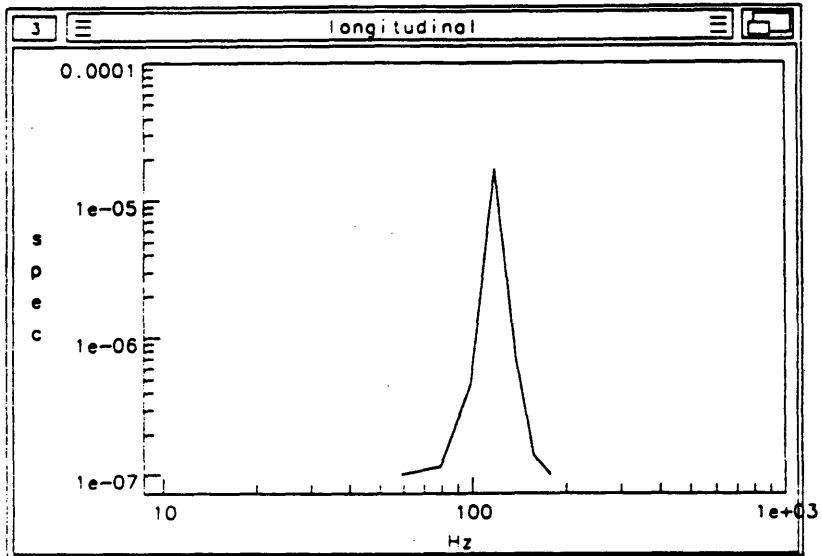
Longitudinal wave power spectrum  
for pure tone excitation @ 78.125 Hz



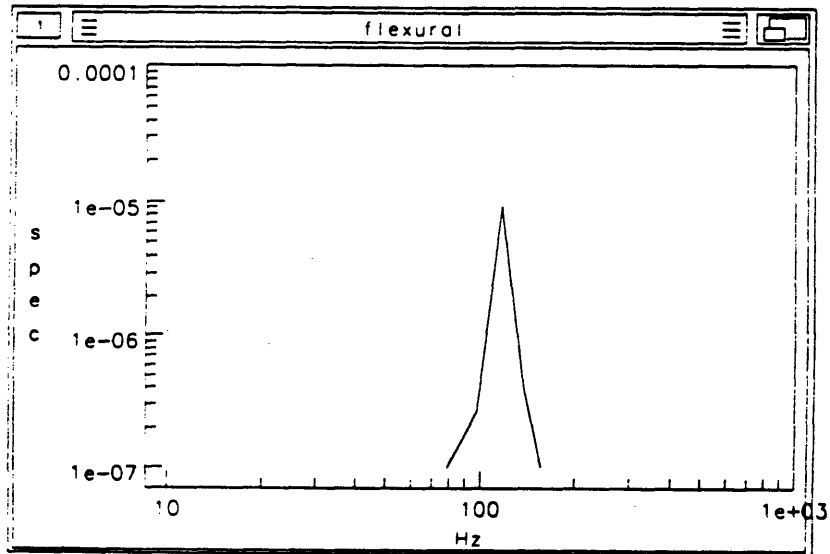
Flexural wave power spectrum for  
pure tone excitation @ 78.125 Hz



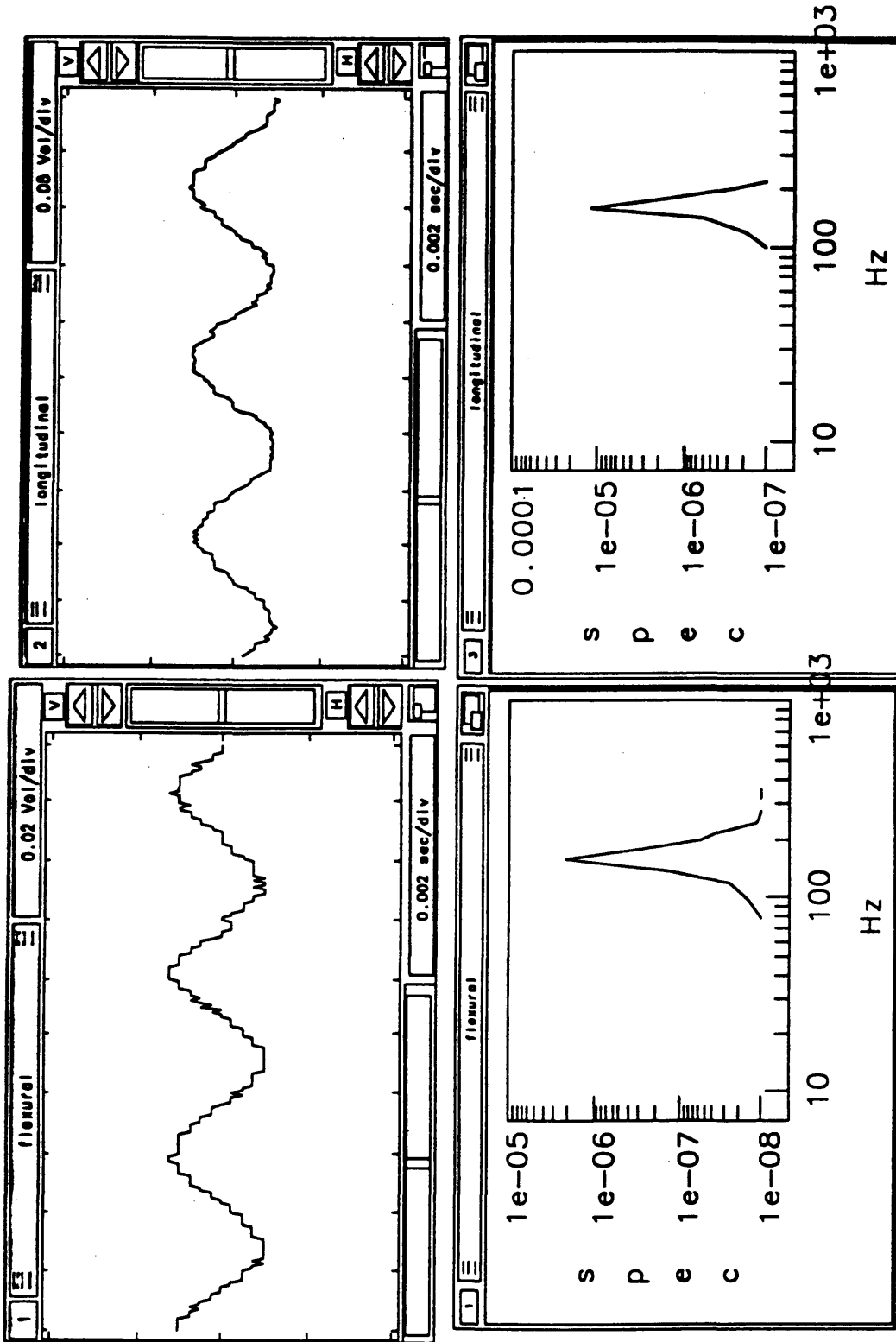
Time series/frequency response of pure tone longitudinal excitation @ 117.19 Hz



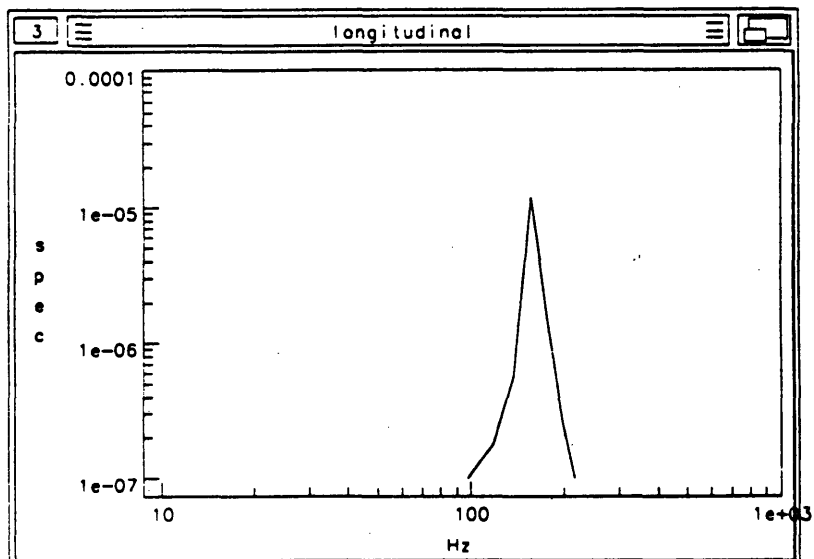
Longitudinal wave power spectrum  
for pure tone excitation @ 117.19 Hz



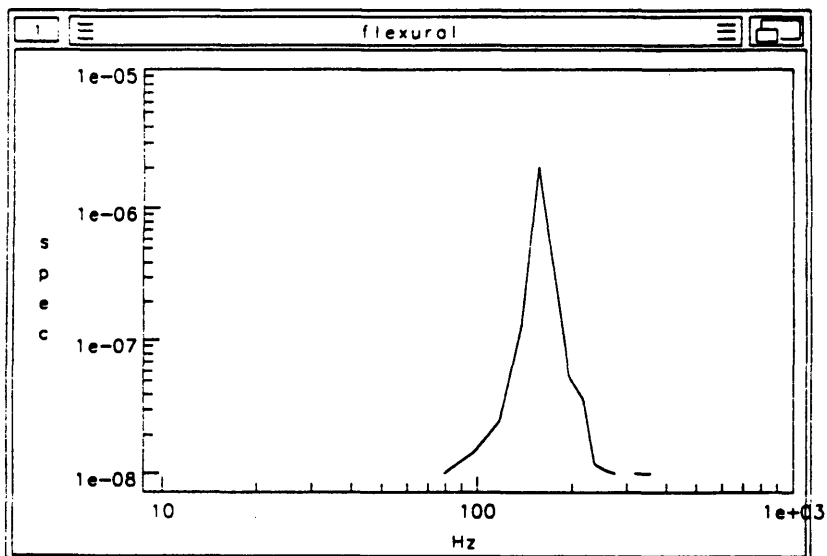
Flexural wave power spectrum for  
pure tone excitation @ 117.19 Hz



Time series/frequency response of pure tone longitudinal excitation @ 156.25 Hz

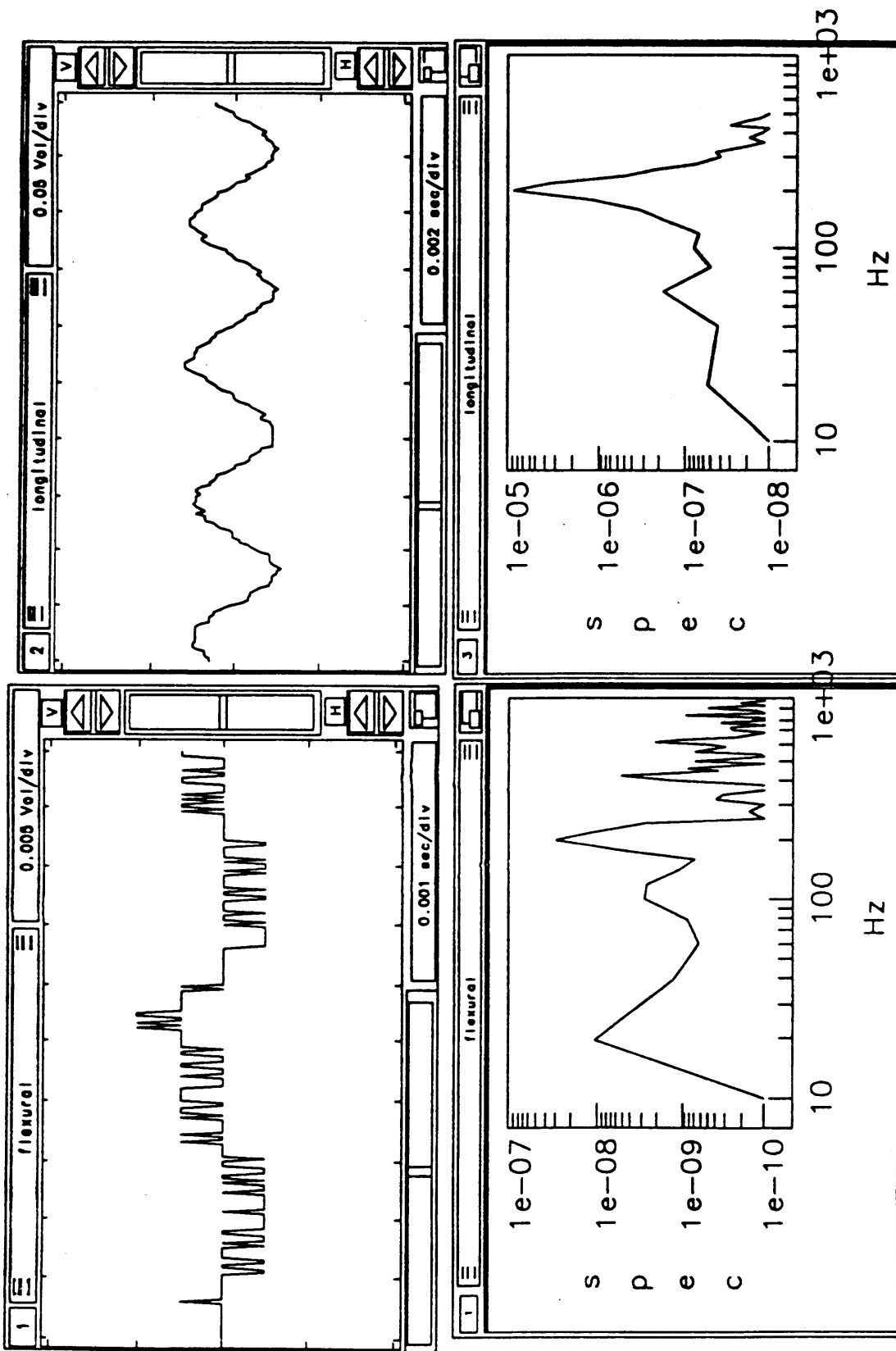


Longitudinal wave power spectrum  
for pure tone excitation @ 156.25 Hz

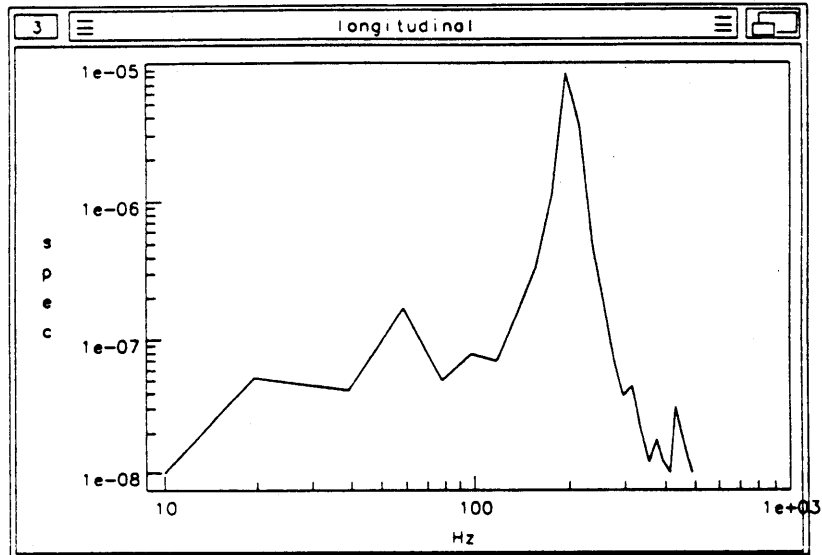


Flexural wave power spectrum for  
pure tone excitation @ 156.25 Hz

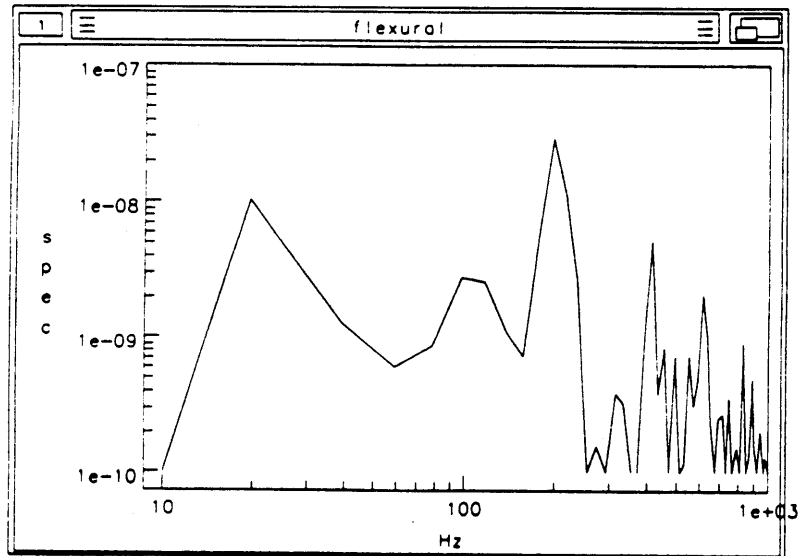




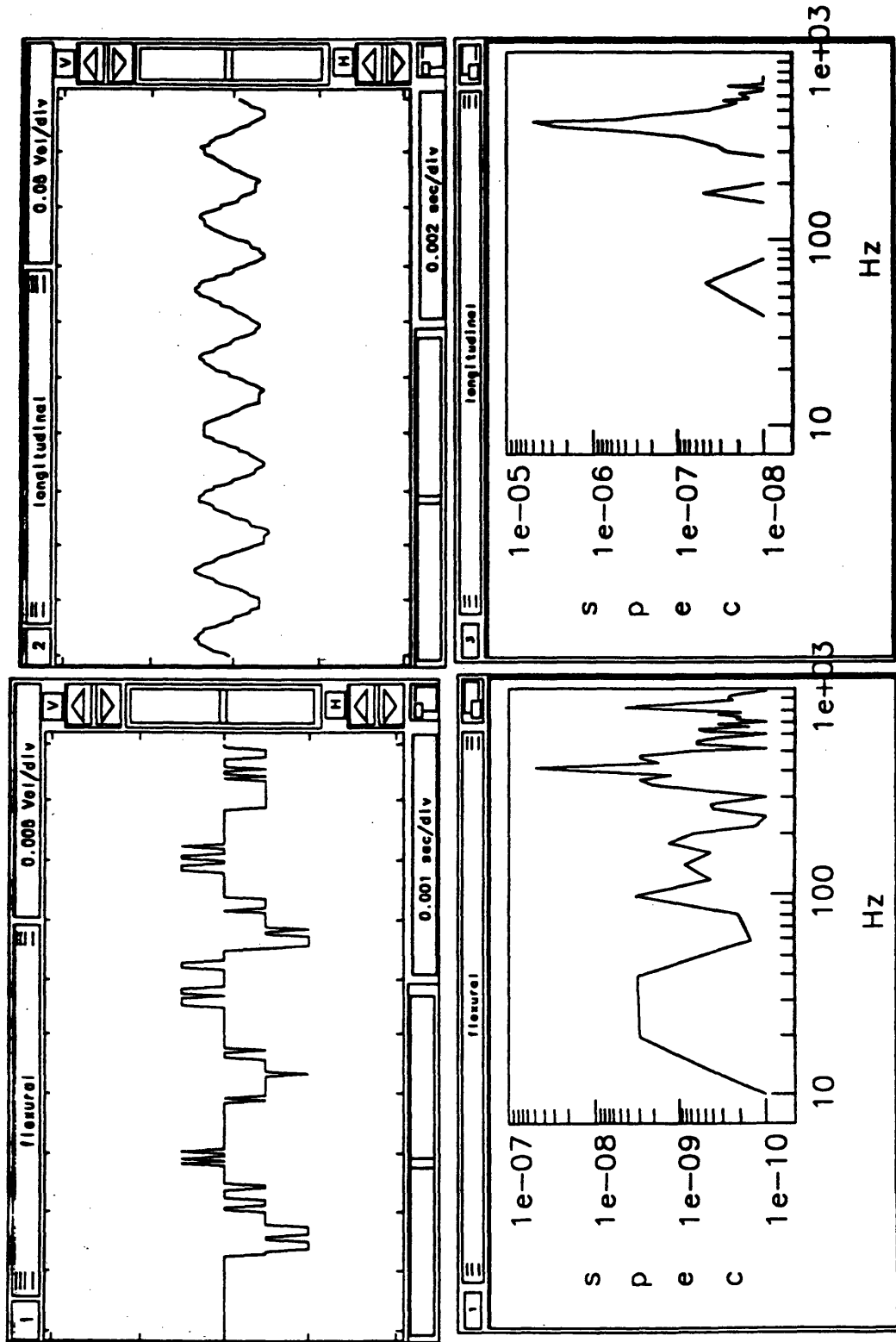
Time series/frequency response of pure tone longitudinal excitation @ 195.31 Hz



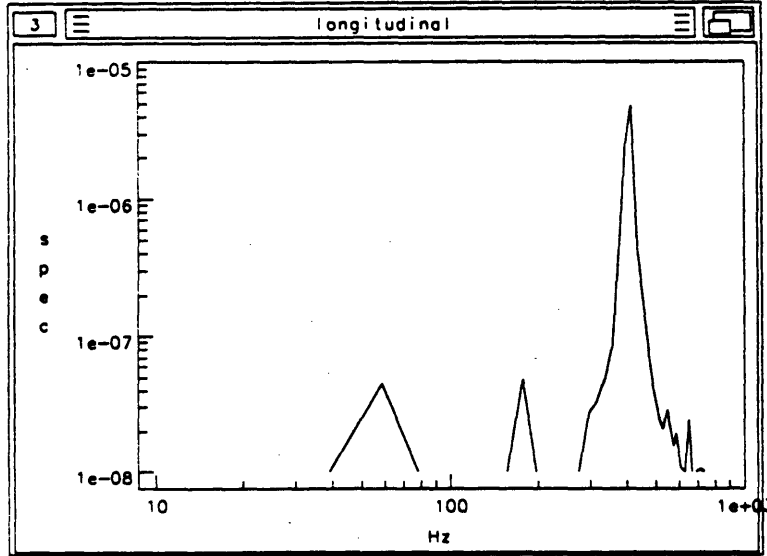
Longitudinal wave power spectrum  
for pure tone excitation @ 195.31 Hz



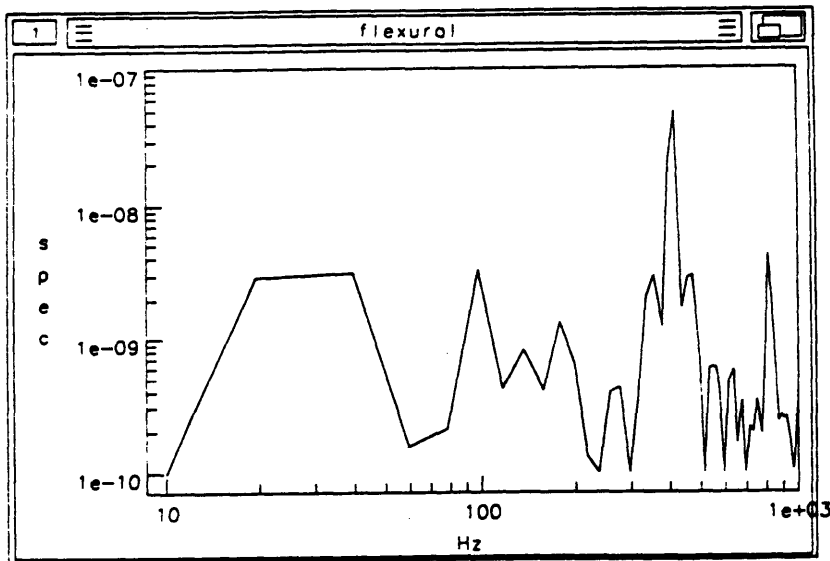
Flexural wave power spectrum for  
pure tone excitation @ 195.31 Hz



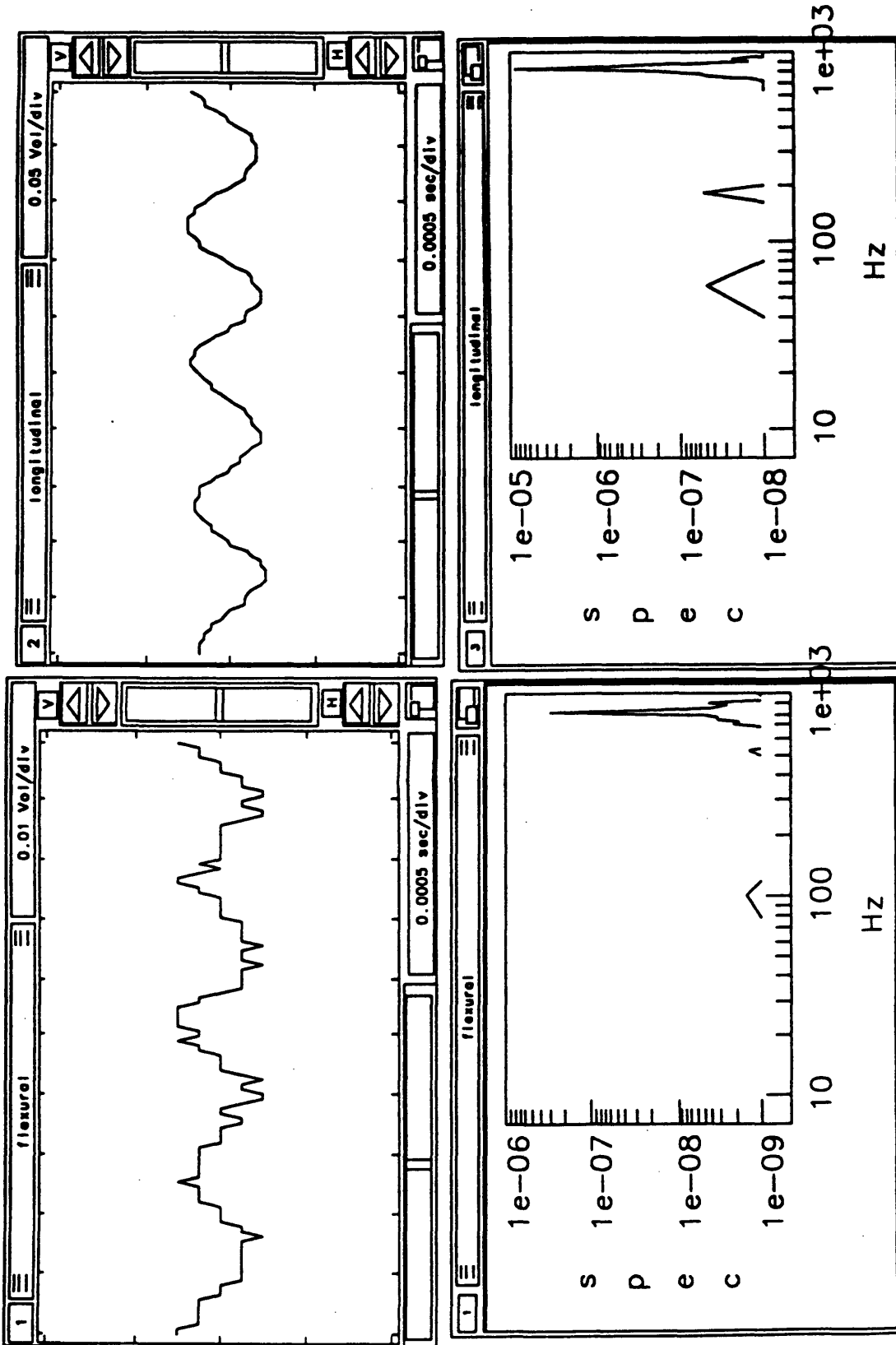
Time series/frequency response of pure tone longitudinal excitation @ 410.16 Hz



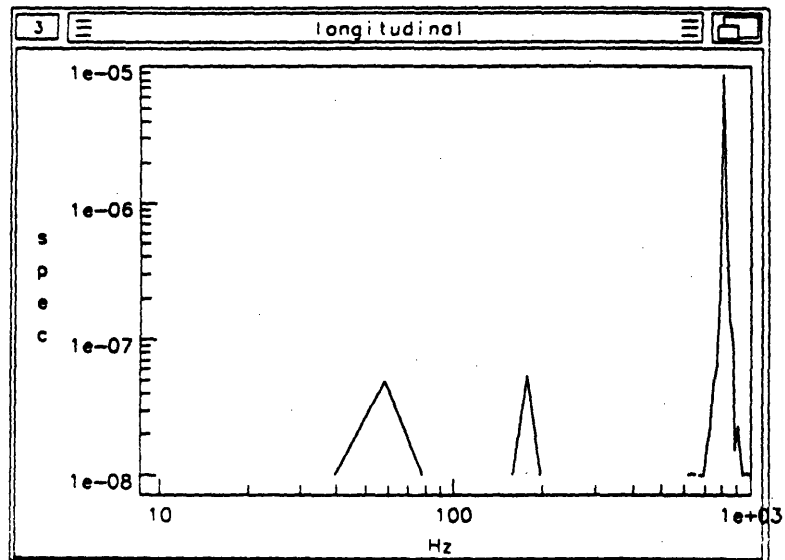
Longitudinal wave power spectrum  
for pure tone excitation @ 410.16 Hz



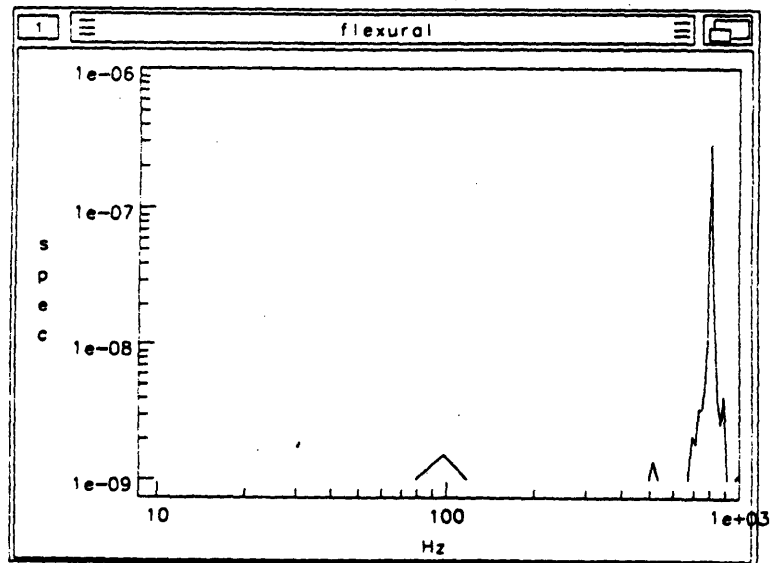
Flexural wave power spectrum for  
pure tone excitation @ 410.16 Hz



Time series/frequency response of pure tone longitudinal excitation @ 800.78 Hz



Longitudinal wave power spectrum  
for pure tone excitation @ 800.78 Hz



Flexural wave power spectrum for  
pure tone excitation @ 800.78 Hz